Université d'Ottawa · University of Ottawa

EVALUATION OF MODULATION TECHNIQUES FOR BROADBAND ACCESS OVER TWISTED PAIR

by

Mark Hawryluck, B.A.Sc.

A thesis submitted to the School of Graduate Studies and Research in partial fulfillment of the requirements for the degree of

Master of Applied Science
in Electrical Engineering

Ottawa-Carleton Institute for Electrical Engineering
School of Information Technology and Engineering
Faculty of Engineering
University of Ottawa
Ottawa, Ontario, Canada

0-612-26330-4

ABSTRACT

This thesis is a study of modulation techniques which could be used to provide Asymmetric Digital Subscriber Line (ADSL) and Very-high-speed Digital Subscriber Line (VDSL) services over Unshielded Twisted Pair (UTP). Three all-digital modulations are considered: Carrierless AM-PM (CAP), FFT Discrete Multitone (FFT-DMT) and Cosine Modulated Filter Bank Discrete Multitone (CMFB-DMT). The relative merits of the three modulations are examined at two data rates, 6 Mbps and 26 Mbps, which are representative of downstream ADSL and VDSL rates, respectively.

Block diagrams and mathematical descriptions are provided for all three modulations. A discussion of modeling the UTP channel and a number of impairments, namely AWGN, self-FEXT, NEXT, narrow-band interference and impulse noise, is also included.

Link margins computed for the three modulations on a variety of UTP loop lengths indicate that multicarrier modulation can offer a performance advantage over CAP modulation on AWGN-dominated loops with moderate to heavy attenuation. The link margins for multicarrier modulation are observed to be, at best, equivalent to the margins for CAP modulation when self-FEXT dominates.

Time-domain BER simulation strategies are outlined for all three modulations. A simple Monte-Carlo simulation is described for CAP; semi-analytical simulations based upon the Gauss quadrature rules are described for both CMFB-DMT and FFT-DMT.

The simulated BER performance of 16-CAP and the two multicarrier modulations in the presence of AWGN is presented. The performance in the presence of AWGN demonstrates the feasibility of using any of the modulations at both data rates. Simulation results are also used to demonstrate that the most effective equalization model for CMFB-DMT includes both a linear equalizer and a post-detection combiner. Both multicarrier modulations are observed to offer and advantage over CAP since they do not suffer from significant penalties due to equalization under the simulated conditions. The performance

of FFT-DMT is also observed to be marginally better than that of CMFB-DMT due to its highly effective equalization scheme.

More detailed study of the link margin performance of 16-CAP and the two multicarrier modulations in the presence of self-FEXT indicates that self-FEXT causes similar error floors for both CAP and multicarrier modulation. Multicarrier modulation offers no discernible advantage over CAP in the presence of dominant self-FEXT.

The simulated BER performance in the presence of AWGN of 16-CAP VDSL with emission masking is included. The spectral notches introduced by the emission masking filter cause a dramatic increase in the number of DFE taps required. The BER performance curves show significant penalties due to noise enhancement in the masking notches and due to the fact that the large equalizers were trained using the standard LMS algorithm.

The spectral isolation properties of the CMFB and FFT filters are examined briefly. This mostly qualitative analysis indicates that CMFB-DMT should be more robust than FFT-DMT in the presence of narrow-band interference.

The computational complexity in terms of real operations per bit is considered for 16-CAP, CMFB-DMT and FFT-DMT at ADSL and VDSL data rates. The complexity analysis indicates that the multicarrier modulations offer an advantage over CAP modulation in this regard. Furthermore, it is noted that the complexity of the FFT-DMT receiver is less than that of the CMFB-DMT receiver due to the high equalization complexity required for CMFB-DMT.

TABLE OF CONTENTS

ABSTRACT .... **I**

TABLE OF CONTENTS .... **III**

LIST OF FIGURES .... **VI**

ACKNOWLEDGMENTS .... **VIII**

GLOSSARY .... **IX**

LIST OF SYMBOLS .... **XII**

INTRODUCTION **1**

1.1 MOTIVATION 1
1.2 SCOPE AND ORGANIZATION 2
1.3 CONTRIBUTIONS 5

THE MODULATIONS: BASIC PRINCIPLES **6**

2.1 CAP 6
2.1.1 System Overview *6*
2.1.2 Decision Feedback Equalization *9*
2.2 CMFB-DMT 11
2.2.1 Some Generalities About Multicarrier Modulation *11*
2.2.2 CMFB-DMT System Overview *13*
2.2.3 CMFB Structure and Design *15*
2.2.4 Equalization and Post-Detection Combining *19*
2.2.5 Bit Allocation and Spectrum Shaping *22*
2.2.5.1 Optimization with AWGN Only 22
2.2.5.2 Optimization With AWGN and Self-FEXT 29
2.3 FFT-DMT 30
2.3.1 FFT-DMT System Overview *30*
2.3.2 Equalization for FFT-DMT *32*
2.3.3 Bit allocation and Spectrum Shaping *35*
2.3.3.1 Optimization with AWGN Only 36
2.3.3.2 Optimization With AWGN and Self-FEXT 38

CHANNEL AND IMPAIRMENT MODELING **40**

3.1 THE UTP CHANNEL 40
3.2 AWGN 43
3.3 FEXT 44
3.4 NARROW-BAND INTERFERENCE AND EMISSION MASKING 46
3.5 NEXT 48

3.6 IMPULSE NOISE 49

LINK MARGIN ANALYSIS 54

4.1 CAP LINK MARGINS 55
4.2 DMT LINK BUDGETS 56
4.3 LINK MARGIN RESULTS 57
4.3.1 ADSL Link Margins 57
4.3.1.1 Margins with AWGN Only 61
4.3.1.2 Margins with self-FEXT 62
4.3.2 VDSL Link Margins 63
4.3.2.1 Margins with AWGN Only 65
4.4 ESTIMATING REACH 68
4.5 CHOICE OF CAP CONSTELLATION 69

SIMULATING THE ERROR RATE PERFORMANCE 71

5.1 CAP 71
5.1.1 Time Domain Monte-Carlo Simulation 71
5.1.1.1 Optimum Timing Recovery 74
5.1.1.2 Determining Equalization Requirements. 75
5.2 MULTICARRIER MODULATIONS 76
5.2.1 Simulation of CMFB-DMT in the Presence of AWGN 77
5.2.1.1 Formulating the CMFB-DMT Simulation Problem 80
5.2.1.2 Moment Computation 82
5.2.2 Simulation of FFT-DMT in the Presence of AWGN 83
5.2.2.1 Formulating the FFT-DMT Simulation Problem 85

SIMULATED PERFORMANCE RESULTS AND ANALYSIS 88

6.1 PERFORMANCE IN THE PRESENCE OF AWGN 88
6.1.1 16-CAP 88
6.1.1.1 CAP-ADSL Transmission in the presence of AWGN 88
6.1.1.2 CAP-VDSL Transmission in the Presence of AWGN 92
6.1.2 Multi-carrier Modulations 95
6.1.2.1 How Many Sub-Channels ? 95
6.1.2.2 CMFB-DMT 98
6.1.2.3 FFT-DMT 110
6.2 PERFORMANCE IN THE PRESENCE OF SELF-FEXT 117
6.2.1 Performance of 16-CAP in the Presence of Self-FEXT 119
6.2.1.1 ADSL Data Rate 119
6.2.1.2 VDSL Data Rate 121
6.2.2 Performance of Multicarrier Modulations in the Presence of Self-FEXT 122
6.2.2.1 ADSL Data Rate 123
6.2.1.1 VDSL Data Rate 124
6.3 EMISSION MASKING AND NARROW-BAND INTERFERENCE 126
6.3.1 Performance of CAP with Emission Masking 126
6.4.1 Narrow-Band Interference and Multicarrier modulations. 130

COMPUTATIONAL COMPLEXITY 134

7.1 CAP 134
7.2 CMFB-DMT 135
7.3 FFT-DMT 137

7.4 Estimated Complexity for ADSL 138
7.5 Estimated Complexity for VDSL 140
CONCLUSIONS AND SUGGESTIONS FOR FUTURE WORK 142
8.1 Summary and Conclusions 142
8.2 Suggestions for Future Work 152
BIBLIOGRAPHY 155

LIST OF FIGURES

Number *Page*

Figure 1: Simplified Network Configuration 3
Figure 2: A CAP System 7
Figure 3: DFE Block Diagram 10
Figure 4: Channel Frequency Response (Hc) and Multicarrier Spectrum (Sm) 12
Figure 5: CMFB-DMT System 14
Figure 6: Discrete Impulse Response of Lowpass Prototype Filter for an Eight Sub-Channel PR-CMFB 16
Figure 7: Analysis Filter Impulse Responses for an Eight Sub-Channel PR-CMFB 17
Figure 8: Analysis Filter Frequency Responses for an Eight Sub-Channel PR-CMFB 18
Figure 9: 3x3 Post Detection Combiner Span in the Time-Frequency Plane 20
Figure 10: Sample Bit Allocation Results 27
Figure 11: Sample Optimized Spectrum 28
Figure 12: FFT-DMT Block Diagram 31
Figure 13: Equalizer Design Block Diagram 33
Figure 14: 16-QAM Constellation 36
Figure 15: Sample UTP Impulse Response 42
Figure 16: Sample UTP Frequency Response 43
Figure 17: Example Self-FEXT Spectrum 45
Figure 18: Impulse Noise in the Time and Frequency Domains 50
Figure 19: ADSL Link Margins vs. Loop Length - AWGN Only 61
Figure 20: ADSL Link Margins vs. Loop Length - AWGN + 49 FEXT 62
Figure 21: VDSL Link Margins vs. Loop Length - AWGN Only 65
Figure 22: VDSL Link Margins vs. Loop Length - AWGN + 10 FEXT 66
Figure 23: VDSL Link margins vs. Loop Length - AWGN + Emission Masking 67
Figure 24: CAP Simulation Block Diagram 72
Figure 25: CAP Monte-Carlo Simulation Flow Chart 73
Figure 26: CMFB-DMT Semi-Analytical Simulation Block Diagram (for k^{th} Sub-Channel) 78
Figure 27: Flow-chart for Performance Simulation of a Single Sub-Channel 79
Figure 28: FFT-DMT Semi-Analytical Simulation Block Diagram (for k^{th} Sub-Channel) 84
Figure 29: 16-CAP ADSL Performance in the Presence of AWGN 91
Figure 30: 16-CAP VDSL Performance in the Presence of AWGN 94
Figure 31: Performance of FFT-DMT in the Presence of AWGN with no CP or TEQ 97
Figure 32: CMFB-DMT ADSL Performance on 2000 m Loop Using FIR Equalizer Only 100
Figure 33: CMFB-DMT ADSL Performance on 2000 m Loop Using Idealized Post-Detection Combining 101

Figure 34: CMFB-DMT ADSL Performance on 2000 m Loop Using an Ideal 5-5 Post-Detection Combiner and FIR Equalizers.......... 103
Figure 35: CMFB-DMT ADSL Performance in the Presence of AWGN (With Optional FIR Equalization and Ideal 5-5 Post-Detection Combiner).......... 105
Figure 36: CMFB-DMT VDSL Performance in the Presence of AWGN(With Optional FIR Equalization and 5-5 Post-Detection Combiner).......... 108
Figure 37: CMFB-DMT VDSL Performance on 1000 m Loop Using a Reduced Maximum Sub-Channel Bit Load.......... 109
Figure 38: FFT-DMT ADSL Performance in the Presence of AWGN.......... 112
Figure 39: FFT-DMT VDSL Performance in the Presence of AWGN.......... 115
Figure 40: FFT-DMT VDSL Performance on 1050 m Loop Using a Reduced Maximum Sub-Channel Bit Load.......... 116
Figure 41: 16-CAP VDSL Symbol Error Rate Performance in the Presence of FEXT (500 m Loop, Infinite ZF-DFE).......... 118
Figure 42: 16-CAP ADSL Link Margin Performance vs. Transmit Power.......... 120
Figure 43: 16-CAP VDSL Link Margin Performance vs. Transmit Power.......... 121
Figure 44: Multicarrier ADSL Margin Performance vs. Transmit Power.......... 123
Figure 45: Multicarrier VDSL Margin Performance vs. Transmit Power.......... 125
Figure 46: CAP-VDSL Performance with Emission Masking.......... 127
Figure 47: CAP-VDSL Performance with Emission Masking Using Smaller DFE's Than in Figure 46.......... 129
Figure 48: Normalized Narrow-Band Interference Magnitude at Output of Analysis CMFB (Case A – Interferer at sub-channel center; Case B – Interferer between two sub-channels).......... 131
Figure 49: Normalized Narrow-Band Interference Magnitude at Output of Analysis FFT (Case A – Interferer at sub-channel center; Case B – Interferer between two sub-channels).......... 132

ACKNOWLEDGMENTS

To begin with, I would like to thank my thesis supervisors, Dr. Mohsen Kavehrad and Dr. Abbas Yongaçoglu, for providing a good working environment and excellent assistance when it was needed. Particularly in the recent months, Dr. Yongaçoglu has also provided a shining example of a good work ethic.

Thanks is also due to Mohammad Reza Pakravan for the many helpful discussions we have had on the subject matter in this work. Our talks have proven to be invaluable in improving my understanding and making this work clear.

During the course of this work, financial assistance was provided to me by the University of Ottawa and the Natural Sciences and Engineering Research Council. I am very grateful to have had the benefit of this funding.

For providing practical points of view, access to standards and related materials, and the opportunity to interact with a high caliber design group, I would like to thank Dr. Henry Wong, Dr. Sami Aly and Christian Bourget of Nortel.

Thanks also to Dr. Ranjan Gangopadhyay for initially helping to spark my interest in this material and for his correspondence.

For his useful input on the topic of impulse noise, and for being an able squash opponent, I would like to thank Robin Mélinand.

Thanks to my colleagues and friends for their occasional advice and for making the last two years memorable.

Most of all, I would like to thank my family and Justine Hoang whose understanding and support made all the difference in the world.

— Mark Hawryluck, June 1997

GLOSSARY

A/D	Analog to Digital
ADSL	Asymmetric Digital Subscriber Line
AGC	Automatic Gain Control
AM	Amplitude Modulation
ATM	Asynchronous Transfer Mode
AWGN	Additive White Gaussian Noise
BER	Bit Error Rate (bit error probability)
CAP	Carrierless AM/PM
CATV	Community Antenna Television
CP	Cyclic Prefix
CMFB	Cosine Modulated Filter Bank
CMFB-DMT	Cosine Modulated Filter Bank Discrete Multitone
D/A	Digital to Analog
DFE	Decision Feedback Equalizer
DWMT	Discrete Wavelet Multitone
FDEQ	Frequency Domain Equalizer
FDM	Frequency Division Multplexing
FEXT	Far-End Cross Talk
FFT	Fast Fourier Transform
FFT-DMT	Fast Fourier Transform Discrete Multitone
FIR	Finite Impulse Response

FTTN	Fiber To The Neighborhood
GQR	Gauss Quadrature Rules
HFC	Hybrid Fiber-Coax
ICI	Inter-Channel Interference
ISDN	Integrated Services Digital Network
ISI	Inter-Symbol Interference
LMS	Least Mean Square (stochastic gradient adaptation algorithm)
MSE	Mean-Square Error
MOM	Method of Moments
NEXT	Near-End Cross Talk
OFDM	Orthogonal Frequency DivisionMultiplexing
PAM	Pulse Amplitude Modulation
PDF	Probability Density Function
PM	Phase Modulation
PMF	Probability Mass Function
PR	Perfect Reconstruction
PSD	Power Spectral Density
QAM	Quadrature Amplitude Modulation
RLS	Recursive Least-Squares
RX	Receiver
SNR	Signal to Noise Ratio
TEQ	Time-Domain Equalizer
TX	Transmitter

UTP	Unshielded Twisted Pair
VDSL	Very high-speed Digital Subscriber Line
xDSL	Either ADSL or VDSL
ZF	Zero-Forcing

LIST OF SYMBOLS

$\{A_m\}$	A set of PAM symbols
$a_{I\,k}$	Parameters of generalized exponential impulse noise inter-arrival time distribution
$a_{j,k}$	PAM symbol on the j^{th} sub-channel of a multicarrier system
a_k	PAM symbol representing the real part of a CAP or QAM symbol
(a_k+jb_k)	Two dimensional CAP or QAM symbols
B	Set of frequencies within the 3 dB bandwidth of a CAP signal
b_A	Aggregate number of bits carried by a single multicarrier symbol
$bits_k$	Number of bits carried by k^{th} multicarrier sub-channel
b_k	PAM symbol representing the imaginary part of a CAP or QAM symbol
$B_{TIR\,i}$	i^{th} DFT coefficient of the truncated impulse response (TIR) in FFT-DMT
$b_{TIR\,n}$	Truncated impulse response (TIR) in FFT-DMT
$C_{k,n}$	CMFB modulating sequences
$c_{m,k}$	QAM symbol transmitted on FFT-DMT sub-channel m at instant k
C_p	Capacitance primary constant of a transmission line
d_c	Coupling distance for crosstalk models
$d_{RX\,k}$	Received constellation distance on k^{th} multicarrier sub-channel
$d_{TX\,k}$	Transmitted constellation distance on k^{th} multicarrier sub-channel
E_b/N_o	Signal to noise ratio per bit
f	Frequency
f_{baud}	Baud rate

f_c Carrier frequency

$f_{Dur.}(t)$ Density function of impulse noise event duration

$f_{Inter.}(x)$ Density function of impulse noise inter-arrival time

f_k Center frequency of k^{th} multicarrier sub-channel

f_s Sampling frequency

$f_{Voltage}(u)$ Density function of impulse noise voltage

$f_\zeta(\zeta_p)$ PMF of the aggregate ISI and ICI in a multicarrier system

g Genus number for CMFB

$G(f)$ Self-FEXT gain function

$g_{I\,n}$ In-phase modulated pulse in a CAP system

$g_{j,n}$ Impulse response of j^{th} synthesis filter in a multicarrier system

G_p Conductance primary constant of a transmission line

$g_{Q\,n}$ Quadrature-phase modulated pulse in a CAP system

$h_{c\,n}$ Channel impulse response

$H_c(f)$ Channel frequency response

$h_{eq\,n}$ Impulse response of FIR equalizer in CMFB-DMT system

$h_{j,n}$ Impulse response of j^{th} analysis filter in a multicarrier system

$h_{lp\,n}$ Impulse response of CMFB low-pass prototype

$h_{UTP\,n}$ UTP impulse response

$H_{UTP}(f)$ UTP frequency response

ICI Inter-channel interference

ISI Inter-symbol interference

K Number of DFE feedback taps

k_F	Coupling coefficient used in self-FEXT model
k_N	Coupling coefficient used in NEXT model
L	Number of DFE feed-forward taps
L_{CAP}	Number of elements in a CAP constellation
L_{FIR}	Length of FIR equalizer in CMFB-DMT
L_k	Number of constellation elements on the k^{th} multicarrier sub-channel
L_p	Inductance primary constant of a transmission line
L_{pulse}	Length (in samples) of a CAP pulse
L_{TEQ}	Length of TEQ in FFT-DMT
M	Number of sub-channels in a filter bank
m	Performance margin
N	Number of samples per symbol in CAP modulation
N'	Length of FFT-DMT symbols
N_c	Length in samples of CMFB filters
N_d	Number of disturbers in crosstalk models
N_{DFE}	Total number of DFE taps
N_{FFT}	Length of FFT
$P_{dist}(f)$	Disturber PSD
$P_{e\,k}$	Probability of symbol error on k^{th} multicarrier sub-channel
$P_{e\,CAP}$	Probability of symbol error for CAP
$P_{FEXT}(f)$	Power spectral density of FEXT
P_k	Average transmitted power on k^{th} multicarrier sub-channel
$P_{m=0}$	Transmit power for zero performance margin

p_n	Baseband pulse (CAP)
$P_{NEXT}(f)$	Power spectral density of NEXT
P_o	Constant used in multicarrier spectrum optimization
P_{TX}	Aggregate transmitted power
q_d	"Weight" parameter of the bimodal, log-normal impulse noise duration distribution
R	Bit rate
$r_{ij,n}$	Cross-correlation between $g_{i,n}$ and $g_{j,n}$
$r_{m,n}$	Symbol spaced ISI on sub-channel k due to sub-channel m
R_p	Resistance primary constant of a transmission line
$S_{cap}(f)$	CAP signal power spectral density
s_{d1}, s_{d2}	"Spread" parameters of the bimodal, log-normal impulse noise duration distribution
$s_{k,j}$	Decision variable on sub-channel k at symbol instant j at the output of the post-detection combiner in a CMFB system
$S_m(f)$	Power spectral density of multicarrier signal
SNR	Signal to noise ratio
$SNR_{dec.}$	Signal to noise ratio at a decision device
SNR_g	Signal to Gaussian noise ratio
SNR_{geom}	Geometric signal to noise ratio
SNR_{min}	Minimum acceptable signal to noise ratio
T	Set of symbol instants considered by a post-detection combiner
t_{d1}, t_{d2}	"Median" parameters of the bimodal, log-normal impulse noise duration distribution
T_{sym}	Symbol Period

$v_{I\,n}$	Complex, symbol-spaced, end-to-end response due to a pulse launched on CAP in-phase channel
v_n	Symbol-spaced, end-to-end ISI response on sub-channel k of a multicarrier system
$v_{Q\,n}$	Complex, symbol-spaced, end-to-end response due to a pulse launched on CAP quadrature phase channel
W_i	i^{th} DFT coefficient of the FFT-DMT TEQ impulse response
w_n	FFT-DMT TEQ impulse response
x_n	A transmitted sequence
z	A complex number
Z^{-1}	Discrete-time unit delay
α_p	Attenuation constant of a transmission line
α_{RC}	Roll-off factor of a raised cosine pulse
β_p	Phase constant of a transmission line
χ	Set of sub-channels used in a multicarrier bit allocation
Δ	Delay parameter in FFT-DMT equalizer design
ϕ_t	Sampling phase
$\Phi_{n,i}$	Noise power observed in the band of the i^{th} FFT-DMT sub-channel
ϕ_{opt}	Optimum sampling phase
γ	Target value of $d_{RX\,k}/2\sigma_k$ for multicarrier bit allocation and spectrum optimization
γ_p	Propagation constant of a transmission line
η	Sample of additive noise
λ	Lagrange multiplier

λ_E	Instantaneous mean of the impulse noise inter-arrival time
μ_v	Parameter of double-sided exponential impulse noise voltage distribution
$\Phi_n(f)$	Noise power spectral density
$\theta_{v,l}$	Output of CMFB analysis filter v at symbol instant l
ϑ_p	Cumulant of order p of a random variable
$\sigma_{FEXT\ k}$	Standard deviation of the FEXT noise observed on the k^{th} multicarrier sub-channel detector output
σ_k	Noise variance due to AWGN at the k^{th} multicarrier sub-channel detector output
υ	FFT-DMT cyclic prefix length
$\varsigma_{v,l}$	Post-detection combiner coefficient acting on the output of analysis filter v at time l
ς_k	k^{th} DFE coefficient
Ω	Set of sub-channels considered by a post-detection combiner
ξ_n	n^{th} random variable which contributes to ISI on the k^{th} multicarrier sub-channel
ζ	Aggregate ISI and ICI (random variable)
ζ_k	k^{th} point at which the PMF of ζ is defined

Chapter 1

Introduction

1.1 Motivation

In the last five years, bandwidth hungry applications like surfing the World-Wide Web and telecommuting have seen an exponential increase in popularity. It has become clear that voice-band modems and even ISDN (which has led a surprisingly quiet existence to date) leave a lot to be desired in terms of data rate. The simple truth is that people like pictures – these older technologies aren't fast enough to support graphics intensive applications. Surprisingly, fiber to the home is still considered to be a "future technology" – currently too costly for mass consumption [1]. This situation has created an explosion of activity in the field of high speed modem design as various players in the telecommunications industry scramble to develop economical technology to enable broadband digital services over existing metallic plant.

The most visible competitors in the race to develop broadband access technology are telephone companies which want to squeeze all that they can from their vast existing Unshielded Twisted Pair (UTP) plant ([1], [43], [68]). Cable television providers have added an interesting twist to the broadband access fray as they push the development of cable modems and HFC networks as a means of gaining entry into the digital services market ([33], [34], [50]). Coaxial cable has a much better frequency response than twisted pair and this makes it a better medium for transmitting high data rate signals. Moving into the digital services market does, however, represent a serious paradigm shift for the CATV providers. There are other hurdles for the HFC/ cable modem combination to clear as well. ADSL Forum [1] estimates that world-wide there are 60 telephone lines capable of supporting ADSL for every available HFC line. It is not clear that CATV proponents will be able to accomplish the necessary sweeping changes in time to do serious damage to the market share of the telephone companies.

1.2 Scope and Organization

This thesis focuses on the performance analysis of modulation techniques which could be used to provide Asymmetric Digital Subscriber Line (ADSL) and Very-high-speed Digital Subscriber Line (VDSL) type services over UTP. Three standard metrics will be used to compare the modulations. These are the following: 1) link margin; 2) BER performance and 3) computational complexity. For the sake of simplicity, half-duplex transmission over straight lengths of UTP is considered. In order to further narrow down the scope of the comparison, two representative data rates are used. For ADSL, the representative data rate is chosen to be 6 Mbps and for VDSL the representative data rate is 26 Mbps. In both cases, the representative data rates are close to typical "downstream" (to the subscriber) rates mentioned in [1], [4] and [37]. The simplifications mentioned above can be considered in terms of a simplified network configuration where a generalized "Central Unit" (which may be thought of as a Fiber-To-The-Neighborhood node) transmits data simultaneously using a bank of identical modulators to a number of identical subscriber "Remote Units" or demodulators. This configuration is represented in Figure 1.

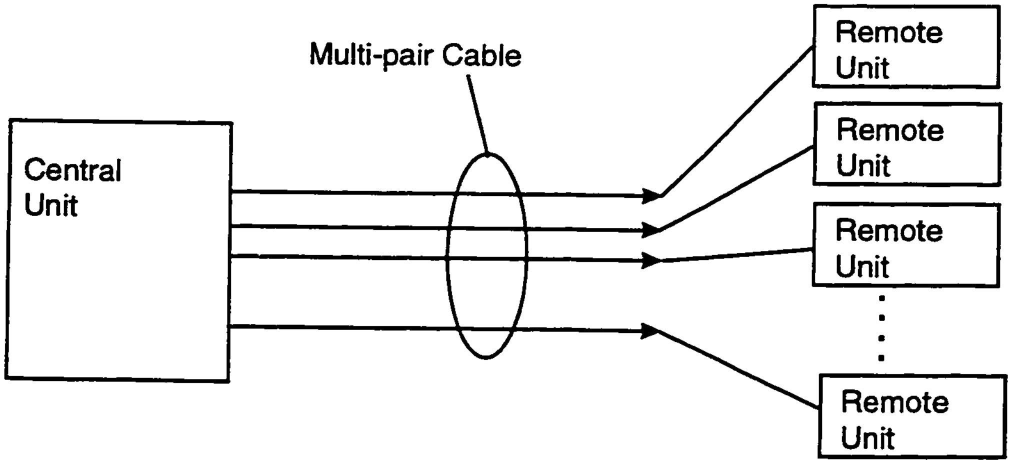

Figure 1: Simplified Network Configuration

The transmission of data on the upstream path from the remote units to the central unit is generally performed at a significantly lower effective data rate than is used for the downstream signal. The upstream signal can use proportionately less bandwidth, making it less susceptible to impairment by the UTP attenuation response. For these two reasons, the performance on the upstream path is likely to always be at least as good, if not better, than the performance on the downstream path.

The study of full duplex xDSL transmission is complicated by the fact that, depending upon how the upstream and downstream signals share the UTP medium, different issues come into play.

For multicarrier ADSL, the upstream signal usually carries less than 1 Mbps and is located at low frequency (~30 kHz - 110 kHz). Two types of multiplexing are allowed by the ADSL standard [4]: 1) the upstream and downstream signals can be frequency division multiplexed with the upstream signal occupying the band between 110 kHz and 1.1 MHz; or 2) the downstream signal can use the whole band (~30 kHz to 1.1 MHz) with echo cancellation employed to separate the upstream and downstream signals. For the first scenario, the capacity of the downstream signal path is limited to an extent due to the fact that the upstream signal occupies the least attenuating part of the UTP frequency response. In addition to Far-End CROSS-Talk (FEXT), some Near-End CROSS-Talk

(NEXT) and leakage between the upstream and downstream signals is possible. This is particularly true for the FFT multicarrier system specified in the ADSL standard since the sub-channels have relatively slow spectral roll-off. Some combination of band-pass filtering and guard-bands can be used to mitigate the effects of these impairments. In the case of the echo-cancellation scheme, both the upstream and downstream signals are significantly impaired by FEXT and also by NEXT since they share the same band. The quality of the echo-cancellation also plays a big role in determining the performance since it dictates the amount of direct leakage between the signals [9].

At the time of writing, the VDSL standard is still taking shape. As of May 1997, time-division duplexing is under consideration as a means of multiplexing the upstream and downstream VDSL signals [10]. This scheme has three major advantages: it eliminates direct leakage between the upstream and downstream signals; it allows both the upstream and downstream signals to use the entire available bandwidth; and it simplifies changing the ratio of the upstream and downstream data rates. Both FEXT and NEXT are still limiting impairments in the time division duplexing scenario because adjacent subscriber loops are likely to be unsynchronized.

Three bandwidth efficient, all-digital modulations are considered in this thesis. The first is Carrierless AM-PM (CAP) a single carrier scheme which is basically an in-band generation form of Quadrature Amplitude Modulation (QAM). Two multicarrier modulations are also considered. These are: Cosine Modulated Filter Bank based Discrete Multitone (CMFB-DMT), which is often referred to in the literature as Discrete Wavelet Multitone (DWMT), and Fast Fourier Transform based Discrete Multitone (FFT-DMT). These two multicarrier schemes use modulated filter banks to achieve frequency division multiplexed (FDM) transmission of many narrow bandwidth signals.

The remainder of this thesis is organized as follows: in Chapter 2, the modulation techniques will be described; Chapter 3 is a discussion of the channel and impairment models; Chapter 4 includes mathematical developments and results related to the computation of performance margins for the modulations on Category 3 UTP; Chapter 5 presents mathematical developments and discussion of BER performance simulations; Chapter 6 includes a discussion of the various BER performance results; in Chapter 7 the computational complexity of the three modulations is analyzed and finally, in Chapter 8, conclusions are presented.

1.3 Contributions

This work comprises five contributions to the general area of Broadband Access Technology. These contributions are: 1) a tutorial treatment of CAP, CMFB-DMT and FFT-DMT modulations as well as of the major UTP plant impairments; 2) the application of a semi-analytical simulation technique in determining the performance of the multicarrier modulations; 3) an efficient equalization scheme, which includes both an FIR equalizer and a post-detection combiner, is identified for CMFB-DMT; 4) an investigation of the spectral isolation behavior of CMFB and FFT filters; and 5) a relatively detailed analysis of the computational complexity of 16-CAP, CMFB-DMT and FFT-DMT.

Chapter 2

The Modulations: Basic Principles

In this section, the block diagrams of the various transmission systems are presented and the discrete-time transmitted signals are described mathematically. Certain critical components of the block diagrams are discussed in detail.

2.1 CAP

2.1.1 System Overview

Carrierless AM/PM or CAP is essentially digital QAM modulation using in-band signal generation [19]. CAP systems may use exactly the same two-dimensional signal constellations as QAM systems. In a CAP system, the passband signal is generated directly from the symbolic data using passband shaping pulses as opposed to modulating baseband pulse trains using quadrature carriers. The block diagram of a CAP system is shown in Figure 2. As can be seen from the diagram, the sequence of data symbols is first broken into in-phase and quadrature components. The two resultant sequences are then up-sampled to the sampling rate and the in-phase and quadrature phase passband shaping filters are applied. The sequence of samples to transmit is formed by simply adding together the outputs of the shaping filters. The transmitted sequence then passes through the composite channel which is made up of the digital to analog converter, the linear channel and the analog to digital converter. Note that the sampling phase of the receive A/D converter is set by some timing recovery mechanism. Next, matched filters are applied to the received signal samples and the in-phase and quadrature-phase results are downsampled to the symbol rate. The received complex symbol sequence which is corrupted by ISI and noise, is then applied to the input of an equalizer. A slicer is not shown in Figure 2 because in this work only decision feedback equalization is considered and decision feedback equalizers incorporate a slicer.

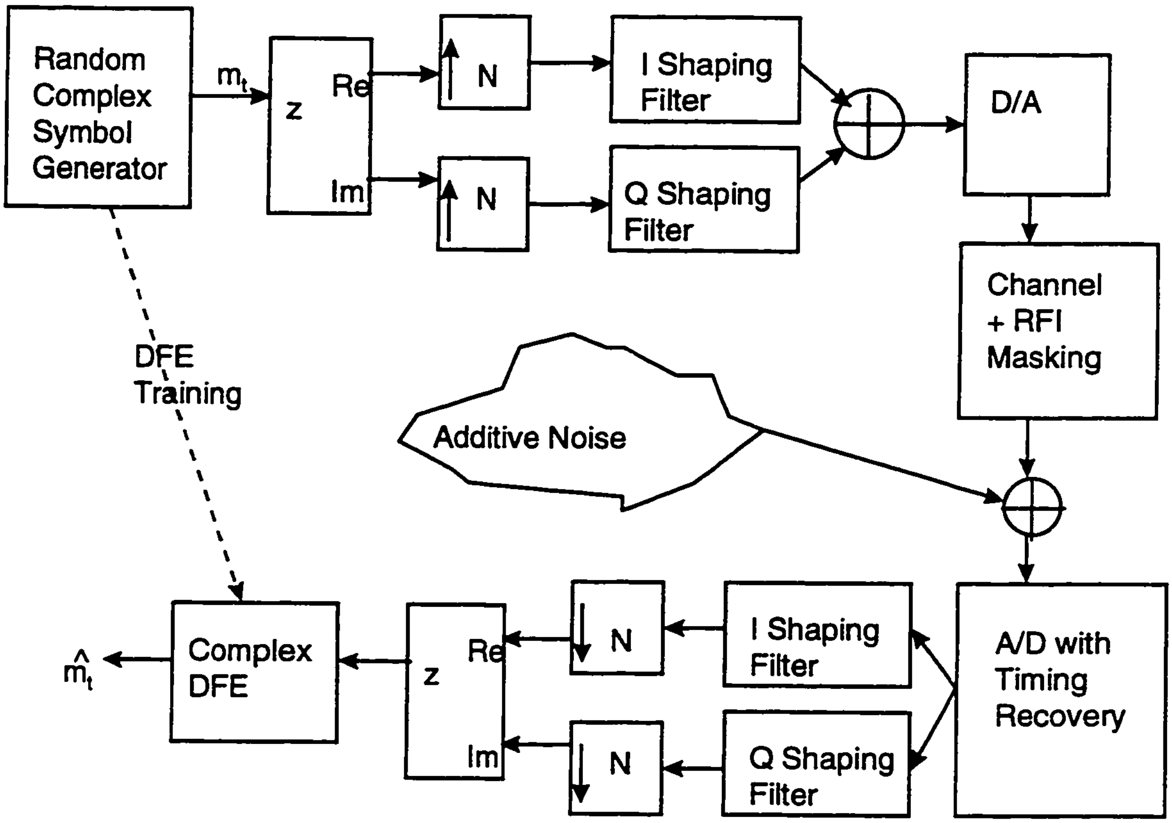

Figure 2: A CAP System

CAP modulation is best understood in terms of its relationship to QAM [11]. The sequence of transmitted samples in a digital QAM system can be expressed using the following familiar equation:

$$x_n = \sum_k \left\{ a_k p_{n-Nk} \cos\left(2\pi n f_c / f_s\right) + b_k p_{n-Nk} \sin\left(2\pi n f_c / f_s\right) \right\} \quad \ldots(1)$$

where: a_k and b_k represent the real an imaginary parts of a complex symbol respectively; $N = f_S/f_{baud}$ is the number of samples per symbol; f_C is the carrier frequency; f_S is the sampling frequency and p_n is some baseband pulse (usually chosen to ensure a Nyquist end-to-end response). After the developments in [11], we can re-write (1) in an in-band generation form. Basically, this entails combining the baseband pulse with the sinusoidal modulating functions as follows:

$$x_n = \sum_k \left\{ a_k^{'} g_{I\ (n-Nk)} + b_k^{'} g_{Q\ (n-Nk)} \right\} \qquad \ldots(2)$$

where $g_{I\,n}$ and $g_{Q\,n}$ are passband pulses defined as

$$g_{I\,n} = p_n \cos(2\pi n f_c / f_s) \qquad \ldots(3)$$

and

$$g_{Q\,n} = p_n \sin(2\pi n f_c / f_s) \qquad \ldots(4)$$

and a_k' and b_k' represent the real and imaginary parts of a rotated complex symbol such that

$$a_k^{'} + jb_k^{'} = (a_k + jb_k)\exp(j2\pi k f_c / f_{baud}) \qquad \ldots(5)$$

with a_k and b_k defined as in (1). This symbol rotation is due to the fact that the symbol period does not necessarily represent an integral number of cycles of the carrier frequency.

To make a QAM system into a CAP system, we simply dispense with the symbol rotation and apply the complex symbols directly to the passband shaping filters. Thus the discrete time transmitted sequence for a CAP system is:

$$x_n = \sum_k \left\{ a_k g_{I\ (n-Nk)} + b_k g_{Q\ (n-Nk)} \right\} \qquad \ldots(6)$$

where the passband pulses, $g_{I\,n}$ and $g_{Q\,n}$, are defined as above in equations (3) and (4). It is important to note, therefore, that CAP and QAM systems are not compatible unless the symbol period is exactly as long as an integral number of periods of the carrier tone. This relationship can be expressed in terms of the number of samples per symbol and the sampling, carrier and baud frequencies:

$$N = f_s / f_{baud} = lf_s / f_c \qquad \ldots(7)$$

where l is a positive integer.

2.1.2 Decision Feedback Equalization

In order to achieve a high data rate using a single carrier system such as CAP, it is necessary to have a relatively high symbol rate. On the UTP channel, such transmission is only possible if we can somehow eliminate the Inter-Symbol Interference (ISI) which is due to the channel dispersion. An equalizer is used to perform this task. In this work, the CAP systems considered use decision feedback equalization. The block diagram of a generalized decision feedback equalizer (DFE) with complex coefficients is shown in Figure 3.

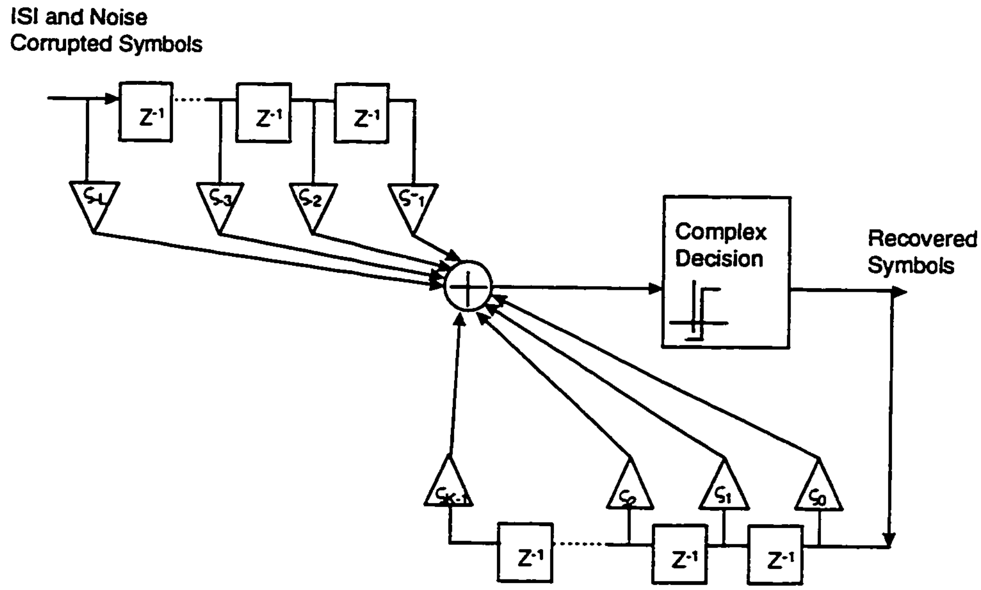

Figure 3: DFE Block Diagram

The DFE consists of an L-tap linear feed-forward section, the purpose of which is to cancel pre-cursor inter-symbol interference (ISI), and a K-tap feed-back section which serves to cancel the post-cursor ISI. Since the feedback section takes input from the decision device or quantizer, the DFE is a non-linear filter.

In this work, the channel is assumed to be static. Therefore, it is reasonable to first train the equalizer using an adaptive algorithm such as the Least Mean Square (LMS) algorithm and then freeze the coefficients for the actual performance simulation. The mathematics of the DFE and LMS algorithm are well treated in the literature and so they will not be discussed any further in this work. Interested readers are referred to the excellent paper by Qureshi, [51], and the texts by Proakis [49] and Haykin [24] for details.

2.2 CMFB-DMT

2.2.1 Some Generalities About Multicarrier Modulation

Before we embark upon any discussion of multicarrier modulations such as CMFB-DMT and FFT-DMT, it is worthwhile to discuss in general terms the differences between multicarrier modulation and the classical single carrier approach.

In single carrier systems like the CAP systems considered in this work, data is transmitted serially using some symbol rate which is a function of the desired data rate and the number of bits carried by the constellation. For scenarios such as transmission at ADSL or VDSL data rates over UTP, the symbol period is, in general, small compared to the channel impulse response which, for UTP, can have duration on the order of a millisecond. As a result, the signal is subject to a significant amount of ISI and an equalizer is required to recover the symbols. Note that one could conceive of some sort of pre-distortion filtering scheme to reduce or even eliminate the equalization requirement [11]. Such schemes are very sensitive to the quality of the estimate of the channel characteristics and, in a sense, only move the complexity of the equalizer from the receiver to the transmitter.

In a multicarrier system, the approach is to transmit data using a number of narrow bandwidth FDM signals simultaneously as illustrated in Figure 4.

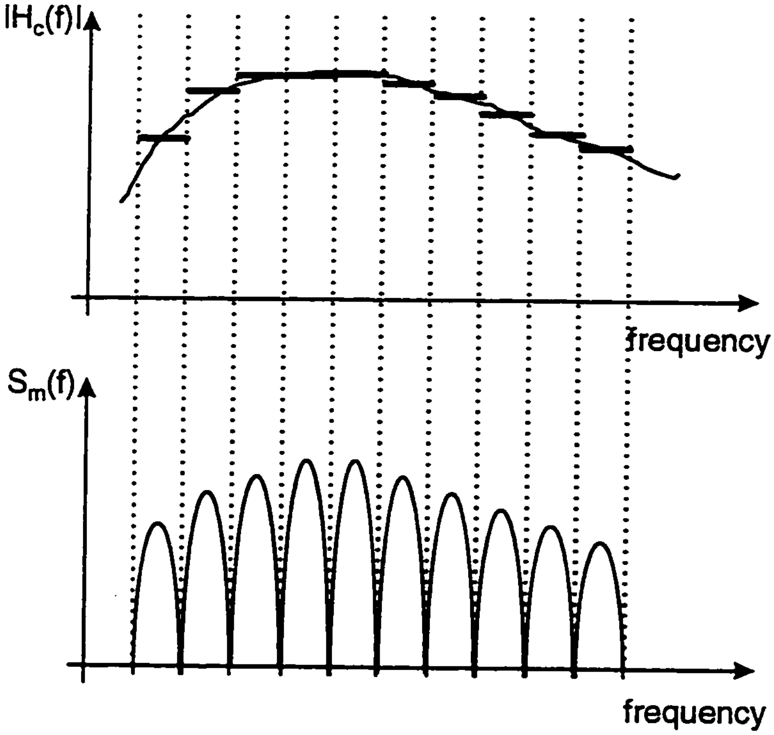

Figure 4: Channel Frequency Response (Hc) and Multicarrier Spectrum (Sm)

In order to obtain the full benefit of multicarrier signaling, the bandwidth of the component signals must be narrow enough to ensure that the channel behaves as closely as possible to an ideal channel for each component signal. That is to say that the channel magnitude response and noise PSD are both essentially flat within the band of each component signal [49]. With reference to Figure 4 note that, for a finite number of sub-channels, the nearness to ideality of the channel characteristic observed by each component signal can vary. For the scenario illustrated in Figure 4, we should expect the aggregate performance to be dominated by the performance of the low-frequency sub-channels which clearly do not experience an ideal channel response.

The narrow sub-band requirement has a time domain implication as well. Those familiar with Fourier transform properties or digital filter design [48] should know that a narrow bandwidth pass-band filter is by necessity a relatively long one. Each of the narrow, spectrally isolated signals of a multicarrier system uses much longer time domain pulses than single carrier systems. The impact of ISI in a multicarrier system is dramatically reduced by virtue of the fact that the symbol period on each sub-channel is longer than the channel spread. The long symbol periods used in multicarrier schemes also offer an advantage in the presence of impulse noise since impulse noise events are likely to span fewer symbol periods [9].

2.2.2 CMFB-DMT System Overview

CMFB-DMT is a multicarrier PAM system in which the sub-carrier signals are in-band generated using a PR cosine modulated filter bank ([52], [54], [59], [60]). A simplified block diagram for a CMFB-DMT system appears below in Figure 5. The synthesis and analysis filter banks are arranged in what is termed a transmultiplexor configuration [63]. In the CMFB-DMT system, serial data from the information source first passes through a block which converts it into symbolic vectors. This is a two step process. The serial data is first parsed into frames – each frame contains all of the data to be transmitted by one DMT symbol. In the second step, the data in each frame is divided among the sub-channels based upon the computed bit distribution. A single PAM symbol is chosen for each sub-channel and these symbols are scaled to affect the desired spectrum shape. Thus, at the output of the first block, we have a vector of symbolic data which can be applied to the input of the transmit or synthesis filter bank to generate the transmitter output for a single DMT symbol. After the synthesis transform, the output vector of waveform samples is converted to serial form which is then routed to the D/A converter. The vector to serial conversion is complicated by the fact that CMFB-DMT symbols overlap – it is necessary to add up all of the overlapping samples in order to generate the output waveform during a single symbol period. After the transmitter D/A converter, the DMT signal passes through the channel and picks up additive noise. At the receiver, the signal is sampled, a linear equalizer may be applied, and the samples of the received waveform are organized into vectors. The vectors of waveform data are next applied to the receiver or analysis transform and the resultant output may be input to an optional post-detection combiner. The vector signal is next input to a decision device which incorporates a PAM slicer for each sub-channel. Finally, the vector of recovered PAM symbols is converted back into a serial data sequence and sent to the data sink.

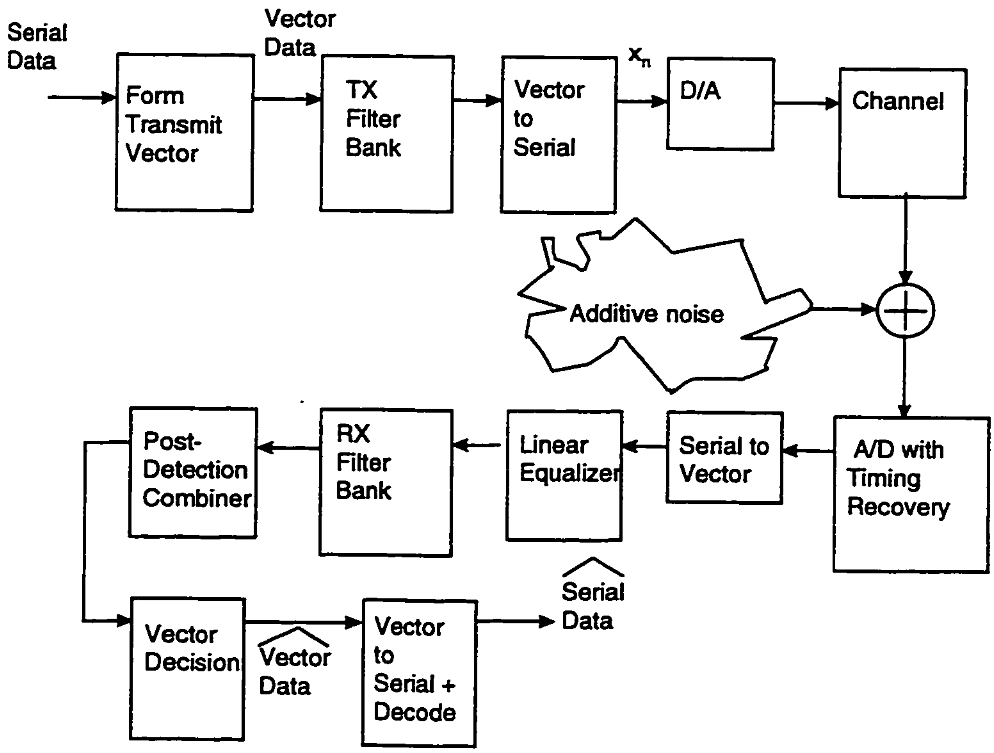

Figure 5: CMFB-DMT System

The transmitted sequence in a CMFB-DMT system is formulated as follows:

$$x_n = \sum_{j=1}^{M} \left\{ \sum_{k} \left(a_{j,k} g_{j,n-kM} \right) \right\} \qquad \ldots(8)$$

where M is the number of sub-channels in the filter bank, $a_{j,k}$ represents the PAM symbol on sub-channel j for the k^{th} symbol period and $g_{j,n}$ is the impulse response of the j^{th} filter in the synthesis bank. Note that the components of x_n associated with fixed k represent the computational results of a single application of the synthesis transform (filter bank). The filter impulse responses, $g_{j,n}$, in (8) are actually longer than M samples. The CMFB-DMT symbols can still be transmitted at intervals of M samples due to the shift orthogonality property of PR-CMFB's. This property is most concisely described by the following equations:

$$r_{ij,n} = g_{i,n} * g_{j,N_c-n}$$
$$r_{ij,lM} = \begin{cases} 1, \text{ for } l = 0 \text{ and } i = j \\ 0, \text{ for } l \neq 0 \text{ or } i \neq j \end{cases} \quad \ldots(9)$$

where l is some integer and N_c is the filter length. The shift-orthogonality of PR cosine modulated filter banks as well as the compact support of the filters and their effectively limited bandwidth indicate that they can be termed M-band wavelet filter banks. It is this association with wavelet concepts that has caused some authors to term CMFB-DMT "Discrete Wavelet Multitone" or DWMT. Currently, there is vast array of subject matter associated with the term "wavelet" including a variety of modulations based upon various types of wavelet transform. One such modulation is wavelet packet modulation as discussed in [20], [39], and [40]. Due to the potential for confusion, it seems sensible to specify exactly what type of wavelet filter bank is under consideration and so, in this work, the term CMFB-DMT is used.

2.2.3 CMFB Structure and Design

Cosine modulated filter banks are rather elegant in that both the analysis filters, $h_{k,n}$, and synthesis filters, $g_{k,n}$, are all modulated versions of the same low-pass prototype, $h_{lp\ n}$. An advantage of this structure is that they can be implemented as fast transforms as indicated in [42], [52], and [54]. For the PR cosine modulated filter banks considered in this work, the filter bank structure is represented by the equations below:

$$C_{k,n} = 2\cos\left[(2k+1)\frac{\pi}{2M}\left(n - mM + \frac{1}{2}\right) + (-1)^k \frac{\pi}{4}\right]$$
$$h_{k,n} = h_{lp\ n} C_{k,n} \quad \ldots(10)$$
$$g_{k,n} = h_{k\ (N_c-1-n)}$$

and the length of the various filter impulse responses is given by:

$$N_C = 2mM = gM \qquad \ldots(11)$$

where M is the number of sub-channels and m is some positive integer. The even, positive integer, g, in (11) is sometimes termed the "genus" [59] or "overlap factor" [54] of the filter bank. The following three figures show examples of a lowpass prototype response, the modulated filter impulse responses and the frequency responses of the modulated filters for an eight sub-channel PR-CMFB with $g = 4$.

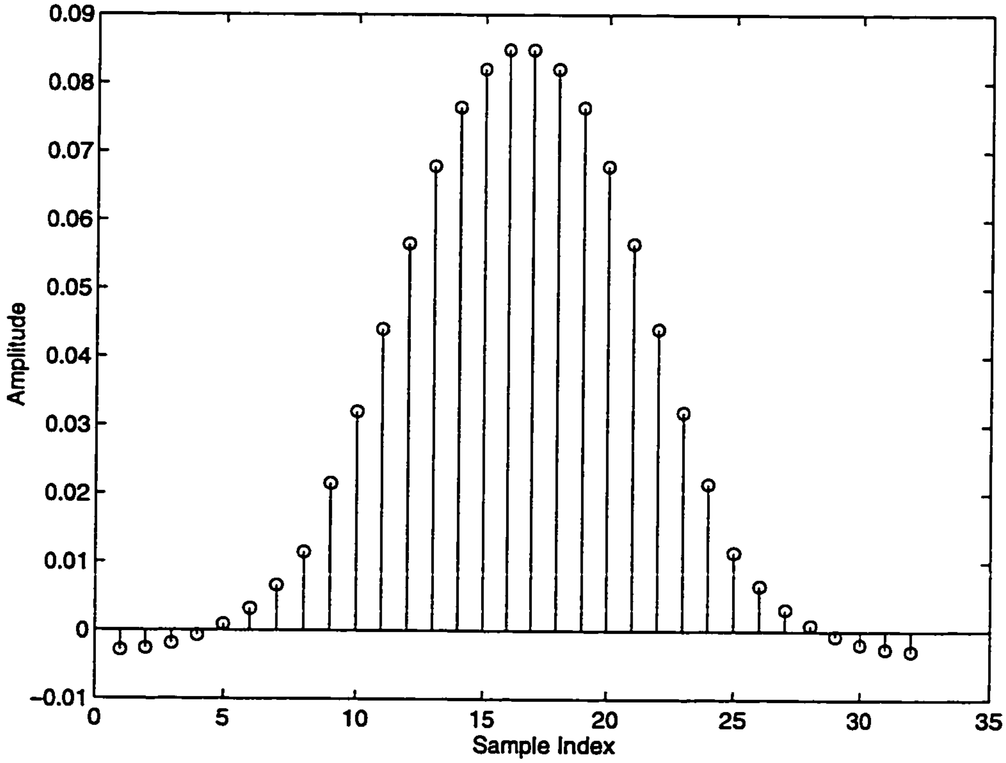

Figure 6: Discrete Impulse Response of Lowpass Prototype Filter for an Eight Sub-Channel PR-CMFB

As can be seen from Figure 6, the low-pass prototype filter has a shape very similar to the optimal pulse shapes determined for Orthogonal Frequency Division Multiplexing (OFDM) in [62].

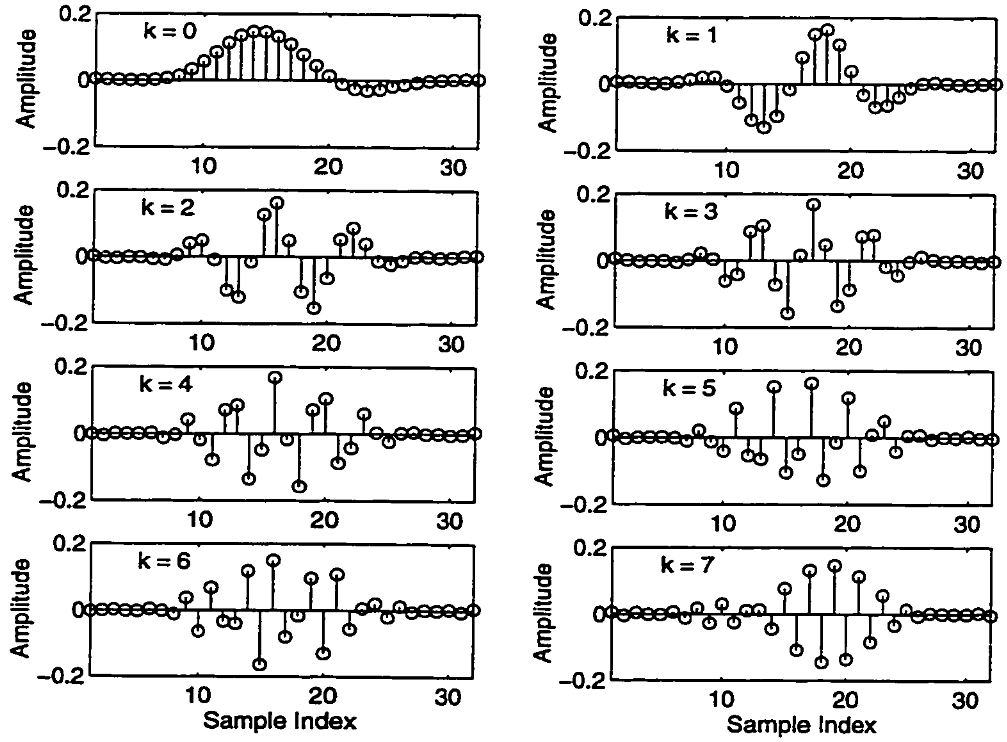

Figure 7: Analysis Filter Impulse Responses for an Eight Sub-Channel PR-CMFB

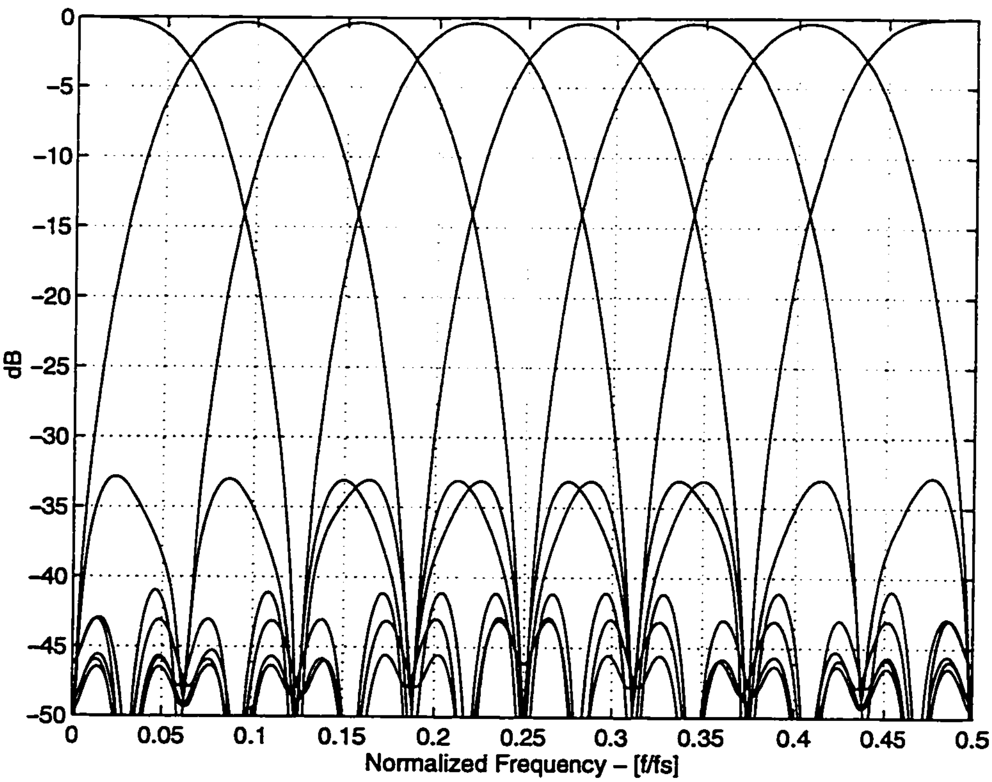

Figure 8: Analysis Filter Frequency Responses
for an Eight Sub-Channel PR-CMFB

The frequency responses in Figure 8, indicate one of the primary advantages of using PR-CMFB's in the context of multicarrier communications: the filters have very good spectral isolation. The first sidelobes of the various sub-channels are all at approximately -33 dB for the filter bank shown above. For the sake of comparison, the first sidelobes of FFT-DMT component signals are only at -13dB assuming that a rectangular window is used.

In simple terms, the design of a PR CMFB implies designing the low-pass prototype taking into account the desired sub-channel bandwidth and the constraints represented in (9) which are usually expressed in terms of the polyphase component matrix representation ([35], [47], [63]). There are a number of excellent references on the subject of PR-CMFB's and their design including references [35], [41], [53], [56], [63], and [64]. During the course of this work, the lossless lattice design of Koilpillai and

Vaidyanathan ([35], [63]) was found to be useful only for the design of relatively short filters (i.e. banks with few sub-channels and small genus number). This fact made the method of little value for this work since relatively large filter banks were required. In [52], Rizos et al. identify the quadratic constrained method of Nguyen [47] to provide good results for high order filters. This filter design procedure is not trivial to code, however, and software which uses it was unavailable due to patent restrictions. The method used to design all of the filter banks which were used in the simulations in this work was the iterative least squares design of Rossi et al. [53]. This highly efficient method was found to perform quite well for banks with the high order (512 sub-channels) used in this work.

2.2.4 Equalization and Post-Detection Combining

Two equalization methods for the CMFB-DMT system have been identified in the literature [52], [54]. The first of these is to use a linear FIR equalizer at the input to the receiver. The function of this filter is to shorten (or invert) the channel response. The second type of equalization is post-detection combining. As outlined in [54], the post-detection combiner forms a decision variable, $s_{k,i}$, for the k^{th} sub-channel at the i^{th} symbol instant by computing a linear combination of neighboring analysis filter outputs. This is formulated as follows:

$$s_{k,i} = \sum_{v \in \Omega, l \in T} \varsigma_{v,l} \theta_{v,l} \qquad \text{...(12)}$$

where Ω denotes the set of sub-channels which are considered by the combiner; T denotes the set of symbol instants; $\varsigma_{v,l}$ is the weight applied to the output of analysis filter v at instant l; and $\theta_{v,l}$ denotes the output of analysis filter v at instant l. We can think of the combiner as a two dimensional filter which acts in the time and frequency domains. This idea is illustrated below in Figure 9: the shaded area encompasses the detector outputs used by a 3x3 post detection combiner to compute the decision variable for sub-channel k at symbol instant t_0.

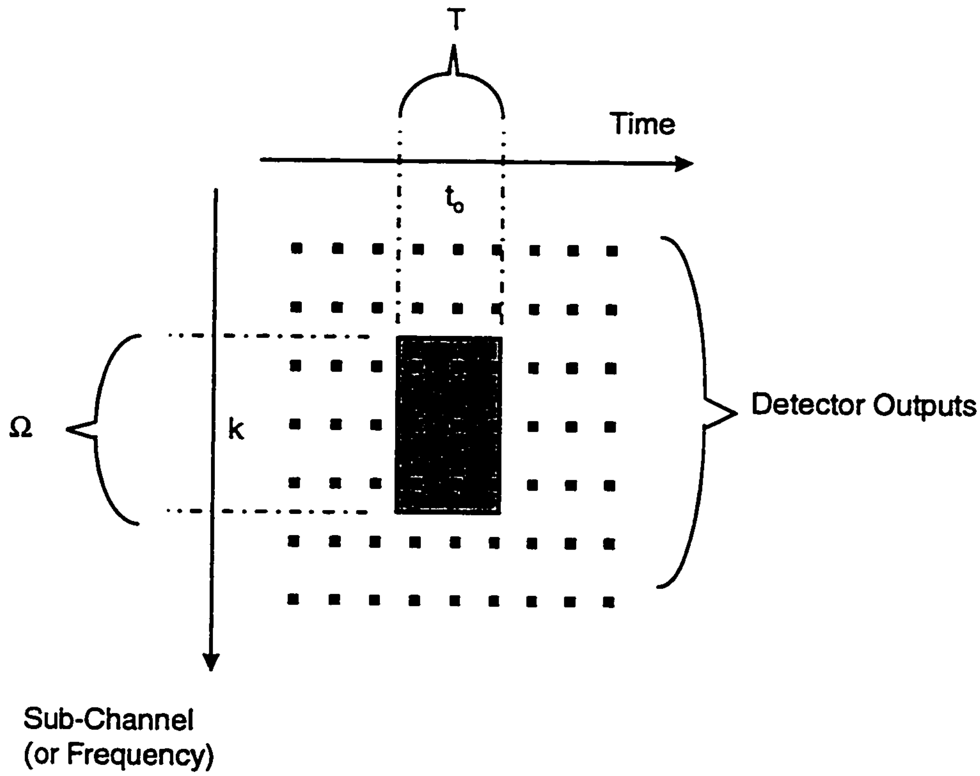

Figure 9: 3x3 Post Detection Combiner Span in the Time-Frequency Plane

Each CMFB sub-channel uses a unique set of post-detection combiner coefficients, $\varsigma_{v,l}$, in general. This makes implementing the combiner more complicated than implementing a simple FIR filter – particularly if it is to be adaptive.

There are drawbacks to using either the linear equalizer or post-detection combiner alone.

Using only the linear equalizer is complicated by the fact that the CMFB-DMT symbols overlap: even a small amount of residual distortion in the end-to-end channel can cause significant ISI and ICI. This means that the linear equalizer has to almost perfectly invert the channel response. This requirement translates to a large number of linear equalizer taps.

Used alone, post-detection combining can also require a large number of taps since the orthogonality properties of the CMFB pulses are very sensitive to distortion. The demodulation of the CMFB-DMT signal is performed "in-band" and each sub-channel carries unidimensional PAM. As a result, this scheme is also very sensitive to timing phase error. This is particularly true for the high frequency sub-channels (the eye width decreases with increasing frequency). The UTP channel has slightly non-linear phase along with significant amplitude distortion. After distortion by the UTP channel, the optimum sampling phase is generally *not the same* on all CMFB-DMT sub-channels. However, because the detector filtering is done simultaneously for all sub-channels using a block transform, all sub-channels must be sampled with the same phase. Since the post-detection combiner acts after down-sampling to the symbol rate, it has to work with whatever sub-optimal samples are obtained on all of the sub-channels. This implies that performance will be limited by those sub-channels which have the most damaging timing phase error.

Computational complexity and ease of implementation are of primary importance for ADSL and VDSL since they have an impact on the ultimate cost of the transceiver. The least complex equalization solution for CMFB-DMT incorporates both linear equalization and post-detection combining.

In this work, we will consider both linear equalization and idealized post-detection combining. The design of the FIR linear equalizers used in the simulations was based upon the optimum MSE criterion linear equalizer design suggested by Proakis in [49].

Post-detection combining, as identified in [54], is a generalization of linear equalization using the MSE criterion. From Proakis [49], we know that, under the condition of high SNR, the MSE equalization criterion is equivalent to the zero-forcing criterion. Based upon [51], the functionality of the optimum zero-forcing linear equalizer is to null all of the ISI within the temporal span of the equalizer. In this work, it is assumed that the ideal post-combiner functions in a similar manner. That is to say it nulls all of the interference terms within its two-dimensional span while retaining the cursor (or desired) tap. Interference outside of the span of the idealized combiner is unaffected. Noise enhancement due to post-detection combining is not modeled in this work.

2.2.5 Bit Allocation and Spectrum Shaping

At the heart of any multicarrier communications scheme are the elements of bit allocation and spectrum shaping. As indicated by [5], [49], and [55] it is best to optimize the both spectrum and bit allocation of a multicarrier system in order to maximize the capacity of the loop given the available bandwidth and power constraints. Note that this is in contrast to the ADSL specification which requires that the ADSL signal have an essentially flat power spectral density ([4], [15]). In [5], Barton identifies that using the non-optimized spectrum chosen by the ADSL standard committee incurs as much as a 6 dB performance penalty with respect to an optimized spectrum in the presence of cross-talk from dissimilar signals. In this work, the spectrum optimization and bit allocation were computed using a method derived from the optimal "water-pouring solution" mentioned in [29] and [49]. In the following pages, the mathematical developments behind the bit allocation and spectrum optimization are presented.

2.2.5.1 Optimization with AWGN Only

The k^{th} component sub-channel in the DMT signal carries an L_k-PAM constellation. The unscaled symbolic values are from the odd-integer set described by the following equation:

$$\{A_m\} = (2m - 1 - L_k), \quad m=1,2, \ldots L_k \qquad \ldots(13).$$

The aggregate number of bits per symbol, b_A, is defined to be:

$$b_A = \sum_{k\in\chi} \log_2(L_k) \qquad \text{...(14)}$$

where χ is defined to be the set of all sub-channels used in the CMFB-DMT signal. The bit rate, R, can be computed by multiplying b_A by the symbol rate, f_{baud}:

$$R = b_A f_{baud} = b_A \frac{f_s}{M} \qquad \text{...(15)}$$

where f_s denotes the sampling rate and M is the number of samples per symbol (equivalent to the number of sub-channels in the CMFB).

The probability of a symbol error on the k^{th} PAM sub-channel, $P_{e\,k}$ is approximated as follows:

$$P_{e\,k} = 2\left(\frac{L_k - 1}{L_k}\right) Q\left(\frac{d_{RX\,k}}{2\sigma_k}\right) \approx 2Q\left(\frac{d_{RX\,k}}{2\sigma_k}\right) \qquad \text{...(16)}$$

where σ_k is the standard deviation of the in-band Gaussian noise on sub-channel k and $d_{RX\,k}$ is the distance between adjacent constellation points on this sub-channel at the receiver. The value of $d_{RX\,k}$ is approximated by:

$$d_{RX\,k} \approx \left|H_c(f_k)\right| d_{TX\,k} \qquad \text{...(17)}$$

where $d_{TX\,k}$ is the transmitted constellation distance on the k^{th} sub-channel and $H_c(f_k)$ is the channel frequency response evaluated at the center frequency of the k^{th} sub-channel. Based upon equations (16) and (17), for a given error probability on the k^{th} sub-channel, we require that:

$$\gamma = \left(\frac{d_{RX\,k}}{2\sigma_k}\right)^2 \qquad \text{...(18)}$$

where γ is a quantity proportional to SNR and equal to approximately 14.5 dB for an SER of 1e-7. Note that the required value of γ is the same on all sub-channels by this analysis.

Now, the average transmitted power on the k^{th} sub-channel, P_k, (normalized to the characteristic impedance of the line and the symbol period) is defined to be:

$$P_k = \frac{1}{12}\left(L_k^2 - 1\right)d_{TXk}^2 \qquad \text{...(19)}$$

and the normalized aggregate power is given by:

$$P_{TX} = \sum_{k\in\chi} P_k \qquad \text{...(20).}$$

We can solve (19) for L_k and make substitutions taking into account equations (17) and (18) to yield:

$$L_k = \sqrt{1 + \frac{3P_k\left|H_c(f_k)\right|^2}{\sigma_k^2\gamma}} \qquad \text{...(21).}$$

After [5], the optimum bit allocation and spectrum shape are the ones which maximize the data payload (capacity) of the loop taking into account the transmit power constraint. We can formulate this as a Lagrange optimization problem with Lagrangian:

$$L(P_k) = \sum_{k\in\chi}\frac{1}{2}\log_2\left(1 + \frac{3P_k\left|H_c(f_k)\right|^2}{\sigma_k{}^2\gamma}\right) - \lambda\sum_{k\in\chi}P_k \qquad \text{...(22).}$$

Setting the derivative of the Lagrangian equal to zero, we can solve for the optimal values of P_k:

$$P_k = P_o - \frac{\sigma_k^2 \gamma}{3\left|H_c(f_k)\right|^2} \qquad \ldots(23)$$

where P_o is some constant. Note that the power distribution of (23) assumes the use of infinite granularity in allocating bits to the various sub-channels. The form of equation (23) is identical to that of the "water pouring" solution described by Proakis [49].

What remains is to describe how to apply (23) in finding a practical bit allocation and optimized spectrum – that is to say a bit allocation and associated spectrum using finite bit granularity. In this work, the bit allocation used unit bit granularity – that is to say that each sub-channel was allocated an integral number of bits. The bit allocation and spectrum shaping was an iterative process which is summarized by the following steps:

1. Choose a value for P_o (using a simple search algorithm with a small incremental step size).

2. Compute P_k using (23).

3. Compute the number of bits allocated to each sub-channel using the following relationship:

$$bits_k = RND\left\{\frac{1}{2}\log_2\left(1 + \frac{3P_k\left|H_c(f_k)\right|^2}{\sigma_k^{\,2}\gamma}\right)\right\} \qquad \ldots(24)$$

where the operator *RND{}* denotes selecting the closest integer within the set of acceptable bit loads. For this work, the acceptable set of bit loads for each PAM sub-channel was chosen to be integers between 1 and 7 bits.

4. Add up the variables, $bits_k$, to find the total number of bits allocated, b_A. If the current number of bits per symbol is below the desired number of bits, go back to step 1 (in this case P_o is too low). If the current number of bits exceeds the desired number by

more than the number of sub-channels, go to step 1 (in this case the aggregate power is too high).

5. Eliminate some high frequency sub-channels, if necessary, to achieve the desired value for b_A.

6. Compute final values of P_k to guarantee that the symbol error rates on each sub-channel are equal. This final step is performed using the following equation which is simply a re-arrangement of(24):

$$P_k=(2^{2b_k}-1)\frac{\gamma\sigma_k}{3\left|H_c(f_k)\right|^2} \qquad ...(25).$$

The following figures show the normalized sub-channel powers and bit allocation as computed using the procedure outlined above for a 6 Mbps, 512 sub-channel CMFB-DMT signal to be sent over 2000 m of Category 3 UTP with AWGN as the only impairment.

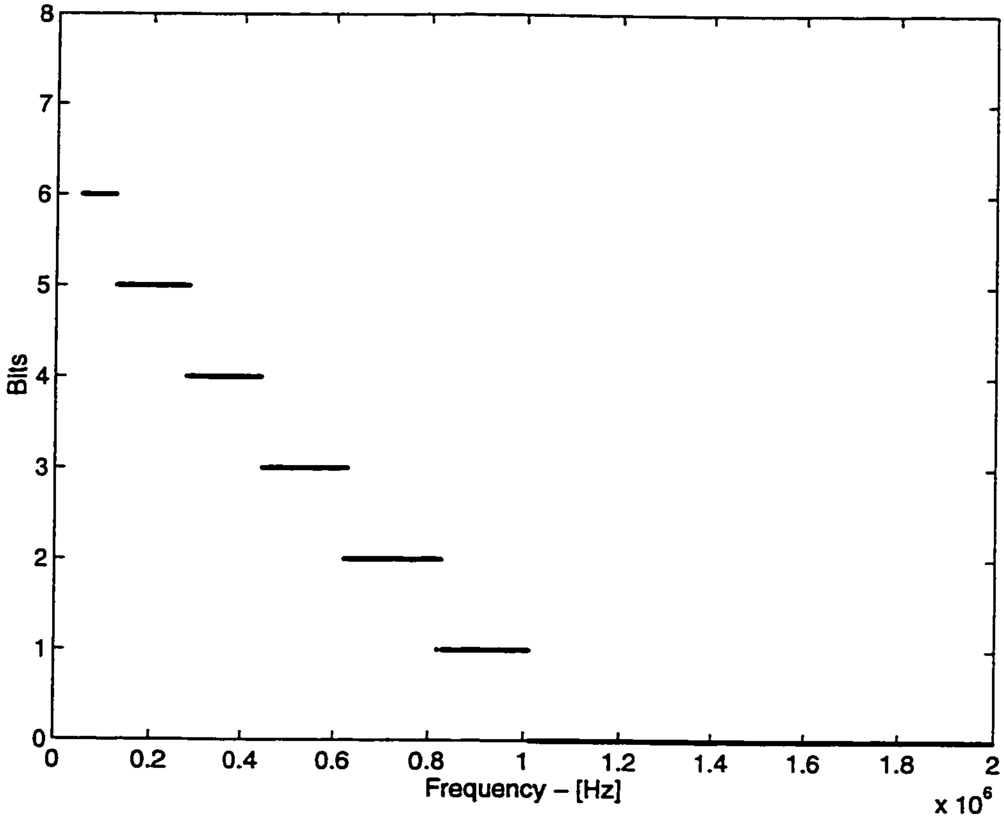

Figure 10: Sample Bit Allocation Results

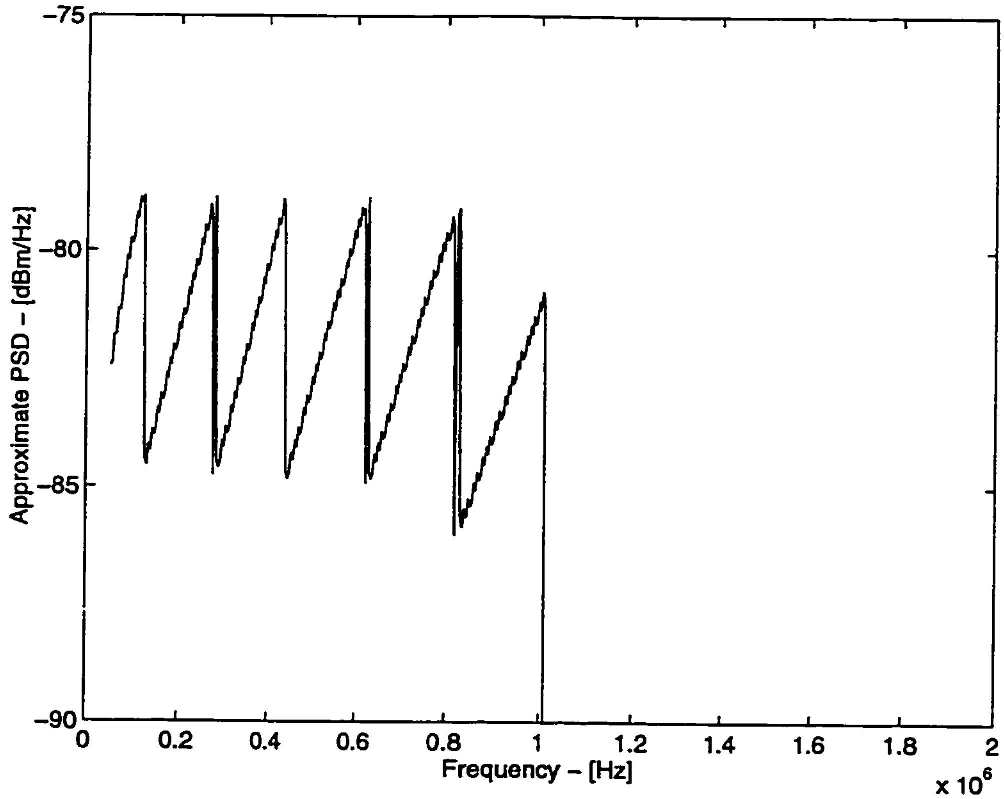

Figure 11: Sample Optimized Spectrum

As can be seen from Figure 11, the sub-channel power distribution has a "saw-tooth" character. This is due to the final error rate equalization step which makes up for the rounding operation in step 3. The saw-tooth deviations are within approximately +/-3 dB due to the fact that the SER versus SNR curves for the possible PAM constellations are all 6 dB apart. In this case, AWGN is the only additive noise and the available SNR on each sub-channel falls off with increasing frequency. This is reflected in the bit allocation shown in Figure 10 – the number of bits allocated to the sub-channels decreases with frequency.

2.2.5.2 Optimization With AWGN and Self-FEXT

It is fairly straight-forward to adapt the optimization described in the previous section to include self-FEXT (please refer to section 3.3 FEXT for a description of the self-FEXT impairment).

Let us assume that self-FEXT contributes a zero-mean additive Gaussian noise – which is independent of the AWGN – to the output of each sub-channel. Further, assuming that the standard deviation of the FEXT noise observed on the k^{th} sub-channel is given by:

$$\sigma_{FEXT\,k} = P_k G(f_k) \qquad \ldots(26)$$

where P_k is defined as in the previous section and $G(f_k)$ denotes the FEXT power gain at the center frequency of the kth sub-channel, we can reformulate the Lagrangian as follows

$$L(P_k) = \sum_{k\in\chi} \frac{1}{2}\log_2\left(1 + \frac{3P_k\left|H_c(f_k)\right|^2}{\left(\sigma_k^{\,2} + P_k G(f_k)\right)\gamma}\right) - \lambda \sum_{k\in\chi} P_k \;\ldots(27).$$

Using Matlab™'s symbolic math package, (27) was solved for the optimum values of P_k. This solution has the form of a quadratic root:

$$P_k = -\frac{\sigma_k^2\gamma G(f_k) - \frac{3}{2}\sigma_k^2\left|H_c(f_k)\right|^2}{\gamma G^2(f_k) + 3\left|H_c(f_k)\right|^2} \pm \ldots.$$

$$\frac{\left\{3\sigma_k^2\left|H_c(f_k)\right|^2\left(3P_o\log_2(2)\sigma_k^2\left|H_c(f_k)\right|^2 + 2\gamma G^2(f_k) + 6G(f_k)\left|H_c(f_k)\right|^2\right)\right\}^{0.5}}{2\sqrt{P_o\log_2(2)}\left(\gamma G^2(f_k) + 3\left|H_c(f_k)\right|^2\right)}$$

$$\ldots(28).$$

The six-step procedure described in the previous section was adapted to compute the bit loading and power distribution taking into account the impact of self-FEXT.

2.3 FFT-DMT

2.3.1 FFT-DMT System Overview

FFT-DMT is a multicarrier QAM system which uses a simple IFFT/FFT pair as the transmit and receive filter banks ([4], [49]). The block diagram of the FFT-DMT system is shown in Figure 12. As can be seen from Figure 12, the FFT-DMT system and the CMFB-DMT of Figure 5 are very similar with the exception of the fact that the FFT-DMT system includes some new blocks and the fact that FFT-DMT symbols do not overlap. In the FFT system, serial data is first parsed into frames which are used to form the transmitted vectors. The transmitted vector associates a QAM symbol with each FFT-DMT sub-channel of which there are a maximum of $N_{FFT}/2-1$ (excluding DC and $f_s/2$) assuming an N_{FFT}-point transform. The size of the QAM constellation on a given sub-channel is chosen based upon bit allocation computations similar to those described earlier for the CMFB-DMT system. The output of the IFFT, which is the transmit or synthesis transform, must be real. Therefore, as described in [49], the symbolic transmit vector is constructed to incorporate the necessary conjugate symmetry. After the synthesis transform, the resulting vector of samples is converted to serial form and, if desired, a cyclic prefix (CP) is added. Next, the DMT signal passes through the end-to-end channel which is made up of the transmit D/A, the UTP and the receive A/D. The sequence of received samples is next applied to an FIR filter or equalizer which is used to shorten the spread of the channel impulse response. After the equalization step, the serial samples are organized into vector symbols and the cyclic prefix, if used, is removed. Next the FFT, or analysis transform is applied. At the output of the receive transform, it is possible to apply a frequency domain equalizer to provide AGC and to correct any remaining phase error before slicing the complex symbols on each sub-channel. Vector data at the output of the decision block is finally decoded and returned to serial form.

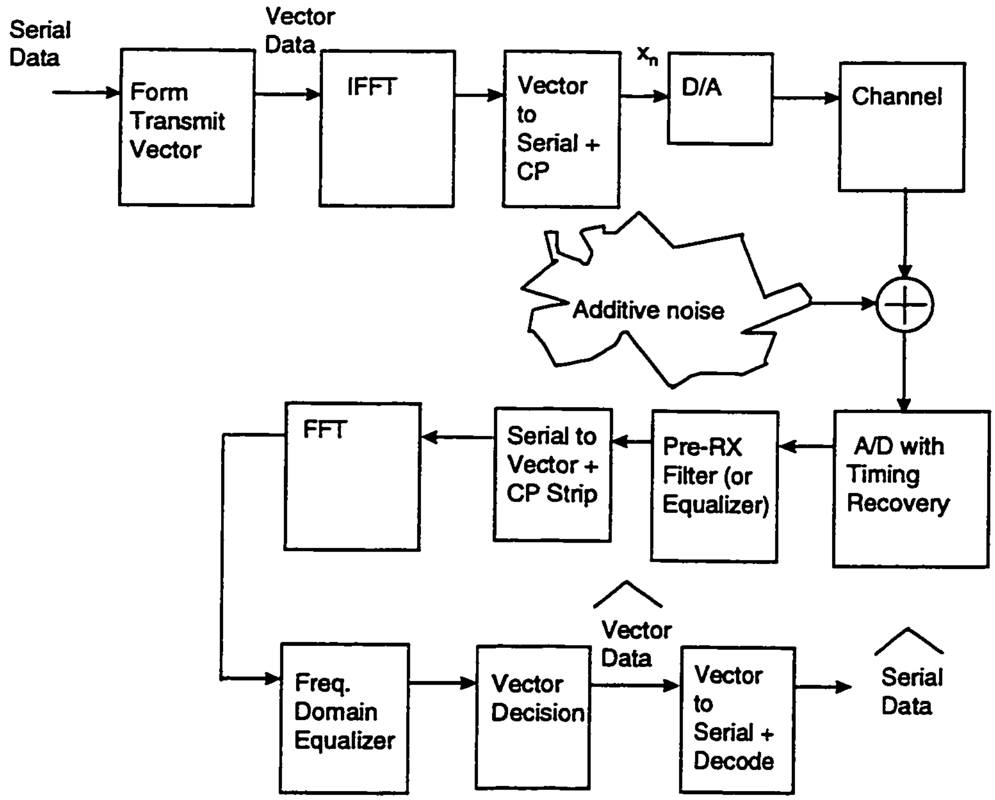

Figure 12: FFT-DMT Block Diagram

The transmitted sequence in an FFT-DMT system can be formulated in a way analogous to the transmitted sequence for CMFB-DMT:

$$x_n = \mathrm{Re}\left\{\sum_{m=1}^{M}\left\{\sum_{k} 2\left(c_{m,k}\, g_{m,n-kN'}\right)\right\}\right\} \qquad \ldots(29)$$

where $c_{m,k}$ represents a complex symbol transmitted on the mth sub-channel during the kth symbol period; N' represents the symbol duration in samples (the length of the FFT plus cyclic prefix); and $g_{m,n}$ are truncated complex exponential sequences – the basis functions for the FFT expansion including the cyclic prefix samples. The impulse responses, $g_{m,n}$, are given by:

$$g_{m,n} = \begin{cases} K_m \exp\left(j2\pi mn / N_{FFT}\right) + K_m^* \exp\left(-j2\pi mn / N_{FFT}\right), & n = -\upsilon,\ldots,N_{FFT}-1. \\ 0, & \text{else.} \end{cases}$$

...(30).

In equation , K_m is a scale factor used to affect the desired power spectral level on the m^{th} sub-channel; N_{FFT} is the FFT size; and υ is the cyclic prefix length. The symbol duration, N', in samples is given by:

$$N' = N_{FFT} + \upsilon \qquad ...(31).$$

Note that the cyclic prefix has the effect of reducing the capacity of the link by a factor of $N_{FFT}/N_{FFT}+\upsilon$.

Two major differences between FFT-DMT and CMFB-DMT should now be clear. In FFT-DMT, the symbols do not overlap and each narrow-band component signal carries a 2-dimensional (complex) constellation. In CMFB-DMT, the symbols overlap in general and each component signal carries unidimensional PAM.

2.3.2 Equalization for FFT-DMT

The design of the FIR linear equalizer at the input of the FFT-DMT receiver is an interesting problem in itself. The goal is to shorten the impulse response of the channel to a duration less than the length of the cyclic prefix. This is a classical inverse system modeling problem as defined in [19] represented by the block diagram shown in Figure 13. The goal is to find a short FIR filter, w_n, which, when convolved with the channel impulse response, provides a temporally shorter end-to-end impulse response. The shortened response must be such that it minimizes the error with respect to some Target Impulse Response (TIR), $b_{TIR\,n}$, which must also be determined by the design process.

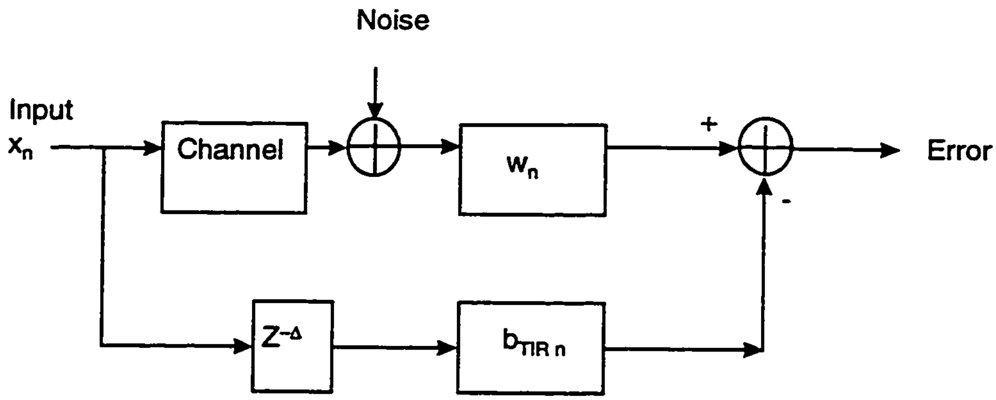

Figure 13: Equalizer Design Block Diagram

As indicated by [13], the time-domain LMS algorithm is not suitable for this application due to convergence problems. Since the channel response is expected to be essentially static, we can opt for an approach where the equalizer is trained based upon data from channel characterization. The design or training of a Time domain EQualizer (TEQ) can be thought of as a three step process: first we characterize the channel response; then we compute the TIR, $b_{TIR\,n}$; and, finally, we compute the TEQ response, w_n. In this work, knowledge of the channel response is assumed for the sake of simplicity. In real systems [4], [14], the channel response is determined by a characterization step during the link setup.

As one might expect, there are a number of ways to go about finding w_n and $b_{TIR\,n}$. The various design procedures can be classified in terms of the equalization criteria and the constraints used.

In [2], an optimum equalization criterion is defined for DMT. This criterion is to maximize a figure of merit called the geometric SNR which is defined as follows:

$$SNR_{geom} \approx \prod_{i \in \chi} \left(\frac{P_{s,i} \left(B_{TIR\,i} \right)^2}{\Phi_{n,i} \left| W_i \right|^2} \right)^{\frac{1}{N_{FFT}/2}} \qquad \ldots(32)$$

where P_i is the signal power in the i^{th} FFT-DMT sub-channel, $B_{TIR\,i}$ and W_i are the i^{th} DFT coefficients of the TIR and TEQ respectively, and $\Phi_{n,i}$ represents the noise power observed in the band of the i^{th} sub-channel. This is similar to the familiar MSE criterion due to the fact that the noise spectrum is taken into account. The design of the geometric TEQ requires finding the TIR which maximizes (32) and satisfies a constraint to exclude the trivial solution and then solving for w_n. Unfortunately, finding the optimum TIR in terms of the geometric SNR criterion requires solution of a constrained non-linear programming problem which does not have a unique global optimum. This can be computationally expensive and is probably not a practical goal in a real system. In any case, the extra computation required to compute the geometric TEQ does not seem to pay off: simulation results for the CSA loops in [2] show that the geometric TEQ offers only a 1 dB performance advantage compared to some other designs.

Two other TEQ design procedures commonly encountered in the literature are based directly upon the Mean Square Error (MSE) equalization criterion and two different constraints which are intended to exclude the trivial (w_n, $b_{TIR\,n}$, all zero) solution. These constraints are termed the Unit Tap Constraint (UTC) and the Unit Energy Constraint (UEC).

In the MSE-UTC design as discussed in [3] and [38], the TIR, $b_{TIR\,n}$, is constrained to have one tap with unit value. While using the UTC can provide a computationally efficient design, from a filter design perspective, it seems to be an unusual constraint. Using the UTC also has the disadvantage of adding another parameter to optimize during the design process: namely the location of the unit tap in the TIR.

For the MSE-UEC design, the TIR is constrained to have unit energy. This is a more familiar constraint in digital filter design and it is known (from [3]) to provide better performance than the UTC. Detailed mathematical developments for the MSE-UEC TEQ design are provided in [3].

In this work, TEQ design was performed using the UEC along with a Least Squares (LS) equalization criterion. The optimum TEQ in terms of the LS criterion minimizes the noiseless squared error between the equalized impulse response, $h_c * w_n$, and the TIR, $b_{TIR\,n}$. This equalization criterion is similar in spirit to the peak distortion or "zero-forcing" criterion since it considers only the end-to-end linear impulse response. The LS-UEC design can either be formulated exactly as described in [3] for the MSE-UEC design with the noise terms set to zero or as proposed in [45]. While the LS criterion is not the optimum equalization criterion, using it simplifies the TEQ design because it does not require an estimate of the noise auto-correlation. This choice should not have a significant effect on the actual performance results. The simulations which follow only consider straight lengths of UTP and so the channel frequency response is always smooth and monotonic with no nulls. The sub-channel bandwidths used in the simulations are narrow enough to ensure that both the TEQ and channel frequency responses are close to uniform within any sub-channel. Therefore, for moderate to high SNR, it is safe to say that the results of the MSE-UEC and LS-UEC designs are equivalent.

During the course of this work, it was found to be advantageous to set the length of the TIR to less than the length of the cyclic prefix. Most of the error in the shortened channel impulse response is localized near the ends of what corresponds to the TIR. By making the TIR shorter than the CP, the effects of the error in the shortened response are reduced. For the performance simulations, the TIR length was set to ½ of the CP duration.

2.3.3 Bit allocation and Spectrum Shaping

Bit allocation and spectrum shaping for FFT-DMT and CMFB-DMT are very similar. The major difference is that FFT-DMT sub-channels carry QAM as opposed to PAM. What follows is a summary of the mathematical developments for the optimum spectrum shapes in the presence of AWGN and self-FEXT.

2.3.3.1 Optimization with AWGN Only

The k^{th} sub-channel in the FFT-DMT signal carries a square L_k-QAM constellation. The symbolic values of the various QAM constellations are assumed to lie on an odd integer grid as depicted in Figure 14 for 16 QAM.

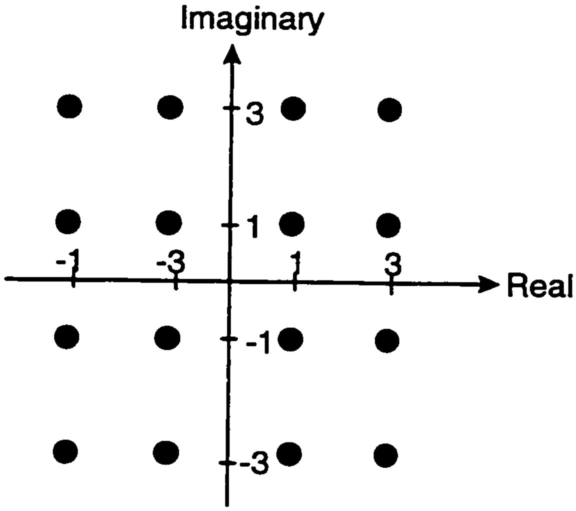

Figure 14: 16-QAM Constellation

We can define the aggregate number of bits per symbol, b_A, as follows:

$$b_A = \sum_{k \in \chi} \log_2(L_k) \qquad \text{...(33)}$$

where χ is defined to be the set of all sub-channels used in the FFT-DMT signal. As for CMFB-DMT, the bit rate, R, is given by:

$$R = b_A f_{baud} = b_A \frac{f_s}{N'} \qquad \text{...(34)}$$

where f_s denotes the sampling rate, f_{baud} is the baud rate, and N' is the number of samples per symbol (i.e. the transform size plus the length of the cyclic prefix).

We can approximate the probability of a symbol error on the kth QAM sub-channel, $P_{e\ k}$, as:

$$P_{e\,k} = 4\left(\frac{\sqrt{L_k}-1}{\sqrt{L_k}}\right)Q\left(\frac{d_{RX\,k}}{2\sigma_k}\right) \approx 4Q\left(\frac{d_{RX\,k}}{2\sigma_k}\right) \qquad \ldots(35)$$

where σ_k is the standard deviation per dimension of the in-band Gaussian noise on sub-channel k and $d_{RX\,k}$ is the distance between adjacent constellation points at the decision device. Equation (35) represents the sum of the error probabilities of the two quadrature PAM signals which make up the QAM signal. The value of $d_{RX\,k}$ is approximated by:

$$d_{RX\,k} \approx \left|H_c(f_k)\right| d_{TX\,k} \qquad \ldots(36)$$

where $d_{TX\,k}$ is the transmitted constellation distance. Based upon equations (35) and (36), for a given error rate on the k^{th} sub-channel, we require that:

$$\gamma = \left(\frac{d_{RX\,k}}{2\sigma_k}\right)^2 \qquad \ldots(37).$$

The quantity, γ, is equal to approximately 14.73 dB for a SER of 1e-7.

Now, the transmit power on the k^{th} sub-channel, P_k, (normalized to the characteristic impedance of the line and the symbol period) is defined to be:

$$P_k = \frac{1}{6}\left(L_k - 1\right)d_{TX\,k}^2 \qquad \ldots(38).$$

Equation (38), is exact for square constellations. It is an upper bound for the CROSS constellations (odd number of bits) in the ADSL standard[4].

The normalized aggregate power is given by:

$$P_{TX} = \sum_{k \in \chi} P_k \qquad \ldots(39).$$

We can solve (38) for L_k and substitute expressions for $d_{TX\,k}$ and $d_{RX\,k}$ to yield:

$$L_k = 1 + \frac{3P_k\left|H_c(f_k)\right|^2}{2\sigma_k^2\gamma} \qquad \ldots(40).$$

Assuming, once again, that the optimum bit allocation and spectrum shape maximize the data payload while taking into account the transmit power constraint (as in [5]), we can formulate a Lagrange optimization problem with Lagrangian:

$$L(P_k) = \sum_{k \in \chi} \log_2\left(1 + \frac{3P_k\left|H_c(f_k)\right|^2}{2\sigma_k^2\gamma}\right) - \lambda \sum_{k \in \chi} P_k \qquad \ldots(41).$$

From the Lagrangian, the optimal values of P_k are given by:

$$P_k = P_o - \frac{2\sigma_k^2\gamma}{3\left|H_c(f_k)\right|^2} \qquad \ldots(42)$$

where P_o is some constant.

In the simulations, the number of bits on each sub-channel was constrained to be an integer between 2 and 14 bits. The iterative procedure described in Section 2.2.4.1 was used in conjunction with equations (40) and (42) to find the optimum integer bit allocations and spectrum shapes.

2.3.3.2 Optimization With AWGN and Self-FEXT

Taking the same assumptions as in Section 2.2.4.2 we can re-formulate equation (41) to take into account the impact of self-FEXT. The new Lagrangian is:

$$L(P_k) = \sum_{k \in \chi} \log_2\left(1 + \frac{3P_k\left|H_c(f_k)\right|^2}{2\left(\sigma_k^2 + G(f_k)P_k\right)\gamma}\right) - \lambda \sum_{k \in \chi} P_k$$

$$\ldots(43)$$

where G is the FEXT gain response.

Solving for the optimum P_k's we obtain the following quadratic root form:

$$P_k = \frac{-1}{A}\left\{B \pm \sqrt{C}\right\}$$
$$A = 2P_o G(f_k)\left[\frac{2\gamma}{3}G(f_k) + \left|H_c(f_k)\right|^2\right]$$
$$B = \left(P_o\sigma_k^2\right)\left(\frac{4\gamma}{3}G(f_k) + \left|H_c(f_k)\right|^2\right)$$
$$C = \left(P_o\sigma_k^2\left|H_c(f_k)\right|^2\right)^2 + \frac{8\gamma}{3}P_o G^2(f_k)\left|H_c(f_k)\right|^2\sigma_k^2 + 4P_o G(f_k)\left|H_c(f_k)\right|^4\sigma_k^2$$

...(44).

This result and equation (40) were used with the iterative procedure described in Section 2.2.4.1 to obtain bit allocations and spectra using unit bit granularity for the simulations.

Chapter 3

CHANNEL AND IMPAIRMENT MODELING

The validity of any analysis of the performance of a communications system depends heavily upon the quality of the channel and impairment models used. The following sections describe the models used in this work for the UTP channel, AWGN, and self-FEXT. Discussions of three other notable impairments on the UTP channel, namely radio frequency interference, NEXT and impulse noise, are also included though their effects are not accounted for in the analysis and simulation results which follow.

3.1 The UTP Channel

Accurate modeling of the channel response in both the time and frequency domains is critical if one wishes to obtain meaningful time-domain simulation results. In the case of the UTP channel, it is necessary to model both the magnitude and the phase which is slightly non-linear. Neglecting to model the phase would produce a symmetric impulse response that looks nothing like the one-sided impulse response of UTP which is similar to that of an RLC circuit (see Figure 15).

As mentioned in Chapter 1, only straight lengths of twisted pair are considered in this work. This allows the use of the relatively simple modeling approach presented on the following pages. More complicated UTP networks which may include bridged taps can be modeled using the method in [46].

In this work, the UTP response was generated from primary constant (resistance, inductance, capacitance, conductance) data provided in [16]. What follows is a brief description of the procedure. Using Matlab™, the parametric curves suggested in [16] were fit to the primary constant data and these functions were used to compute values for R_p, L_p, C_p, G_p at evenly spaced frequencies corresponding to the bins of an FFT. Next, the resultant frequency dependent data was used to compute the propagation constant γ_p as a function of frequency. The relationship used to compute γ_p was the following:

$$\gamma_p(f) = \sqrt{\frac{R_p + j\omega L_p}{G_p + j\omega C_p}} = \alpha_p + j\beta_p \qquad \ldots(45)$$

which should be familiar to readers who have an understanding of transmission line theory [12]. The frequency response of the twisted pair loop of length l_{UTP} was generated by computing the following:

$$H_{UTP}(f) = e^{-\gamma_p(f) l_{UTP}} \qquad \ldots(46).$$

Finally, the (discrete-) time-domain impulse response of the twisted pair was computed by performing an inverse FFT on the samples of the frequency response. The method outlined above was found to provide satisfactory impulse responses as long as enough points were used in the frequency and time domains.

The impulse and frequency responses of a 1000 m length of Category 3 UTP, as generated using the method above, are shown in the following figures. The sampling rate used to generate the impulse response was 26 MHz.

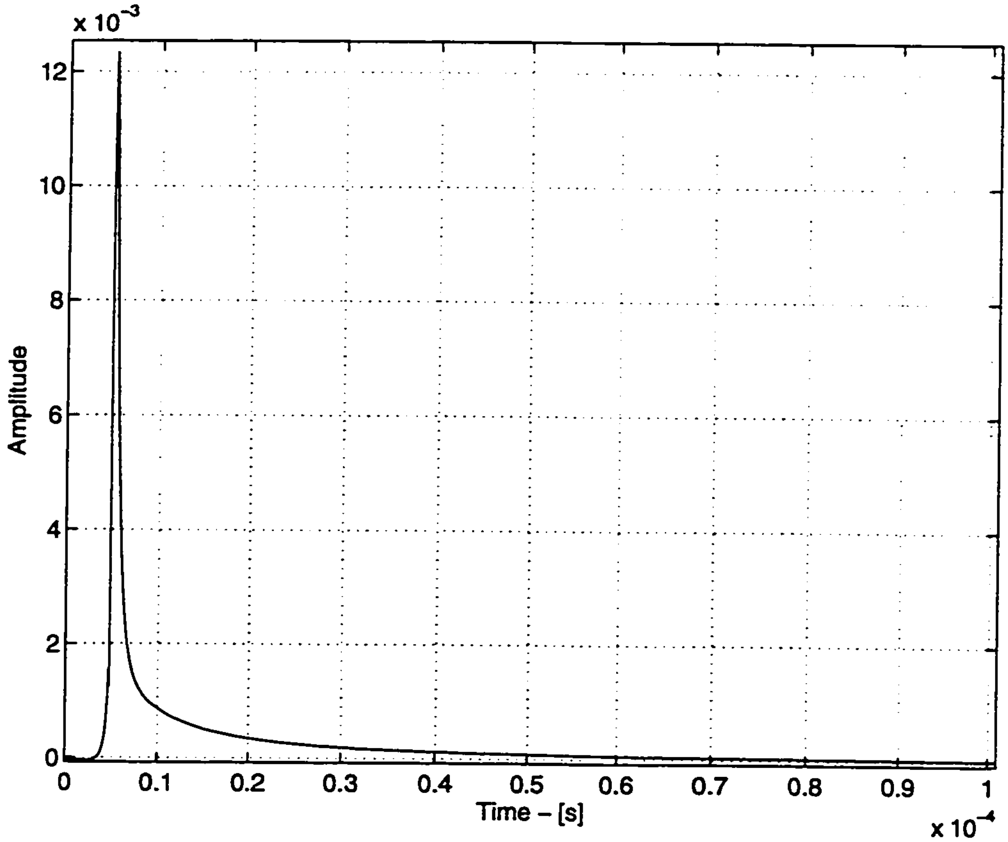

Figure 15: Sample UTP Impulse Response

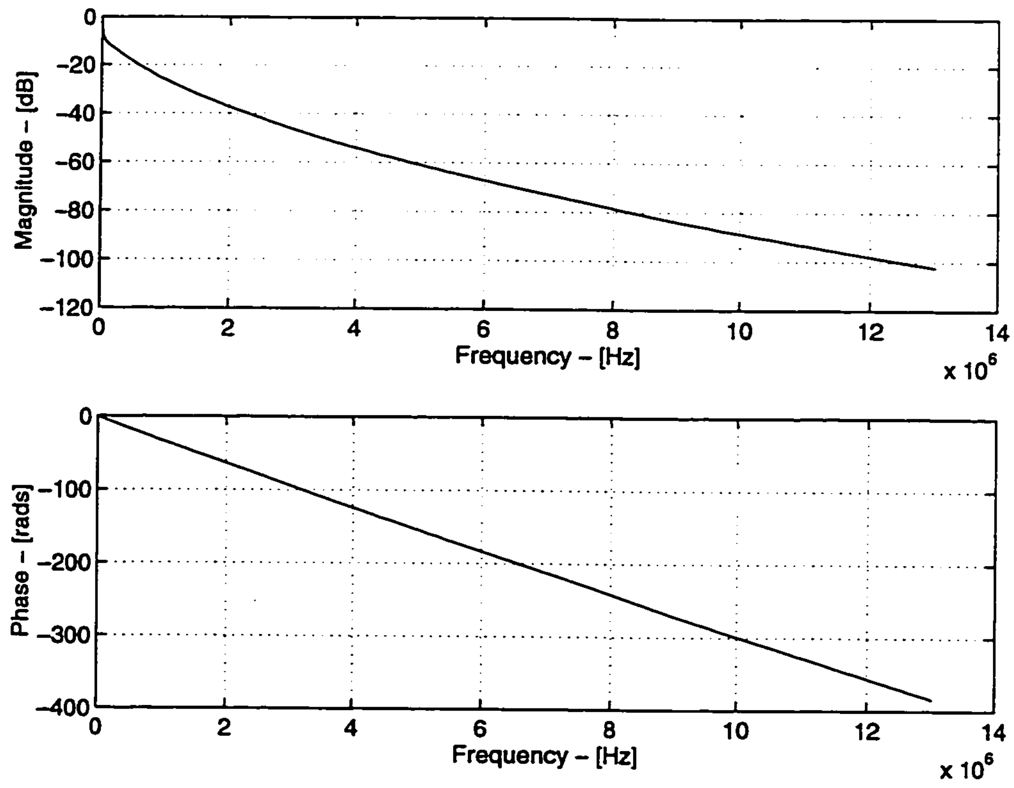

Figure 16: Sample UTP Frequency Response

The phase response in Figure 16 is actually very close to linear: there is, in fact, some non-linearity near DC which causes the exponential decay character in the impulse response. This testifies to the fact that it is important to model even very small amounts of phase distortion.

3.2 AWGN

A number of authors ([6], [7], [17], [65]) who mention additive white Gaussian noise on the UTP channel agree that a good estimate of the flat power spectral density is -140 dBm/Hz. This power spectral level is assumed, where applicable, for the analysis in this work.

3.3 FEXT

Far End CROSS-Talk or FEXT, can be an important impairment in broadband access applications. It is the result of the coupling of signals traveling in the same direction along adjacent twisted pairs in a cable.

This phenomenon is well understood and there is a consensus in the literature ([4], [8], [18], [37], [66]) about how to model it. Commonly, FEXT is modeled as a colored Gaussian process with the following power spectrum, $P_{FEXT}(f)$:

$$P_{FEXT}(f) = \left(\frac{N_d}{49}\right)^{0.6} P_{dist}(f) d_c k_F \left|H_{UTP}(f)\right|^2 f^2 \qquad \ldots(47).$$

Now to elaborate briefly on the parameters in the FEXT model:

- N_d is the number of disturber signals which contribute to the noise. In the worst case N_d is chosen to be equal to the number of twisted pairs in the cable. For the ADSL rate, it is assumed that a 50 pair cable would commonly be used along with a "to-the-neighborhood" distribution strategy and so N_d is chosen to be 49. It is assumed that VDSL service over twisted pair would entail having "curbside" units closer to the subscriber premises, and that these units would likely service fewer subscribers than in the ADSL system. Thus, for the VDSL system, N_d is chosen to be 10.

- k_F is a coupling coefficient related to the efficiency of the electromagnetic field coupling between pairs. For UTP, the value of k_F is usually chosen to be 8e-20.

- $P_{dist}(f)$ is the PSD of the disturbing signals. The model assumes that all disturbers have the same PSD. In this work, self-FEXT is assumed – meaning that the signal spectrum of the disturbers are assumed to be identical to that of the desired signal.

- d_c is the length of twisted pair over which the FEXT coupling takes place. In the worst case, d_c is equal to the loop length which implies that FEXT coupling takes place along the whole length of cable.

- $H_{UTP}(f)$ is the frequency response of the twisted pair loop.

An example self-FEXT spectrum for a 6 Mbps 16-CAP signal on 500 m of Category 3 UTP is shown in Figure 17.

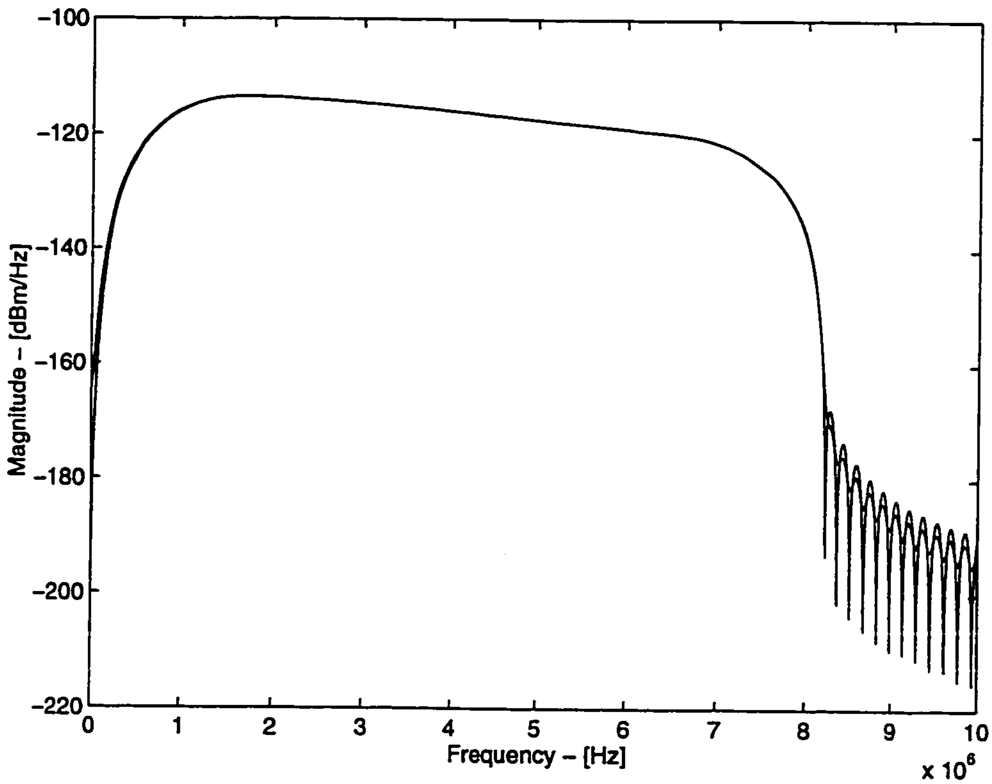

Figure 17: Example Self-FEXT Spectrum

As can be seen from the Figure 17, the self-FEXT spectrum is very similar to the spectrum of the CAP disturber signals with some amplitude distortion due to the combined effects of the channel frequency response and FEXT gain.

The Gaussian nature of the FEXT signal is best explained with reference to the central limit theorem: the sum of the random and generally unsynchronized interferers on a specific loop should tend toward a Gaussian distribution. In other words, this inherently signal dependent noise has a Gaussian character due to the fact that many signals contribute to it.

The FEXT model represented by equation (47) is a simplified model of the real process. In a real network, the loops serviced by all of the various pairs in a cable will all have different lengths in general. FEXT from dissimilar signals may also exist. This possibility is considered in the ADSL standard [4] and by Barton in [5].

Modeling the impact of FEXT on transmission over the UTP channel is difficult due to the fact that it is much smaller than the signal. For the relatively high error rates which are feasibly simulated with a Monte-Carlo simulation, the FEXT spectrum is lost in AWGN. For this reason, the effects of FEXT have been simulated in this work using a frequency-domain approach similar to link budget analysis.

3.4 Narrow-Band Interference and Emission Masking

AM-band radio broadcasts fall within the bandwidths used by ADSL and VDSL signals. Parts of the bandwidth used by VDSL signals are also used for amateur radio. These radio signals can be considered to be narrow-band interferers with respect to the xDSL signals. The AM radio band [61] and amateur radio bands [37] considered in this work are as enumerated below in Table 1.

Table 1: Radio Bands in the xDSL Bandwidth

Band	Minimum Frequency	Maximum Frequency
AM	540 kHz	1700 kHz
Amateur - 1	1.80 MHz	2.00 MHz
Amateur - 2	3.50 MHz	4.00 MHz
Amateur - 3	7.00 MHz	7.30 MHz
Amateur - 4	10.10 MHz	10.15 MHz

The power spectral level of radio frequency disturbers depends largely upon the wattage of the radio transmitters and their proximity to the xDSL plant. According to [37], the best policy in avoiding interference from amateur radio bands is to simply avoid using them. The AM radio band occupies a large bandwidth which is coincident with a desirable part of the frequency response of UTP. The notion of avoiding the AM band is therefore not very appealing.

The impact of narrow-band interference on CAP signals is essentially limited by the amount of interference power coupled into the receiver. The multicarrier modulations are fairly well-suited to dealing with the problem of narrow-band interference since the signal spectrum and information distribution can be adjusted based upon the noise and interference. The spectral isolation properties of the filter bank used (either the FFT or a CMFB) plays a big role in determining exactly how many sub-channels are affected.

An issue related to the problem of narrow-band interference is the potential need to limit emissions due to VDSL signals in the amateur radio bands. While amateur radio transmitters in the immediate vicinity of VDSL plant may cause narrow band interference, emissions from VDSL plant may swamp the weak signals from distant amateur radio sets. One strategy considered by the T1E1.4 committee (according to [37]) is to limit the power spectral density of VDSL signals in the amateur radio bands. For multicarrier modulations, this does not present a problem: one has only to reduce the power level of the sub-channels in the amateur radio band. For CAP transmission, one possibility is to intentionally notch the signal spectrum. This approach has a significant impact on the equalization requirements for CAP since a narrow notch filter in the frequency domain can have a long impulse response in the time domain.

For this work, study of the impact of the issues mentioned above will be limited in scope. In the case of CAP, the effect of applying emission masking notches to the signal will be examined. In the case of the multicarrier modulations, the spectral isolation properties of the FFT and CMFB filter banks will be discussed briefly.

3.5 NEXT

Near End CROSS-Talk or NEXT is defined to be cross talk which impairs the signal at a local receiver due to a local transmitter. NEXT is very similar to FEXT in that it too is often modeled as a coloured Gaussian process ([18], [28]). The power spectral density of NEXT, P_{NEXT}, is usually computed by the following equation.

$$P_{NEXT}(f) = k_N N_d^{0.6} P_{dist}(f) f^{1.5} \qquad \ldots(48).$$

The parameters in the NEXT model are defined as follows:

- The constant, k_N, is related to the efficiency of the NEXT coupling.
- N_d is the number of disturber signals which contribute to the cross talk.
- $P_{dist}(f)$ is the PSD of the NEXT disturbers. All disturbers are assumed to have the same PSD.

- The variable, f, denotes frequency.

In this work, NEXT is not included in the performance analysis. This simplification is in keeping with the network model of Figure 1. Only half duplex signaling is considered and so there are no near-end transmitters. In a real full-duplex system it is possible to eliminate (or at least minimize) the impact of NEXT by using non-overlapping bands for the up-stream and downstream signals. An example of this is the CAT-1 FDM link described in the ADSL standard [4]. In full-duplex systems where the upstream and downstream signals share the same band (the CAT-2 link described in the ADSL standard, for example), NEXT can be a major impairment.

3.6 Impulse Noise

Several authors agree that impulse noise is one of the dominant impairments in twisted pair plant [7], [26], [57], [67]. As indicated by Mélinand in [44], the accurate modeling the phenomenon for the xDSL scenario, however, is an open problem.

We can think of impulse noise on UTP as an ensemble of randomly arriving waveforms with random amplitude and duration along with a non-uniform mean spectral shape. These concepts are illustrated in Figure 18.

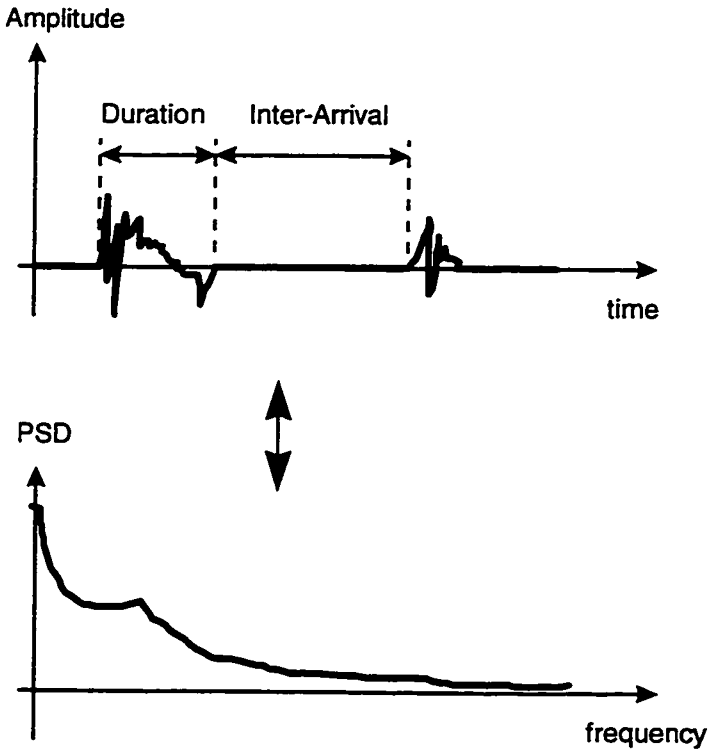

Figure 18: Impulse Noise in the Time and Frequency Domains

Historically, the general approach in the analysis of impulse noise has been to use as simple a model as possible given the channel and modulation under consideration. An early example of an impulse noise model is Middleton's Class A model, originally conceived (and successfully used), for the analysis of radio channel communications. In this model, impulse noise is "lumped in" with other additive noise sources to form a generalized amplitude distribution for noise. This is possibly the simplest model to incorporate in performance calculations: one has only to integrate over the aggregate distribution.

A more complicated and more recent model is the time-domain, Poisson-arriving δ-functions model which is equivalent to a Bernoulli-Gaussian model in discrete time [21]. This model incorporates both an inter-arrival time distribution and an amplitude (or energy) distribution. Analytical performance analysis using this model is still tractable using Fourier-Bessel series expansion as demonstrated in references [21] and [36]. Modeling impulse noise on UTP plant as a train of Poisson-arriving delta functions is surely better than not modeling it at all but, currently, we can not say much more than that with a high level of confidence. The δ-functions have zero duration and so, the model does not include any notion of the duration of impulse noise events. On UTP plant, impulse noise events can be on the order of several hundreds of micro-seconds long. At xDSL data rates, this duration corresponds to many CAP symbols and can even be comparable to the duration of a multicarrier symbol[25].

One effort at incorporating an element of impulse event duration in performance analysis is documented in [7]. In this paper, Barton applies a model which uses Poisson arrivals and a variety of amplitude distributions along with a characteristic impulse to simplify the mathematics. As such, the model does not take into account the variety of wave-forms which impulse noise exhibits and, in effect, it uses fixed impulse duration. On the positive side, the mean energy spectral density is incorporated – this fact was used to generate a number of results in [7].

It should be clear that all of the models mentioned so far rely heavily upon simplifying assumptions. In the literature, we can find analyses where the Poisson arriving δ-functions model and the characteristic impulse model have been applied – yet there is no authoritative reference against which we can validate these interesting results. This indicates that for xDSL, it is worthwhile to use a detailed time domain model for impulse noise based upon its amplitude, duration and inter-arrival statistics.

Henkel et al. of Deutsch Telekom propose exactly such a model for the ADSL environment in [25], [26] and [27]. Based upon a data base acquired via an extensive measurement campaign at sites in Germany, they have characterized the various statistics of impulse noise as well as the mean PSD and phase within the ADSL bandwidth. They also propose a generator structure for use in simulation. What follows is a brief summary of their statistical model. Interested readers are referred to the references mentioned above and [44] for details about the generator implementation.

The voltage was found to follow a double-sided exponential distribution of form:

$$f_{Voltage}(u) = \frac{e^{-|u/u_v|^{1/5}}}{10\Gamma(5)u_v} \qquad \ldots(49)$$

where u_v is a parameter which effects the spread of the distribution.

The probability density function for the impulse event duration suggested by Henkel et al is a double (or bi-modal) log-normal distribution. This form is represented by the following equation:

$$f_{Dur.}(t) = q_d \frac{1}{\sqrt{2\pi}\, s_{d1} t} e^{-\left[\ln^2(t/t_{d1})\right]/\left(2s_{d1}^2\right)} + \left(1 - q_d\right) \frac{1}{\sqrt{2\pi}\, s_{d2} t} e^{-\left[\ln^2(t/t_{d2})\right]/\left(2s_{d2}^2\right)}$$

$$\ldots(50)$$

where q_d is a constant which sets relative weight of the two modes; t_{d1} and $_{td2}$ are medians of the two modal distributions; s_{d1} and s_{d2} are parameters which effect the spread of the two component distributions (analogous to standard deviation in a regular normal distribution).

The inter-arrival times were observed to follow a generalized exponential or Fano distribution:

$$f_{Inter.}(x) = \frac{10^{\alpha_{I1}}}{\ln(10)} x^{(\alpha_{I4}-1)} 10^{\frac{\alpha_{I4}}{\ln(\alpha_{I2})}\alpha_{I2}^{(\log 10(x)-\alpha_{I3})}} \qquad \ldots(51)$$

where α_{I1} is a normalization parameter; and α_{I2}, α_{I3} and α_{I4} are parameters which effect the shape of the distribution. This is probably the most interesting distribution because it is not the simple exponential distribution which is associated with Poisson arrivals (this notion is corroborated in [67]). The measured data showed that, while during relatively short periods of time the inter-arrival time was approximately exponentially distributed, the mean event frequency $(1/\lambda_E)$ varied significantly over the course of any 24 hour period. This property was related to the amount of traffic on the network: in a banking district, for example, very little happens at night. The variation in arrival rates is accounted for by averaging a standard exponential distribution over the distribution of λ_E (which was assumed to be uniform between 0 and some positive value). The result of this averaging step is the distribution of equation(51).

The value of a generator model based upon the statistics discussed above depends heavily upon the data used to characterize the parameters. To date, there are two fairly good characterization studies for the ADSL bandwidth. These are the Deutsch Telekom study mentioned above and a study undertaken by Nynex in 1986 which is described in [57]. As well, there are a number of references for ISDN as indicated in [67]. At the time of writing, there is still no publication of data which considers the VDSL bandwidth.

Chapter 4

Link Margin Analysis

The link margin in a communications system is the ratio, expressed in dB, of the actual signal-to-noise ratio at the decision device, $SNR_{dec.}$, to the signal-to-noise ratio required to achieve the poorest (highest) acceptable error rate performance, $SNR_{min.}$. In equation form, the link margin, m, can be expressed as:

$$m = 10 * \log_{10}\left(\frac{SNR_{dec.}}{SNR_{min.}}\right) \qquad \text{...(52).}$$

The link margin is easily interpreted. If the value is negative for a specific value of $SNR_{dec.}$, the system will have a higher error rate than the maximum acceptable value. A positive link margin implies that the system can do better than the poorest acceptable error rate. Examining link margins is a good step towards answering the basic question: "Is it possible to transmit the desired data rate on the channel in the presence of the known impairments?"

One can think of a number of ways to estimate link margins to various degrees of accuracy. For example, one could perform simulations and characterize the error rate performance curve. This can be very accurate but very time consuming. It is desirable to estimate link margins before investing the time in a detailed simulation. One relatively simple and quick way to estimate link margins is to do the following: 1) determine $SNR_{min.}$ from an assumed form for the error probability as a function of signal to noise ratio; 2) compute $SNR_{dec.}$ based upon what is known about the power spectra of the signal and noise/interference; and 3) compute the link margin using the results from the previous steps. This method was adopted for the link margin analysis in this work.

4.1 CAP Link Margins

The symbol error probability, $P_{e\,CAP}$, as a function of $SNR_{dec.}$ for CAP signaling is approximated as:

$$P_{e\,CAP} \approx 4\left(\frac{\sqrt{L_{CAP}}-1}{\sqrt{L_{CAP}}}\right) Q\left(\sqrt{\frac{3}{(L_{CAP}-1)} SNR_{dec.}}\right) \qquad \ldots(53)$$

where L_{CAP} is the number of symbols in the CAP constellation.

This is the sum of the symbol error probabilities for the two quadrature PAM signals which make up the CAP signal. Assuming that the constellation is Gray coded, we can approximate the bit error probability, commonly referred to as bit error rate or BER as:

$$BER_{CAP} = \frac{P_{e\,CAP}}{\log_2(L_{CAP})} \qquad \ldots(54).$$

From the above equation, the required $SNR_{min.}$, at the decision device for a value of BER_{CAP} is given by:

$$SNR_{min.} = \frac{L_{CAP}-1}{3}\left[Q^{-1}\left(\log_2(M) BER_{CAP} \frac{\sqrt{L_{CAP}}}{4\left(\sqrt{L_{CAP}}-1\right)}\right)\right]^2$$

...(55).

For BER_{CAP} = 1e-7 using 16-CAP, the SNR requirement is approximately 21.2 dB.

The SNR at the receiver input is not equivalent to the SNR at the decision device due to the noise enhancement effects of the equalizer. After the analysis in [49] and [65], the SNR at the decision device can be approximated by evaluation of the following equation:

$$SNR_{dec.} = \exp\left[T_{sym} \int_{f \in B} \ln\left(\frac{|H_c(f)|^2 S_{CAP}(f)}{\Phi_n(f)}\right) df\right] \qquad \ldots(56)$$

where B is the set of frequencies within the 3 dB bandwidth of the signal; $H_C(f)$denotes the channel frequency response; $\Phi_n(f)$ is the noise power spectral density and $S_{CAP}(f)$ is the power spectrum of the CAP signal for the specific transmit power level under consideration. Since CAP is a linear modulation, the PSD has the same shape as the frequency response of the in-phase and quadrature pulses. FEXT and AWGN were assumed to both be zero-mean, uncorrelated, Gaussian processes. This allows us to formulate the aggregate power spectrum as the sum of the FEXT and the AWGN power spectral densities as described in Chapter 3.

4.2 DMT Link budgets

Link margins for FFT-DMT were computed using the bit allocation and spectral optimization procedures described in Chapter 2. These procedures find the optimum bit allocation and spectrum shape based upon the channel response, noise sources and the target value of $\gamma = \left(d_{RX\,k} / 2\sigma_k\right)^2$, a quantity proportional to SNR. Due to the way in which the optimization of the bit allocation and spectrum is formulated, it is convenient to compute performance margins relative to a symbol error rate target but not relative to a BER target. For simplicity in computing margins for DMT, in this work we will assume that the symbol and bit error probabilities are equivalent. The DMT margins will be slightly pessimistic due to this simplification since BER is smaller than SER when we assume Gray coding. Assuming, for example, that all sub-channels carry 12 bits and that each symbol error amounts to only one bit error, the SER would be greater than the BER by a factor of 12. This factor of 12 difference corresponds to an SNR error of less than 1 dB at BER = 1e-7. The degradation due to equalization is not modeled because it should be minor due to the fact that the sub-channels have relatively narrow bandwidth.

In the case where AWGN and was the only noise impairment, estimating the performance margin was accomplished by computing the transmit power required for zero performance (or link) margin, $P_{m=0}$, and then comparing this quantity with the desired transmit power, P_{TX}, using the following equation:

$$m = 10 * \log_{10}\left(\frac{P_{TX}}{P_{m=0}}\right) \qquad \ldots(57).$$

In the cases where self-FEXT was included, estimating the link margin was made more complicated by the fact that the FEXT spectrum is a function of the signal spectrum. In effect, both the DMT signal spectrum and the self-FEXT spectrum have to be designed by the bit allocation/spectrum optimization. Computing the performance margin in the presence of self-FEXT was accomplished by using a simple search algorithm to find the maximum performance margin for which the required bit payload could be achieved without exceeding the transmit power.

4.3 Link Margin Results

The following sections present the results of link margin computations at the ADSL and VDSL data rates.

4.3.1 ADSL Link Margins

Link margins for the representative ADSL data rate of 6 Mbps were computed considering the effects of AWGN and self-FEXT (49 disturbers). A target BER of 1e-7 was assumed.

Link margins for CAP transmission were computed for the different parameters listed below in Table 2.

Table 2: Parameters for CAP ADSL Link Margins

Parameter	Value(s)
Constellation Size (M)	4, 16, 64
Transmit Power	10 mW
Loop Length	100 - 2500 m
Pulse Roll-off	$\alpha_{RC} = 0.25$
Low Frequency Band Edge	50 kHz

The in-band transmit and receive shaping filters used by the CAP system are assumed to be based upon a baseband square root raised cosine characteristic. Thus, the undistorted end-to-end pulse shape is raised cosine. The pulse roll-off parameter specifies the excess bandwidth of the signal: in this case, $\alpha_{RC} = 0.25$, and the system uses 25 % excess bandwidth.

The center frequencies for the various CAP constellations were computed using the following relationship:

$$f_c = \frac{R}{\log_2(L_{CAP})} \times \frac{1+\alpha_{RC}}{2} + 50kHz \qquad \ldots(58)$$

where R is the bit rate; L_{CAP} is the constellation size and α_{RC} is the roll-off factor of the raised cosine pulses. The center frequencies computed using (58) put the minimum frequency of the CAP signals at 50 kHz. The low frequency band edge was chosen to provide a generous guard band between the ADSL signal and the part of the UTP spectrum used for voice-band services (e.g. POTS) which are assumed to coexist with ADSL [6].

The sampling rates in the case of CAP transmission were computed assuming that the scheme used 4 samples per symbol period. We can therefore express the sampling frequency as

$$f_s = \frac{4R}{\log_2\left(L_{CAP}\right)} \qquad \ldots(59)$$

where R and L_{CAP} are defined as above.

For FFT-DMT, link margins were computed assuming the parameters inTable 3.

Table 3: Parameters for FFT-DMT ADSL Link Margins

Parameter	Value(s)
Transform Size	1024 points
Cyclic Prefix Length	0
Transmit Power (maximum)	10 mW
Minimum Frequency	50 kHz
Maximum Frequency	1 MHz
Sampling Frequency	2 MHz
Loop Length	100 - 2500 m

The frequency parameters in Table 3 define the available bandwidth – this bandwidth would only be used if all of the available tones were allocated bits. The actual bandwidth used by the DMT signal depended on the results of the bit allocation procedure which, in general, does not use all of the available tones. The available bandwidth for ADSL-DMT was chosen to be approximately equal to the minimum bandwidth required for 64-CAP (bandwidth efficiency ~ 6 bps/Hz) as in the ADSL Standard [4].

The link margins for CMFB-DMT were not computed because they should be equivalent to the link margins for FFT-DMT under the constraint that the cyclic prefix is not used for FFT-DMT. This is due to the fact that the symbol period for FFT-DMT is twice as long as the symbol period for CMFB-DMT assuming the same number of FDM sub-channels and equal sampling rates. The bit payload of an FFT-DMT symbol is twice the bit payload of the CMFB-DMT symbol under these constraints and the SNR's on each sub-channel should be equivalent for both schemes. Neglecting the factor of two difference in the symbol error probability equations for PAM and QAM, CMFB-DMT and FFT-DMT should have the same link margins under the conditions mentioned above.

4.3.1.1 Margins with AWGN Only

The following chart shows the link margins computed for the 6 Mbps ADSL data rate assuming AWGN is the only impairment.

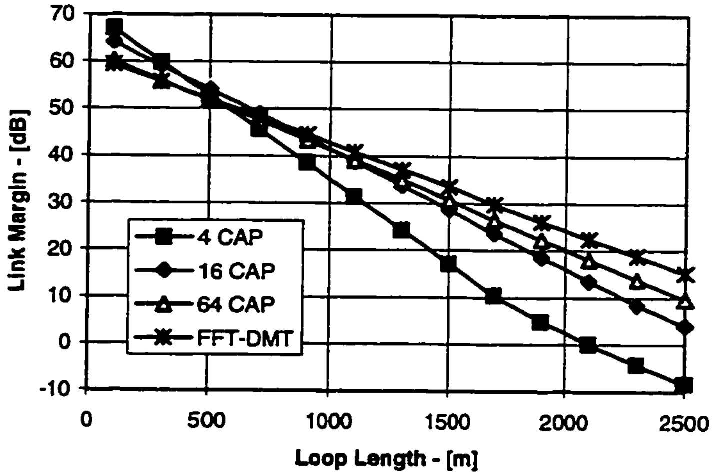

Figure 19: ADSL Link Margins vs. Loop Length - AWGN Only

Figure 19 shows that, for very short loops (< 500 m), the modulations which have the lowest bandwidth efficiency tend to do better in the presence of AWGN because of their lower SNR requirement. Note also that the FFT-DMT margins are nearly equal to the 64-CAP margins on short loops. This is because the channel attenuation response is fairly mild and the FFT-DMT signal has close to uniform bit allocation across the band. For loop lengths beyond 500 m, we see that the modulations with higher bandwidth efficiency have higher margins. This is due to the smaller signal bandwidth which makes them less susceptible to the channel attenuation response. As the channel response becomes more frequency selective, the spectral efficiency of the DMT signal increases because the bit allocation routine puts more bits on the low frequency channels which experience less attenuation. For this reason, as the loop length increases, the advantage of the DMT scheme increases.

4.3.1.2 Margins with self-FEXT

Link margins for the 6 Mbps data rate in the presence of AWGN and 49 self-FEXT disturbers are shown in Figure 20.

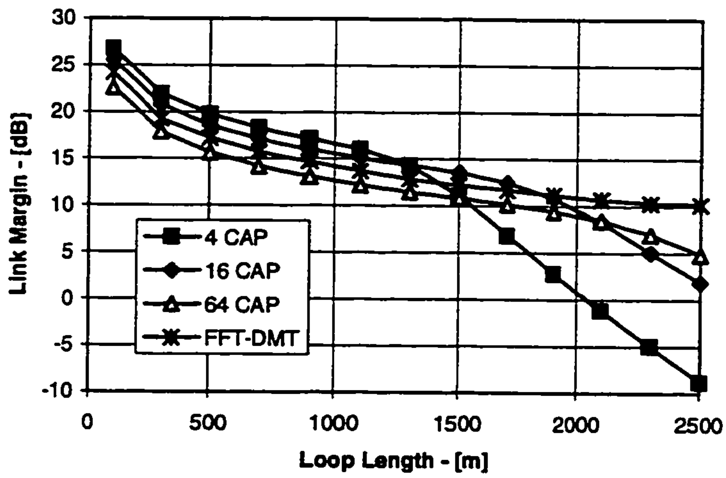

Figure 20: ADSL Link Margins vs. Loop Length
- AWGN + 49 FEXT

The link margin results for CAP are very similar to the results in [37] and [65]. As observed in [65], we see that, for shorter loops, the CAP schemes are FEXT limited. When the loop length becomes longer and the channel attenuation becomes more significant, the FEXT PSD becomes buried in the AWGN floor. As a result, the CAP link margin versus loop length curves tend towards the curves computed considering AWGN only for long loop lengths. This phenomenon is most visible in the cases of 4-CAP and 16-CAP where we observe distinct "knees" in the margin curves at approximately 1200 m and 1800 m respectively. The knee in the margin curve for 64-CAP is just beginning to occur at 2500 m, the maximum loop length considered.

As was observed in the previous section for AWGN only, the modulations with smaller bandwidth efficiency have better margins for short loop lengths. This can be explained by their smaller in-band power spectral level (which means a smaller FEXT PSD) as well as their smaller SNR requirement. For longer loops, the modulations with higher bandwidth efficiency do better, once again, because they experience less in-band attenuation.

On short loops, the margins for FFT-DMT are only slightly better than those for 64-CAP. As the loop length increases and the AWGN limit takes over, the FFT-DMT scheme shows an advantage over the three CAP schemes due to its optimized spectrum and bit allocation.

4.3.2 VDSL Link Margins

For the representative VDSL data rate of 26 Mbps, link margins were computed considering the effects of AWGN and self-FEXT (10 disturbers). As was the case for the ADSL link margins, a target BER of 1e-7 was assumed.

Link margins for CAP transmission were computed for the different parameters listed below in Table 4.

Table 4: Parameters for CAP VDSL Link Margins

Parameter	Value(s)
Constellation Size (M)	4, 16, 64
Transmit Power	10 mW
Loop Length	100 - 1100 m
Pulse roll-off	$\alpha_{RC} = 0.25$
Low Frequency Band Edge	50 kHz

Once again, it is assumed that the CAP system uses in-band pulses which yield an end-to-end pulse which has the raised cosine characteristic. The pulse roll-off is related to the excess bandwidth of the signal.

The center frequencies and sampling rates for the various CAP modulations were computed using equations (58) and (59).

Link margins for CAP at 26 Mbps were also computed considering the effect of emission making in the amateur radio bands described in Section 3.4. The depth of the spectral notches in the amateur radio bands was 20 dB. The spectrum notching was implemented by incorporating a long FIR filter which provided nearly ideal notches in the end-to-end response.

Margins for FFT-DMT were computed for the parameters listed below inFigure 5.

Table 5: Parameters for VDSL/FFT-DMT Link Margins

Parameter	Value(s)
Transform Size	1024 points
Cyclic Prefix Length	0
Transmit Power (maximum)	10 mW
Minimum Frequency	50 kHz
Maximum Frequency	4.33 MHz
Sampling Frequency	8.67 MHz
Loop Length	100 - 1100 m

As was the case for the ADSL analysis, the available bandwidth for FFT-DMT was chosen to be equal to the minimum bandwidth for 64-CAP.

4.3.2.1 Margins with AWGN Only

Link margin results for the VDSL data rate considering AWGN only are shown in Figure 21.

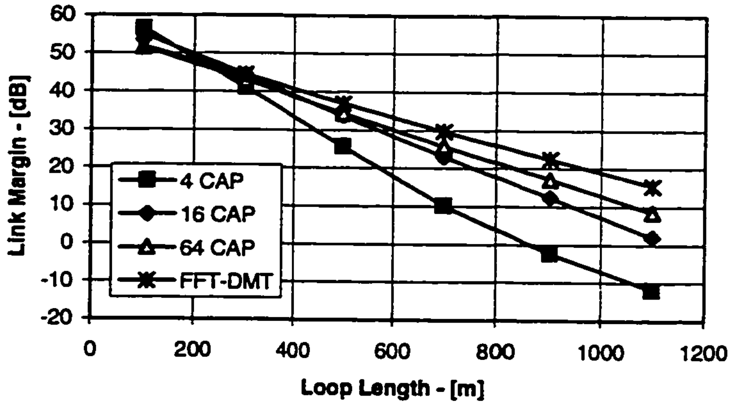

Figure 21: VDSL Link Margins vs. Loop Length - AWGN Only

The results for VDSL transmission in the presence of AWGN are very similar to those observed at the ADSL data rate. For short loop lengths, the modulations with smaller SNR requirements are better. As the loop length increases beyond about 200 m and the channel frequency response becomes steeper, the more bandwidth efficient modulations exhibit an SNR advantage.

4.3.2.2 Margins with self-FEXT

VDSL link margins computed considering the effects of AWGN and 10 self-FEXT disturbers are shown in Figure 22.

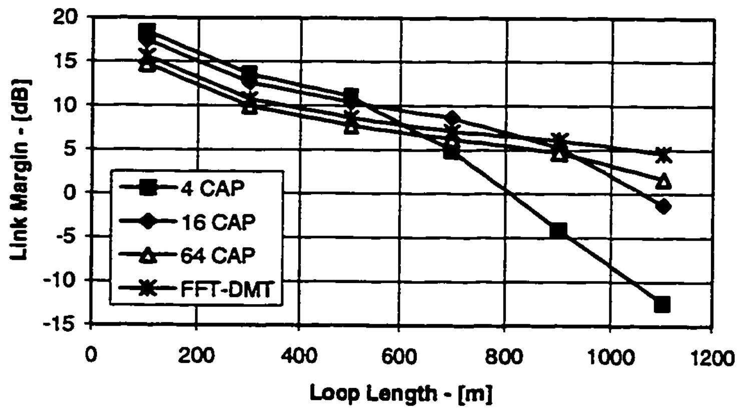

Figure 22: VDSL Link Margins vs. Loop Length
- AWGN + 10 FEXT

Again, the results are similar to those observed at the ADSL data rate. For short loops, all of the modulations exhibit FEXT limited performance. As loop length increases, we observe that the CAP link margin curves hit their respective, asymptotic AWGN limits. This coincides with the FEXT spectra becoming buried in the AWGN floor. For loops longer than about 850 m, FFT-DMT shows an advantage over the CAP modulations.

4.3.2.3 CAP Margins with Emission Masking

Figure 23 shows link margins for the CAP modulations computed considering AWGN and emission masking in the amateur radio bands.

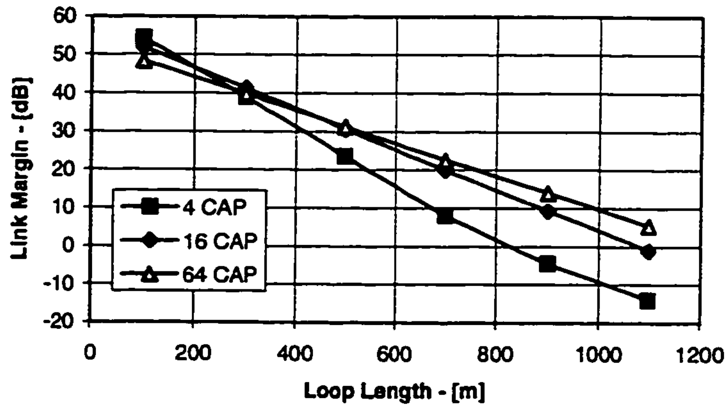

Figure 23: VDSL Link margins vs. Loop Length
- AWGN + Emission Masking

The link margins plotted above are very similar to those in Figure 21 which were computed considering AWGN only. There is a difference with respect to the margins for AWGN only due to the fraction of power lost by the notching and noise enhancement. For 4-CAP there is approximately 2 dB degradation due to emission masking; for 16-CAP the degradation is approximately 3 dB; and for 64-CAP emission masking causes a decrease of nearly 3.5 dB in the link margins. It is important to point out that these results are somewhat optimistic in that we have assumed an infinitely long equalizer and that it would converge perfectly. They do, however, indicate that the penalty due to enhancement of AWGN is moderate.

4.4 Estimating Reach

Link margin results like the ones presented in the previous section can be used to estimate the "reach" of a given communications scheme on the medium under consideration. The reach in the case of ADSL and VDSL transmission over UTP is defined to be the maximum loop length over which the error rate performance is better than some specified level. This error rate requirement is equivalent to requiring that the link margin be beyond a certain minimum value.

Assuming the performance margin standard suggested in [4] – namely a +6 dB margin relative to the SNR required for a BER of 1e-7, we can estimate the reach of the various modulations from Figures Figure 19 to Figure. These results are shown in Table 6 and Table 7.

Table 6: Reach of CAP and FFT-DMT for ADSL Data Rate

Modulation	Reach - AWGN only	Reach - AWGN + 49 FEXT
4-CAP	1800 m	1700 m
16-CAP	2400 m	2200 m
64-CAP	> 2500 m	2400 m
FFT-DMT	> 2500 m	> 2500 m

Table 7: Reach of CAP and FFT-DMT for VDSL Data Rate

Modulation	Reach - AWGN only	Reach - AWGN + 10 FEXT
4-CAP	700 m	650 m
16-CAP	1050 m	900 m
64-CAP	> 1100 m	750 m
FFT-DMT	> 1100 m	900 m

Based upon the results tabulated above and the trends in Figure 19 to Figure 23, we can make some observations. DMT offers the most advantage when the channel has significant amplitude distortion and performance is AWGN limited. Clearly, DMT should provide the longest reach for ADSL compared to the other modulation schemes considered given the performance requirement. Among the different CAP modulations considered, 64-CAP should provide the best reach for the ADSL data rate. Both DMT and 16-CAP should provide equivalent reach for VDSL data rate under the simulated conditions.

4.5 Choice of CAP Constellation

The margin and reach results discussed in the preceding sections indicate that 16-CAP and 64-CAP can provide similar performance on UTP. Due to its smaller SNR requirement, 16-CAP does exhibit better margins than 64-CAP on a greater proportion of the loop lengths considered.

It is important to note that the link margin analysis only considered a subset of the impairments which exist on the UTP channel: NEXT and impulse noise were not included in the analysis. References [6], [8], and [17] suggest that 16-CAP is the optimal constellation for ADSL considering FEXT and NEXT from a variety of sources. The fact that 16-CAP was chosen for a 51.84 Mbps transmission over UTP in the ATM LAN standard as well as the analysis in [28] corroborate the idea that 16-CAP is a good choice for the lower VDSL rate considered here. Based upon [19], 16-CAP transceivers should also be simpler to implement than 64-CAP transceivers due to the fact that 16-CAP is less sensitive to timing phase error.

For the reasons mentioned above and to reduce the scope of the work to follow, 16-CAP will be the only CAP modulation considered from here on.

Chapter 5

Simulating the Error Rate Performance

This chapter is a discussion of time-domain simulation methods used to determine the error rate performance of 16-CAP, CMFB-DMT and FFT-DMT. The simulations discussed in this chapter were employed in simulating the performance of the three modulations in the presence of AWGN. In the case of 16-CAP, the Monte Carlo simulation discussed in this chapter was also used to obtain performance curves in the presence of AWGN and emission masking.

The effects of FEXT on the performance of the modulations considered in this work were studied using methods based upon frequency domain link margin analysis. Since link margin analysis was discussed in some detail in the previous chapter, these methods are described briefly along with the relevant results in Chapter 6.

5.1 CAP

The performance of CAP in the presence of AWGN, with and without emission masking, was obtained using a simple Monte-Carlo simulation.

5.1.1 Time Domain Monte-Carlo Simulation

The time-domain Monte-Carlo simulation of 16-CAP performance was based on the system block diagram of Figure 2. There were some minor differences, however, which are reflected in Figure 24.

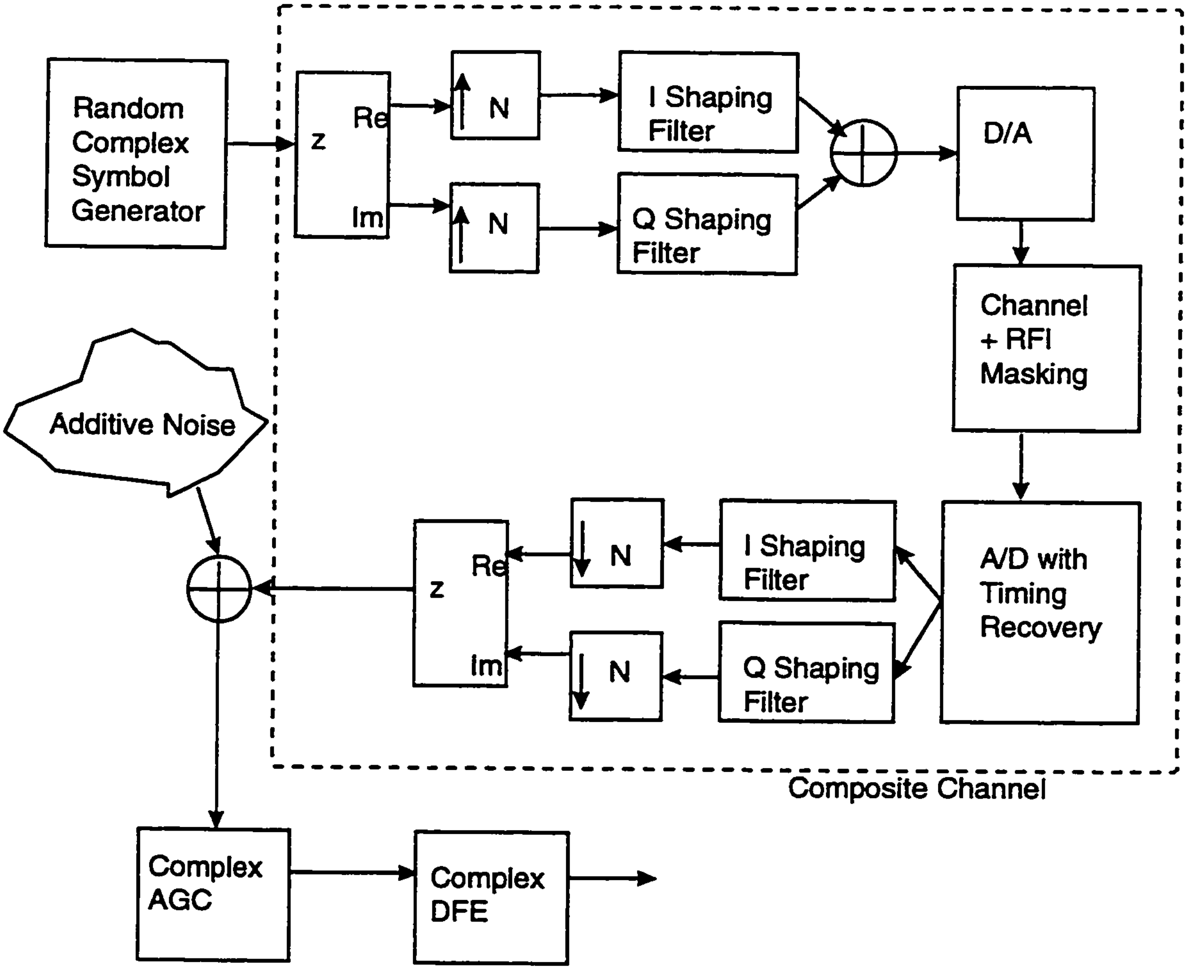

Figure 24: CAP Simulation Block Diagram

In the simulation, the end-to-end channel – shown in a box in Figure 24 – was modeled using symbol-spaced impulse responses. This implies that linearity was assumed and that the D/A and A/D were assumed to have infinite precision. One visible difference from Figure 2 is that the AWGN was referred to the output of the end-to-end channel. Another is the addition of a complex AGC before the DFE. The purpose of this AGC was to correct the amplitude and phase of the cursor tap of the composite channel response – thus facilitating the task of converging the equalizer (and selecting the LMS adaptation step size).

The flow-chart shown in Figure 25 depicts the sequence of events performed in the simulation for a single BER point.

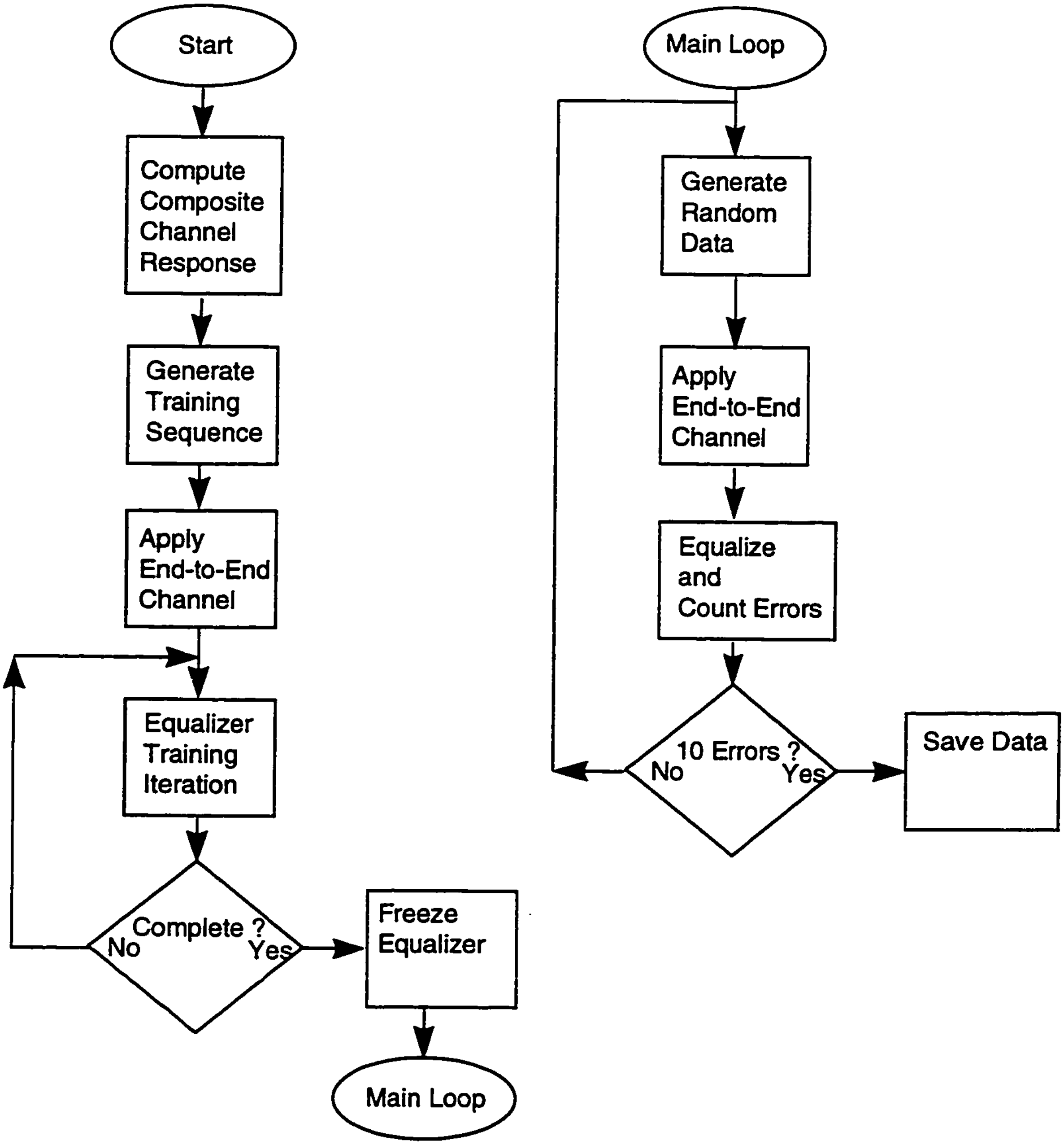

Figure 25: CAP Monte-Carlo Simulation Flow Chart

The equalizer was trained for each SNR since the LMS adapted coefficients are generally different for each SNR. The stopping condition for the main loop iterations was chosen to be a count of at least 10 errors. This was determined to be sufficient to achieve repeatable performance curves. It is worth noting, however, that the reliability of the estimate of the

BER improves as the error count used for the stopping condition is increased. Commonly, a count of 100 errors is employed as the stopping condition in similar Monte-Carlo simulations.

5.1.1.1 Optimum Timing Recovery

Two symbol-spaced impulse responses were used to represent the composite channel: these are the complex outputs at the receiver due to the transmission of the in-phase and quadrature-phase pulses. The composite channel responses were computed taking into account the transmit and receive pulses; the impulse response of the medium; the RFI masking impulse response if it was present; and down-sampling to the symbol rate at the receiver using optimum timing phase.

The received waveform, $\tilde{v}_I$, due to the transmission of the in-phase pulse and the received waveform, $\tilde{v}_Q$, due to the transmission of the quadrature-phase pulse can be expressed as follows:

$$\begin{aligned} \tilde{v}_I &= \tilde{g}_I * \tilde{h}_{UTP} * \tilde{h}_{mask} * \left(\tilde{h}_I + j\tilde{h}_Q\right) \\ \tilde{v}_Q &= \tilde{g}_Q * \tilde{h}_{UTP} * \tilde{h}_{mask} * \left(\tilde{h}_I + j\tilde{h}_Q\right) \end{aligned} \qquad \ldots(60)$$

where g_I and g_Q are the transmit in-phase and quadrature-phase pulses respectively; h_I and h_Q are the receive filters; h_{UTP} is the discrete model of the UTP impulse response and h_{mask} is the masking impulse response (optional). The tildes in the equation above are there to indicate that the equation is referring to a continuous time equivalent to what is normally a discrete function in this work. This is to reflect the fact that an analogue signal passes through the channel and that there is a continuum of possible instants at which the receiver can sample the incoming signal.

The timing phase, ϕ_{opt}, was chosen to maximize the ratio of the energy in the complex cursor tap to the energy in the remainder of the sequence. This figure of merit can be expressed as follows:

$$F = \frac{\left|v_{I0}\right|^2}{\sum_{n,n\neq 0}\left|v_{In}\right|^2} \qquad \ldots(61)$$

where

$$v_{In} = \tilde{v}_I\left(nT_{sym} + \phi_{opt}\right) \qquad \ldots(62)$$

are samples of the of the continuous wave-form, $\tilde{v}_I$, taken at intervals of one symbol period T_{sym}. By convention, the cursor tap has index 0. Optimum sampling which maximizes the figure of merit in (61), can be termed optimum sampling in the mean-squared sense. This is analogous to optimum IF timing recovery in digital radio as discussed in [22].

5.1.1.2 Determining Equalization Requirements.

The method described in [23] was used to determine the number of DFE taps required for the various CAP simulations. This method involves applying a magnitude threshold to the symbol-spaced samples of the end-to-end response described by (62). The feed-forward filter length, L, and the feed-back filter length, K, are chosen such that

$$\left|\frac{v_{In}}{v_{I0}}\right| < Threshold, n \in [-L, K] \qquad \ldots(63)$$

where v_{In} is the complex ISI sequence with index 0 corresponding to the cursor. The magnitude threshold is similar to a peak distortion threshold on each rail.

In this work, the threshold was chosen to be small (usually 0.001) in order to ensure that the span of the DFE essentially covered the entire duration of the dispersed pulse. The number of taps used was probably slightly larger than required at the error rates simulated.

5.2 Multicarrier Modulations

Monte-Carlo simulation of the performance multicarrier modulations in the presence of AWGN was not practical due to the large number of cross-talk terms and the relatively high order constellations used. Assume, for example, that one wished to simulate the performance of one sub-channel in a system with 6 sub-channels, each of which carries a 4 bit constellation. Let's also assume that the span of ISI and ICI is a uniform 5 symbols and all of the five other sub-channels interfere with the one being observed. The total number of bit values which affect the decision variable on the sub-channel under observation is 120. Thus, the total number of unique data combinations is 2^{120}. A basic Monte-Carlo simulation would have to go through all of these combinations – at least once – in order to accurately model the interference amplitude distribution. It would take excessive amounts of time to obtain repeatable BER curves for moderate SNR's.

Viable alternatives to Monte-Carlo simulation use either Gauss quadrature rules (as in [30], [32]) or the maximum entropy method (described in [31]) to estimate the aggregate density of ISI and ICI based upon the moments of these random variables. These approaches can be termed Method of Moments (MOM) based simulation methods. In this work, the simulations of multicarrier modulation performance in the presence of AWGN used the Gauss quadrature rules because this method is faster than the maximum entropy method which includes an optimization step to find Lagrange multipliers.

5.2.1 Simulation of CMFB-DMT in the Presence of AWGN

The simulation of the aggregate BER performance of CMFB-DMT in the presence of AWGN was performed by analyzing the symbol error rate (SER) on each sub-channel using the MOM-based method mentioned above and then combining the results. The simulations for each sub-channel were based upon the block diagram shown in Figure 26. This block diagram is a re-arrangement of Figure 5 from Chapter 2. Sequences of PAM symbols are assumed to be transmitted on all of the sub-channels. These symbols have odd-integer valued levels and are drawn from the constellations chosen by the bit allocation routine. The symbolic sequences are up-sampled and the CMFB synthesis filters, g_m, are applied. The transmit filter amplitudes are scaled to achieve the optimized spectrum shape (which is designed to achieve a target value of $\gamma = d_{RX\,k}/2\sigma_k$ on all sub-channels at the receiver). The resultant sequences from the transmit filter outputs are summed as they would be by the synthesis transform. The aggregate transmit sequence is sent through the D/A, the channel, A/D and linear equalizer. Next, the receive filter for the k^{th} sub-channel, h_k, is applied and the output is down-sampled to the symbol rate. Finally, additive noise referred to the output of the receive filter is introduced, the ISI and ICI sequences are modified by the ideal post-detection combiner and the resultant decision variable is sliced.

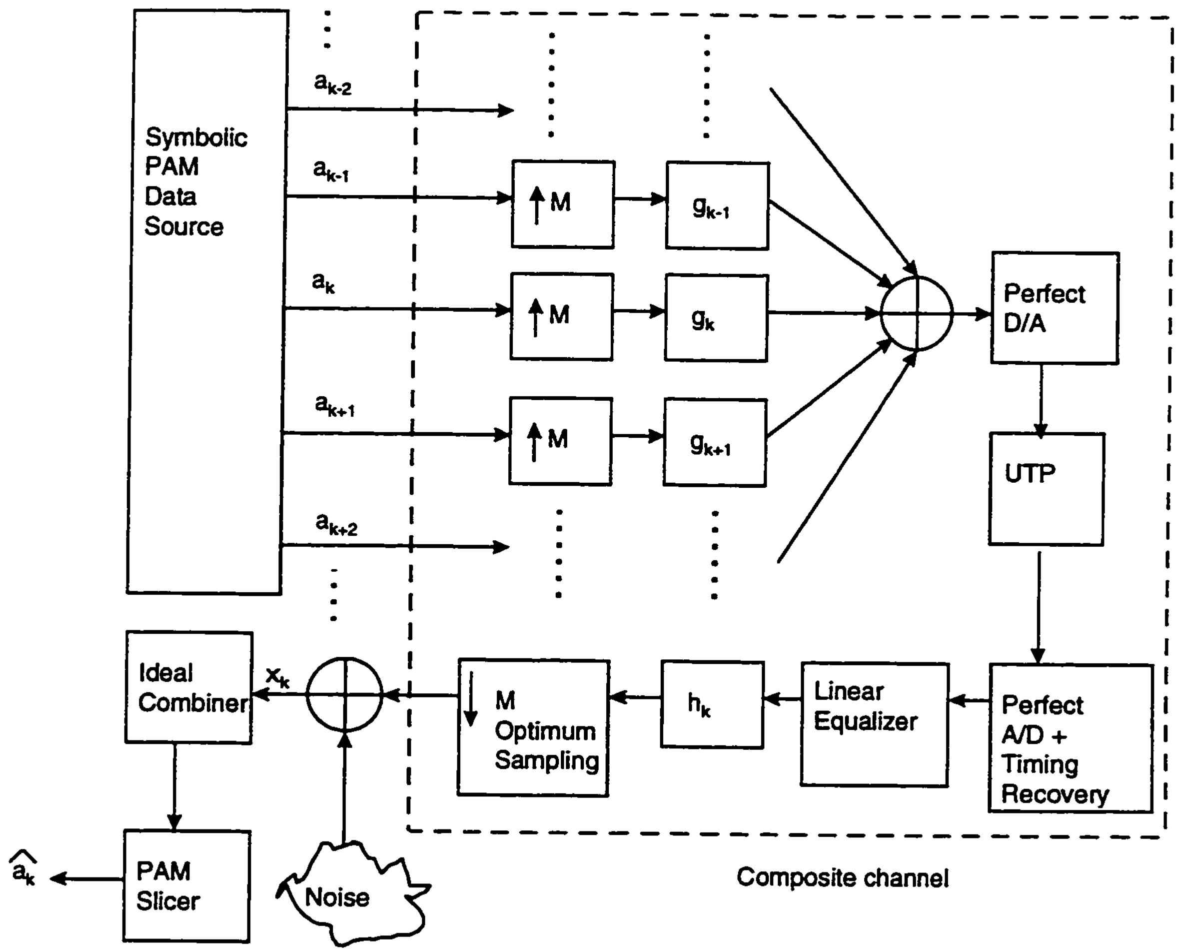

Figure 26: CMFB-DMT Semi-Analytical Simulation Block Diagram (for k^{th} Sub-Channel)

The basic structure of the performance simulation for a single sub-channel is represented by the flow chart in Figure 27.

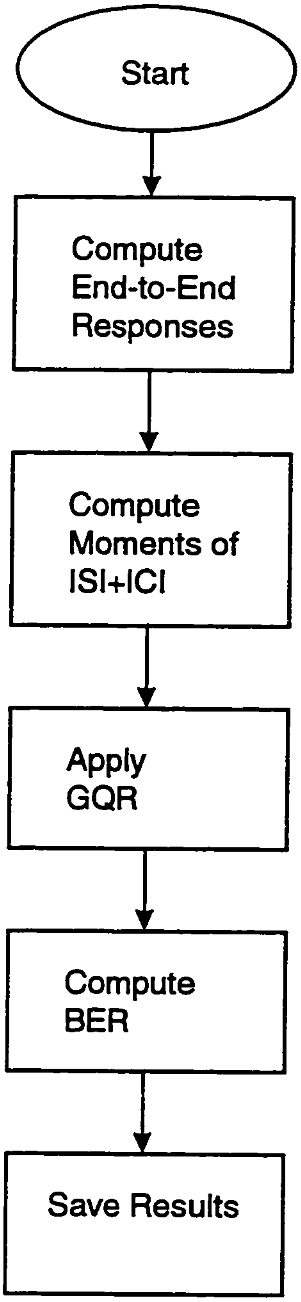

Figure 27: Flow-chart for Performance
Simulation of a Single Sub-Channel

5.2.1.1 Formulating the CMFB-DMT Simulation Problem

The decision variable at the output of sub-channel k for symbol instant 0 can be expressed as follows:

$$x_{k,0} = a_{k,0}v_0 + \sum_{n,n\neq 0} a_{k,n}v_n + \sum_{m,m\neq k}\sum_{n} a_{m,n}r_{m,n} + \eta \qquad \text{...(64).}$$

The variables, $a_{i,n}$, denote PAM symbol values on the i^{th} sub-channel at symbol instant n. The sequence v_n denotes the symbol spaced samples of the end-to-end pulse observed on sub-channel k. The sequences, $r_{m,n}$, are the symbol-spaced samples of the output pulses observed on sub-channel k due to the transmission of pulses on other sub-channels. The four terms in equation (64) represent the cursor, ISI, ICI and noise components, respectively, of the decision variable on sub-channel k. These associations are indicated in the following equations.

$$\begin{aligned}\text{Cursor} &= a_{k,0}v_0 \\ \text{ISI} &= \sum_{n,n\neq 0} a_{k,n}v_n \\ \text{ICI} &= \sum_{m,m\neq k}\sum_{n} a_{m,n}r_{m,n}\end{aligned} \qquad \text{...(65).}$$

The sequences, v_n, and $r_{m,n}$, can be expressed as follows:

$$\begin{aligned}v_n &= \downarrow T_{sym}\left[\tilde{g}_k * \tilde{h}_{UTP} * \tilde{h}_{eq} * \tilde{h}_k\right]_\phi \\ r_{m,n} &= \downarrow T_{sym}\left[\tilde{g}_m * \tilde{h}_{UTP} * \tilde{h}_{eq} * \tilde{h}_k\right]_\phi\end{aligned} \qquad \text{...(66)}$$

where $\downarrow T_{sym}[x]_\phi$ denotes selection down-sampling to the symbol rate taking into account the receiver timing phase, ϕ. As was the case in Section 5.1.1.1, the tildes in the equation above indicate that it refers to continuous-time equivalents to what are normally discrete functions in this work.

The receiver timing phase was chosen to maximize the figure of merit,

$$F = \frac{v_0^2}{\sum_{n,n\neq 0} v_n^2 + \sum_{m,m\neq k} \sum_n r_{m,n}^2} \quad \ldots(67),$$

for one of the sub-channels among those considered by the simulation. Equation (67) represents optimum sampling in the mean squared sense for this multicarrier PAM scenario.

Equation (64) represents the sum of numerous random PAM symbol values, each of which is weighted by some constant. Assuming that we have perfect AGC and standard PAM slicing and recalling that the PAM symbols are from the usual odd-integer set, the error scenario for sub-channel k is when the sum of the ISI, ICI and noise terms is greater than the magnitude of the cursor sample:

$$\left| \sum_{n,n\neq 0} a_{k,n} v_n + \sum_{m,m\neq k} \sum_n a_{m,n} r_{m,n} + \eta \right| > |v_0| \quad \ldots(68).$$

Assuming that η is Gaussian, we can formulate the symbol error probability on sub-channel k as:

$$P_e = \sum_p \frac{2(L_k - 1)}{L_k} Q\left(\frac{v_0 + \zeta_p}{\sigma_k} \right) f_\zeta(\zeta_p) \quad \ldots(69)$$

where L_k is the number of PAM levels on sub-channel k, σ_k is the noise variance observed on sub-channel k and ζ is the discrete random variable which represents the value of the ISI,

$$\zeta = \sum_{n,n\neq 0} a_{k,n} v_n + \sum_{m,m\neq k} \sum_n a_{m,n} r_{m,n} \quad \ldots(70),$$

and f_ζ is the probability mass function (PMF) of ζ. This function is estimated from the moments of ζ by application of the Gauss quadrature rules which are described in detail in [30].

5.2.1.2 Moment Computation

Computing the moments of ζ, $E\{\zeta^p\}$, involves computing the expectation of large polynomials in $a_{m,n}$. This is possible by application of the method employed in [30]. To illustrate this method, the mathematical developments for computing the moments of the ISI are shown below.

We can re-write the expression (65) for the ISI observed on sub-channel k as follows:

$$ISI = \sum_{n,n\neq 0} \xi_n \qquad \text{...(71)}$$

where

$$\xi_n = a_{k,n} v_n \qquad \text{...(72).}$$

The moments of the random variables ξ_n are given by:

$$E\{\xi_n^p\} = v_n^p \frac{2^p}{L_k} \sum_{l=1}^{L_k} (2l - 1 - L_k)^p \qquad \text{...(73)}$$

where L_k is the number of PAM levels on sub-channel k. The summation in (73) represents the sum of all of the odd-integer PAM levels raised to the power p. Note that, due to the symmetry of the PAM constellations about zero, the odd moments of the ξ_n are all zero.

We next apply recursion to find the cumulants of ξ_n

$$\vartheta_{p+1}(\xi_n) = E\{\xi_n^{p+1}\} - \sum_{r=0}^{p-1} \binom{p}{r} \gamma_{r+1}(\xi_n) E\{\xi_n^{p+r}\} \qquad \text{...(74)}$$

where the first cumulant is

$$\vartheta_1(\xi_n) = E\{\xi_n\} = 0 \qquad \text{...(75).}$$

Now, we compute the cumulants of the ISI:

$$\vartheta_p(ISI) = \sum_{n, n \neq 0} \vartheta_p(\xi_n) \qquad \ldots(76).$$

Finally, we compute the moments of ζ as:

$$E\{ISI^p\} = \vartheta_{p+1}(ISI) + \sum_{r=0}^{p-1} \binom{p}{r} \vartheta_{rp+1}(ISI) E\{ISI^{p-r}\} \qquad \ldots(77)$$

with the first moment given by

$$E\{ISI\} = \vartheta_1(ISI) \qquad \ldots(78).$$

The moment calculation algorithm as formulated above was adapted to compute the moments of the ICI observed on sub-channel k due to each other sub-channel. The same algorithm was then employed to compute the moments of the aggregate ISI and ICI, ζ, by combining the moments of the interference due to each sub-channel.

5.2.2 Simulation of FFT-DMT in the Presence of AWGN

Simulation of the performance of FFT-DMT in the presence of AWGN was based upon the block diagram shown in Figure 28. This block diagram is very similar to the block diagram for the CMFB-DMT simulation. This structure was chosen since it simplifies the formulating the simulation. At the transmitter, a symbolic QAM data sequence, $c_{i,n}$, is generated and routed to each transmit filter, $g_{i,n}$. These symbols are taken from the QAM constellations chosen by the bit allocation routine and the transmit filter amplitudes are scaled to achieve the optimized spectrum shape (which is designed to achieve a target value of $d_{RX\,k}/2\sigma_k$ on all sub-channels at the receiver). The resultant sequences from the transmit filter outputs are summed. The overall transmit sequence is sent through the D/A, the channel, A/D and linear equalizer. Next, the receive filter for the k^{th} sub-channel, f_k, is applied and the output is down-sampled to the symbol rate. This represents both stripping the cyclic prefix and the application of the analysis transform. Finally, additive noise referred to the output of the receive filter is introduced and QAM decision rules are applied.

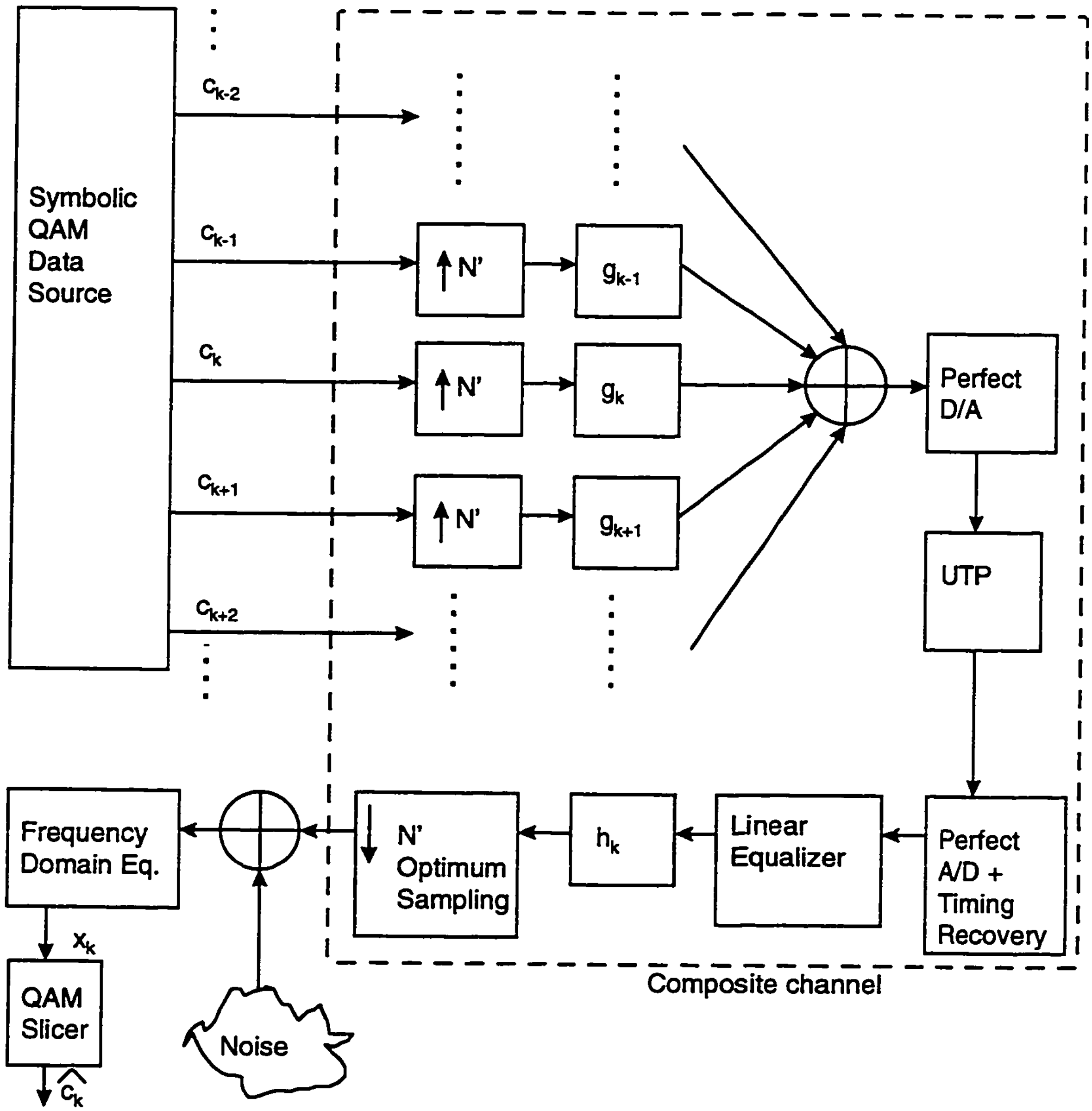

Figure 28: FFT-DMT Semi-Analytical Simulation Block Diagram (for k^{th} Sub-Channel)

5.2.2.1 Formulating the FFT-DMT Simulation Problem

The transmit filters for the FFT-DMT system are truncated complex exponential sequences formulated as in equation(30) which is repeated below for convenience:

$$g_{m,n} = \begin{cases} K_m \exp(j2\pi mn / N), & n = -\upsilon, \ldots, N-1. \\ 0, & \text{else.} \end{cases}$$

Recall that N_{FFT} is the transform size and υ is the cyclic prefix length. The overall length of the synthesis filters is $N' = N_{FFT} + \upsilon$, as suggested by the block diagram. For simplicity, the cyclic prefix and the gain to affect the spectrum shaping are incorporated in the definition of the synthesis filters.

After [54], the analysis or receive filters can be thought of as matched filters without the cyclic prefix. They can be expressed as:

$$h_{m,n} = \begin{cases} \frac{1}{\sqrt{N_{FFT}}} \exp(-j2\pi mn / N_{FFT}), & n = 0, \ldots, N_{FFT}-1. \\ 0, & \text{else.} \end{cases} \qquad \ldots(79).$$

The factor $1/\sqrt{N_{FFT}}$ ensures that each of the receive filters has unity gain.

The complex decision variable on sub-channel k can be expressed in the form of equation (64):

$$\begin{aligned} x_{k,0} &= \frac{1}{v_0}\left\{ c_{k,0} v_0 + \sum_{n,n\neq 0} c_{k,n} v_n + \sum_{m,m\neq k} \sum_{n} c_{m,n} r_{m,n} + \eta \right\} \\ &= c_{k,0} + \sum_{n,n\neq 0} c_{k,n} \frac{v_n}{v_0} + \sum_{m,m\neq k} \sum_{n} c_{m,n} \frac{r_{m,n}}{v_0} + \frac{\eta}{v_0} \end{aligned} \qquad \ldots(80).$$

The four terms in the equation above represent the cursor sample, the ISI on sub-channel k, the ICI due to transmission on all of the other FFT channels and the additive noise component respectively. The division by v_0 represents the application of the optimum frequency domain equalizer tap for sub-channel k: it corrects for both the attenuation and phase of the cursor.

The sequences v_n, and $r_{m,n}$ are formulated exactly as for CMFB-DMT:

$$v_n = \downarrow T_{sym}\left[\tilde{g}_k * \tilde{h}_{UTP} * \tilde{h}_{eq} * \tilde{f}_k\right]_\phi$$
$$r_{m,n} = \downarrow T_{sym}\left[\tilde{g}_m * \tilde{h}_{UTP} * \tilde{h}_{eq} * \tilde{f}_k\right]_\phi$$

where $\downarrow T_{sym}[x]_\phi$ denotes selection down-sampling to the symbol rate (each symbol has a duration equivalent to N' samples) taking into account the receiver timing phase, ϕ. In the case of FFT-DMT, v_n and $r_{m,n}$ are complex valued sequences due to that fact that the transmit and receive filters are complex.

The receiver timing phase was chosen to be optimum in the mean squared sense for one of the sub-channels considered. Since the symbol spaced sequences v and r_m are complex, the figure of merit which was maximized in choosing the timing phase is:

$$F = \frac{|v_0|^2}{\sum_{n,n\neq 0}|v_n|^2 + \sum_{m,m\neq k}\sum_{n}|r_{m,n}|^2} \qquad \ldots(81).$$

Next, we decompose the decision variable into real and imaginary parts representing the in-phase and quadrature phase PAM components, respectively:

$$\mathrm{Re}\{x_{k,0}\} = a_{k,0} + \sum\left[a_{k,n}v'_{R,n} - b_{k,n}v'_{I,n}\right] + \sum_{m,m\neq k}\sum_{n}\left[a_{m,n}r'_{R,m,n} - b_{m,n}r'_{I,m,n}\right] + \eta_R'$$
$$\mathrm{Im}\{x_{k,0}\} = b_{k,0} + \sum\left[b_{k,n}v'_{R,n} + a_{k,n}v'_{I,n}\right] + \sum_{m,m\neq k}\sum_{n}\left[b_{m,n}r'_{R,m,n} + a_{m,n}r'_{I,m,n}\right] + \eta_I'$$

$$\ldots(82).$$

In the equation above, substitutions have been made based upon the following relationships:

$$
\begin{aligned}
c_{m,n} &= a_{m,n} + jb_{m,n} \\
v'_{R,n} &= \mathrm{Re}\left\{\frac{v_n}{v_0}\right\} \\
v'_{I,n} &= \mathrm{Im}\left\{\frac{v_n}{v_0}\right\} \\
r'_{R,m,n} &= \mathrm{Re}\left\{\frac{r_{m,n}}{v_0}\right\} \\
r'_{I,m,n} &= \mathrm{Im}\left\{\frac{r_{m,n}}{v_0}\right\} \\
\eta'_R &= \mathrm{Re}\left\{\frac{\eta}{v_0}\right\} \\
\eta'_I &= \mathrm{Im}\left\{\frac{\eta}{v_0}\right\}
\end{aligned} \qquad \ldots(83).
$$

The error probability for the QAM signaling on sub-channel k can be approximated as the sum of the error probabilities of the in-phase and quadrature phase PAM. Furthermore, since the end-to-end sub-channel is linear, we can expect the probabilities of error on the in-phase and quadrature phase PAM components to be identical. Therefore we need only to compute the probability of error on the in-phase PAM component. Fortunately, equation (82) has basically the same form as equation (64) and we can apply the analysis used for CMFB-DMT as described in sections 5.2.1.1 and 5.2.1.2.

Chapter 6

Simulated Performance Results and Analysis

The results in this chapter are organized by impairment. Section 6.1 presents simulated BER performance results for 16-CAP CMFB-DMT and FFT-DMT in the presence of AWGN. In Section 6.2, the impact of self-FEXT on the performance of the three modulations is evaluated based upon more detailed link margin analysis than in Chapter 4. Finally, in Section 6.3, the simulated BER performance of 16-CAP VDSL with emission masking is considered as well as the spectral isolation properties of CMFB filter and the FFT.

6.1 Performance in the presence of AWGN

The BER performance in the presence of AWGN of the three modulations considered in this work was simulated using the time domain methods discussed in Chapter 5.

6.1.1 16-CAP

6.1.1.1 CAP-ADSL Transmission in the presence of AWGN

The parameters common to all simulations of 16-CAP ADSL transmission in this work are shown below in Table 8.

Table 8: 16-CAP-ADSL Parameters

Parameter	Value
Data Rate	6 Mbps
Raised Cosine Pulse Roll-off	0.25
Carrier Frequency	0.9875 MHz
Symbol Rate	1.5 Mbaud
Minimum Frequency	50 kHz
Sampling Frequency	6.0 MHz

As was the case for the link budget calculations in Chapter 4, the in-band transmit and receive shaping pulses were computed from a base-band square root raised cosine characteristic. The distortionless end-to-end pulses have square root raised cosine frequency response. The pulse roll-off factor indicates that 25 % excess bandwidth was used as in the link margins.

The following table indicates the number of DFE taps used for the different loop lengths considered. These quantities were determined by applying a threshold to the end-to-end impulse response as indicated in Chapter 2. The threshold value was small, 0.001 to ensure that the equalizer span covered a generous part of the dispersed pulse.

Table 9: Number of DFE Taps Used in 16-CAP ADSL Simulations

Loop Length - [m]	# Feed-Forward Taps	# Feed-Back Taps
100	2	2
500	4	4
1000	6	6
1500	10	6
2000	11	10

The equalizers were initially trained for approximately 32000 symbols using a (small) step size, 1e-4, and then frozen for the performance simulation. The combination of long training sequence and a relatively small step size were chosen to ensure that the equalizer coefficients were close to their optimum values. Figure 29 shows the simulated performance for the various parameters listed above.

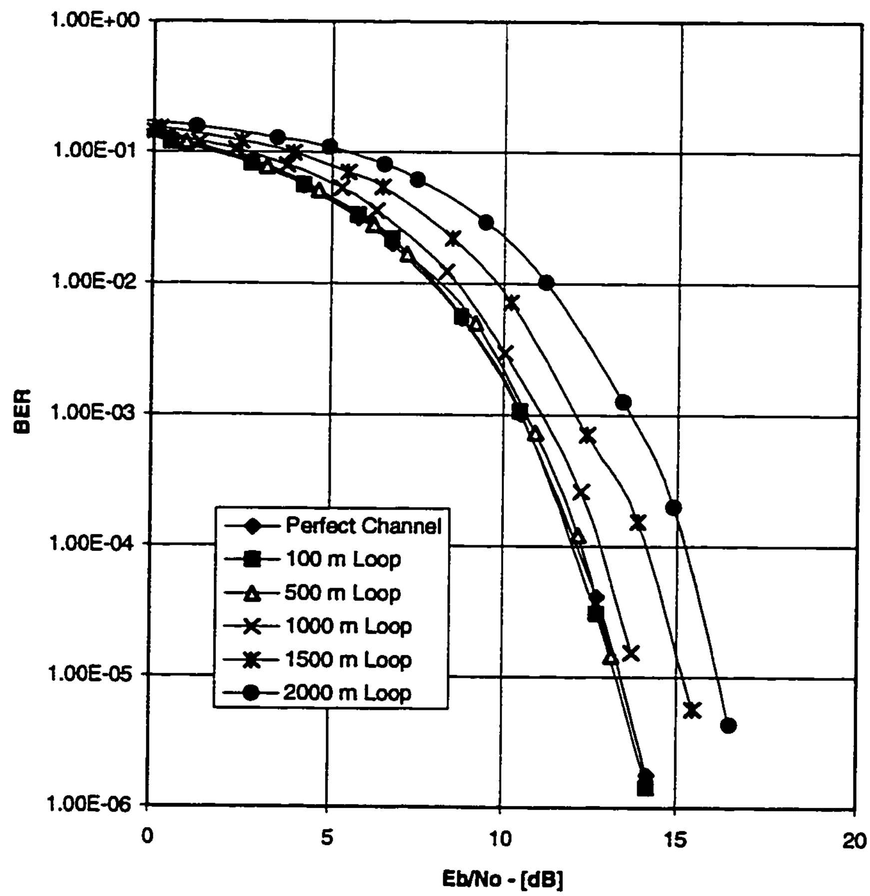

Figure 29: 16-CAP ADSL Performance in the Presence of AWGN

Under the simulated conditions, the performance of 16-CAP is nearly ideal for loop lengths under 1000 m. For the 1000 m loop, a penalty of approximately 1 dB per 500 m at BER = 1e-5. These penalties can be attributed to noise enhancement and residual error in the DFE coefficients at the end of the training period.

6.1.1.2 CAP-VDSL Transmission in the Presence of AWGN

Common parameters among all simulations of 16-CAP VDSL transmission in this work are shown below in Table 10.

Table 10: 16-CAP-VDSL Parameters

Parameter	Value
Data Rate	26 Mbps
Raised Cosine Pulse Roll-off	0.25
Carrier Frequency	4.1125 MHz
Symbol Rate	6.5 Mbaud
Minimum Frequency	50 kHz
Sampling Frequency	26 MHz

Once again, the pulse roll-off parameter refers to the fact that the undistorted end-to-end raised cosine frequency response used 25 % excess bandwidth. A square root raised cosine pulse was used as the baseband pulse in computing both the transmit and receive shaping filters.

The number of DFE taps required for CAP transmission at the VDSL rate was determined using the threshold method mentioned earlier in this work (with threshold value 0.001). The following table indicates the number of feed-forward and feed-back taps used in the simulations. As was the case for the simulations at the ADSL data rate, a long training sequence, approximately 65000 symbols, was used with a small adaptation step size, 1e-4, to obtain DFE coefficients close to the optimum values for each SNR.

Table 11: Number of DFE Taps Used in 16-CAP VDSL Simulations

Loop Length - [m]	# Feed-Forward Taps	# Feed-Back Taps
100	3	4
500	10	8
1000	17	12

The results of simulations based upon the parameters indicated above are shown below in Figure 30.

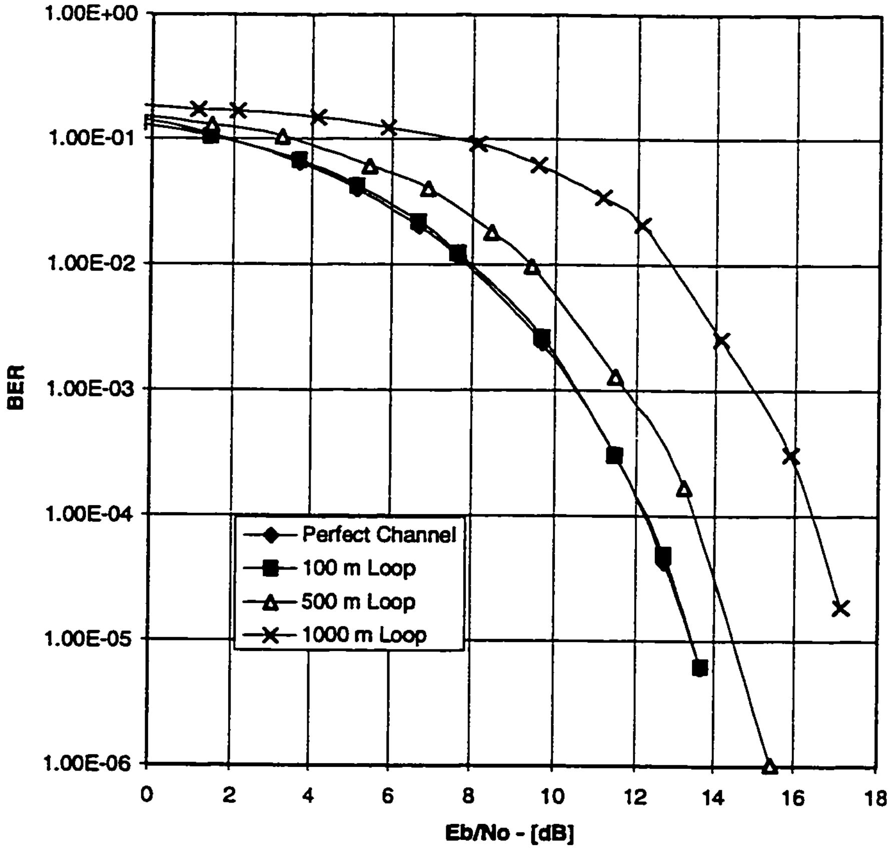

Figure 30: 16-CAP VDSL Performance in the Presence of AWGN

The simulation results show that the performance of 16-CAP VDSL is essentially ideal on the short 100 m loop. A penalty of approximately 1 dB is observed for the 500 m loop at BER = 1e-5. If we extrapolate the plot, the observed penalty on the 1000 m loop is a somewhat poor 4 dB at BER = 1e-5. As was the case for the ADSL simulations, these penalties can be attributed to noise enhancement and residual error in the DFE coefficients. The effects of noise enhancement are more significant for VDSL than for ADSL since the VDSL signal bandwidth is approximately 4 times that of the ADSL signal. The attenuation experienced by the high frequency edge of the VDSL signal is therefore much higher.

6.1.2 Multi-carrier Modulations

6.1.2.1 How Many Sub-Channels ?

One of the first questions which should be answered in designing any multicarrier communications link is: "How many sub-channels ?"

Consider the BER performance curves shown in Figure 31 which were obtained for FFT-DMT signaling with the parameters listed in Table 12.

No cyclic prefix or TEQ were employed. Ideal frequency-domain equalization was employed (this equates to perfect AGC plus phase correction on each sub-channel). As was the case for the link margin computations, the bandwidth was chosen to be approximately 1 MHz. This is the minimum bandwidth for a 64-CAP signal and close to the bandwidth employed in the ADSL standard. Note that the performance curves in Figure 31 are plotted versus $\gamma = d_{RX\,k}/2\sigma_k$ since this is the target parameter used in the bit allocation and spectrum optimization and the received SNR is different on each sub-channel.

In order to accelerate the simulations which used a large number of sub-channels, the BER curves were generated considering the performance of a maximum of 40 sub-channels using no more than 60 sub-channels as sources of ICI. The sub-channels which were considered in the simulations were at the low frequency end of the signal band when more than 40 sub-channels were available. These sub-channels were found to dominate the performance since they carry the largest constellations (because the frequency response of UTP is a monotonically decreasing function of frequency). The 10^{th} sub-channel considered in the simulation was used to set the timing phase according to equation (81). The simulations of the BER performance of FFT-DMT at the ADSL and VDSL rates which are discussed in Section 6.1.2.3 were also performed using a similar reduced set of sub-channels.

Table 12: Parameters for FFT-DMT Simulations Without TEQ or CP

Parameter	Value(s)
Bit rate	6 Mbps
Band	50 kHz - 1 MHz
Sampling Frequency	2 MHz
UTP length	1000 m
Transform Size	64, 128, 256, 512, 1024, 2048

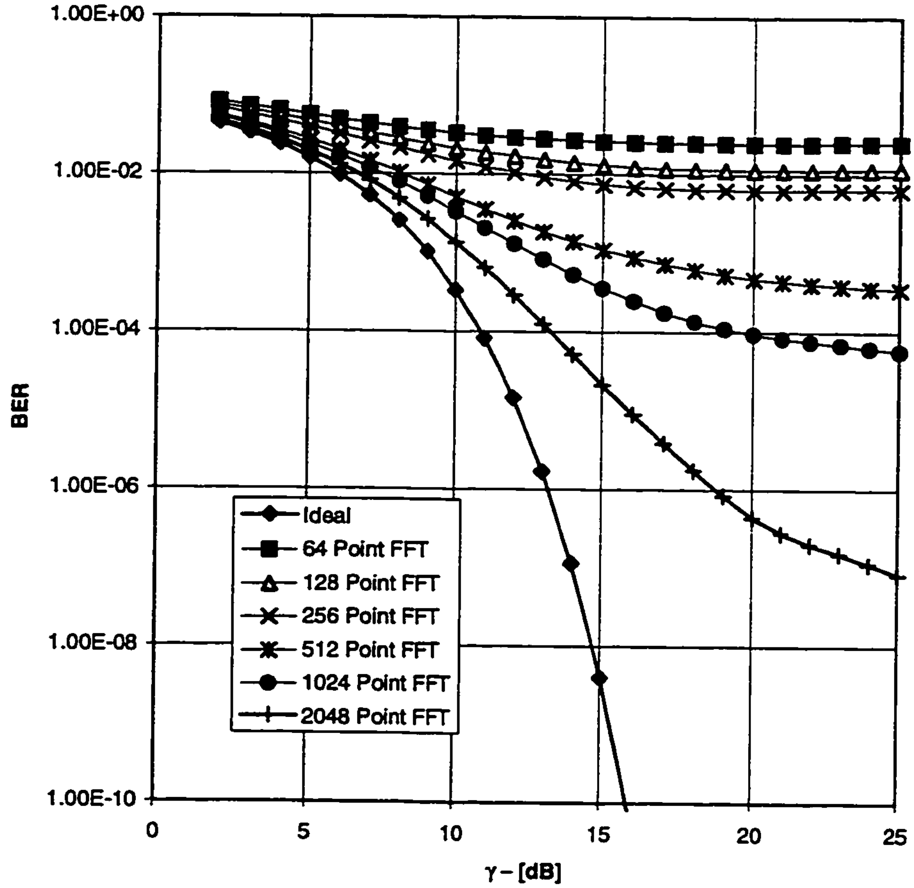

Figure 31: Performance of FFT-DMT in the Presence of AWGN with no CP or TEQ

The curves in Figure 31 show the satisfying result that as the number of sub-channels increases, the error rate performance improves. This is expected since the channel frequency response becomes closer to ideal in each sub-band as the sub-bands decrease in width. Looking at this from the time-domain perspective, the symbol period becomes long as the number of sub-channels increases. When the symbol period is long compared to the channel impulse response, the leakage between symbols becomes less significant.

Notice, however, that the transform size gets somewhat large before the error performance becomes acceptable – even though the loop length is moderate. The performance would likely be much worse on a longer loop or one that has bridged taps because the duration of the channel impulse response would be longer.

On one hand, it is desirable to have narrow bandwidth sub-channels since this increases the flexibility of the spectrum optimization. An excessively large transform size is not desirable though, since it may increase the end-to-end latency and it increases the complexity (cost) of the transceiver. The multicarrier solutions currently discussed in the literature address this tradeoff by using relatively high average sub-channel bandwidth efficiency to minimize the overall signal bandwidth, a moderate transform size chosen based upon what is practical to implement, and some elements of equalization.

6.1.2.2 CMFB-DMT

6.1.2.2.1 Evaluating the Different Equalization Options

Chapter 2 identified two equalization methods for CMFB-DMT, namely the use of a linear FIR filter at the receiver input and the use of post-detection combining. The results presented in this section demonstrate that the most efficient equalization solution for CMFB-DMT uses both equalization methods.

Consider the scenario of a 2000 m loop carrying 6 Mbps (the representative ADSL rate). Table 13 indicates the common parameters for the simulation results in this section.

The simulations of the performance of CMFB-DMT were performed considering a reduced set of sub-channels as was the case for the FFT-DMT simulations. Each BER curve is the aggregate BER simulated on 25 sub-channels using a set of 50 sub-channels to generate ICI for each sub-channel observed. The set of sub-channels used in the CMFB-DMT simulations was located near the low frequency end of the signal band. These sub-channels experience the worst impairment by ISI and ICI due to their relatively large constellations. The 10^{th} sub-channel considered by the simulation was used to set the timing phase. These conditions apply to the simulation results in the following sections as well.

Table 13: CMFB-DMT ADSL Parameters

Parameter	Value
Bit rate	6 Mbps
Transform Size	256 sub-channels, $g = 4$
Maximum Bit Load per Sub-Channel	7 bits
Available Band	50 kHz - 1.0 MHz
Sampling Frequency	2 MHz

The simulated performance of CMFB-DMT using only FIR equalization at the receiver input is shown in Figure 32. The FIR equalizers were computed based upon the design of the optimum linear MSE equalizer in [49].

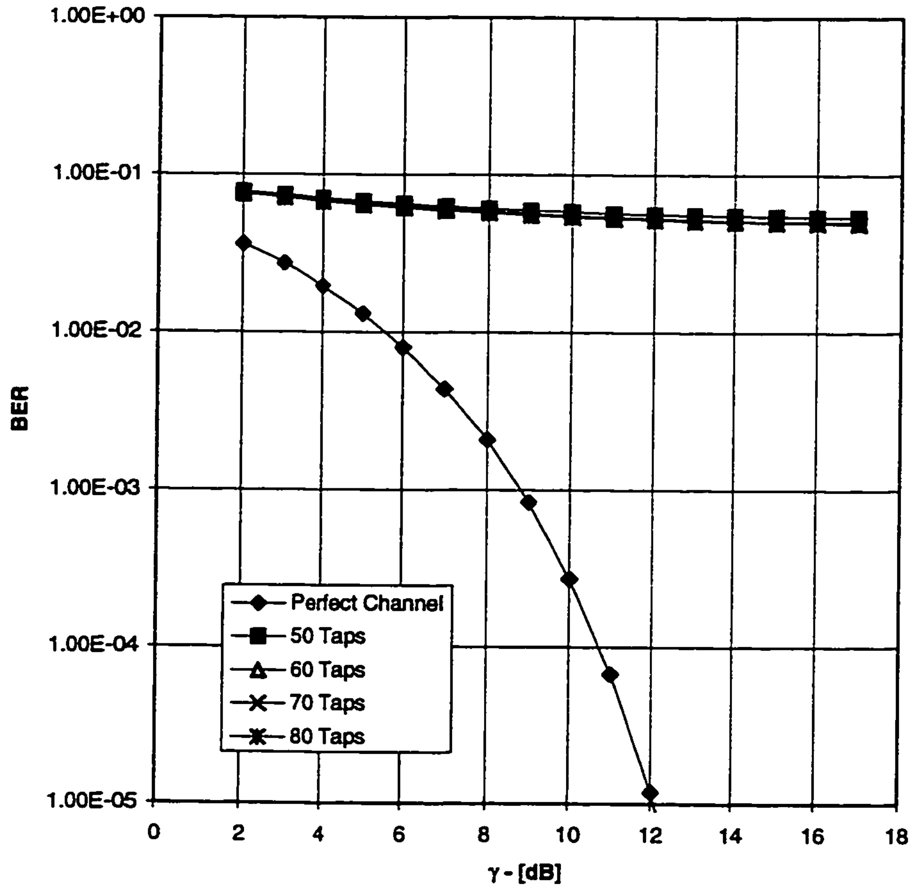

Figure 32: CMFB-DMT ADSL Performance on 2000 m Loop Using FIR Equalizer Only

As can be seen from Figure 32, the FIR equalizer used alone has minimal value. The small amount of residual distortion which exists with even rather long FIR equalizers as well as any reconstruction error due to numerical imperfections in the undistorted filter bank are enough to cause significant ISI and ICI. Recall that the maximum PAM constellation size used is 128 – even a relatively small amount of cross-talk can cause significant peak-distortion. As a result, the performance is poor using only the FIR equalizer.

Let us next consider the performance of CMFB-DMT using only idealized post-detection combining. Performance curves using a variety of combiner dimensions are shown in Figure 33. The combiner dimensions are stated in the form $|\Omega|$-$|T|$ where $|\Omega|$ denotes the number of sub-channels considered by the combiner (analogous to the "width" in the frequency domain) and $|T|$ denotes the number of symbol periods considered by the combiner (the "length" in the time-domain). The combiner dimensions are all odd since we only consider combiners which have a span in the time-frequency plane that is symmetric about the desired symbol. This is the case for the 3-3 combiner illustrated in Figure 9.

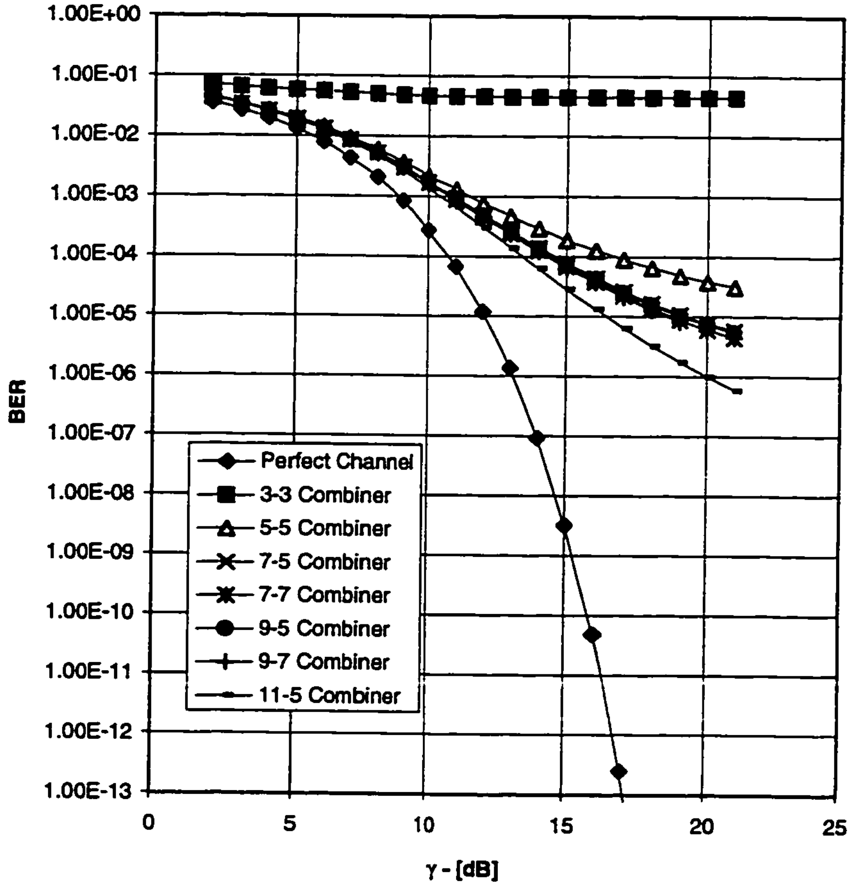

Figure 33: CMFB-DMT ADSL Performance on 2000 m Loop Using Idealized Post-Detection Combining

The performance curves in Figure 33 indicate that the post-detection combiner, when used alone, should provide significantly better performance than an FIR equalizer. These results are somewhat optimistic since the combiner is assumed to function in an ideal manner. There is not much advantage to increasing the combiner dimensions beyond 5-5. The error performance is still poor using the relatively large (55 taps) 11-5 combiner. Inspection of the crosstalk coefficients, v_n and $r_{m,n}$ from equation (64), indicates most of the ISI and ICI energy is confined to the span of the 5-5 combiner (which includes results from two sub-channels on either side of the desired one and two symbols before and after the desired symbol). There is also some minor but non-negligible output from many of the sub-channels not covered by the combiner within the 5 symbol times long period. These observations can be related to the properties of the filter bank. Since the genus number is 4, the detector outputs due to each symbol overlap the detector outputs for four other symbols (two before and two after the desired symbol). Furthermore, each sub-channel has the most significant spectral overlap with two neighboring sub-channels on either side of it in the frequency domain.

It turns out that we can improve upon both of the previous scenarios by using the combiner and the FIR equalizer together. The results in the following figure show the performance of CMFB-DMT ADSL on a 2000 m loop using an ideal 5-5 combiner and various FIR equalizer lengths. The combiner dimensions were chosen based upon the results in Figure 33.

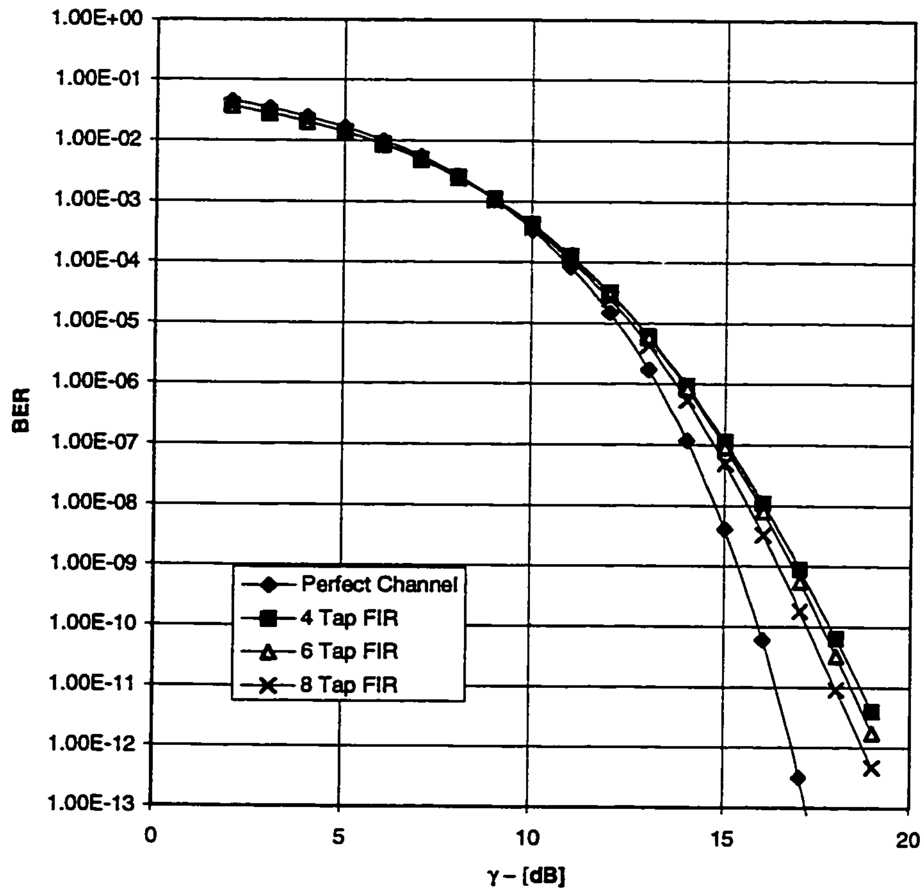

Figure 34: CMFB-DMT ADSL Performance on 2000 m Loop Using an Ideal 5-5 Post-Detection Combiner and FIR Equalizers

The results in Figure 34 indicate that the use of a short FIR equalizer in conjunction with the reasonably sized post-detection combiner can provide good CMFB-DMT performance. We conclude that the most efficient equalization scheme for CMFB-DMT incorporates both the post detection combiner and a linear equalizer.

6.1.2.2.2 CMFB-DMT ADSL Transmission in the Presence of AWGN

The performance of CMFB-DMT ADSL was simulated for different loop lengths using the basic parameters in Table 13. FIR equalization was employed along with a 5-5 post-detection combiner. The FIR equalizer lengths used for the loop lengths considered are shown in Table 14. For the 100 and 500 m loops, it was determined that no FIR equalizer was necessary.

Table 14: FIR Equalizer Lengths Used in CMFB-DMT ADSL Simulations

Loop Length - [m]	# FIR Equalizer Taps
100	0
500	0
1000	4
2000	8

Performance curves simulated using the conditions mentioned above are shown in Figure 35.

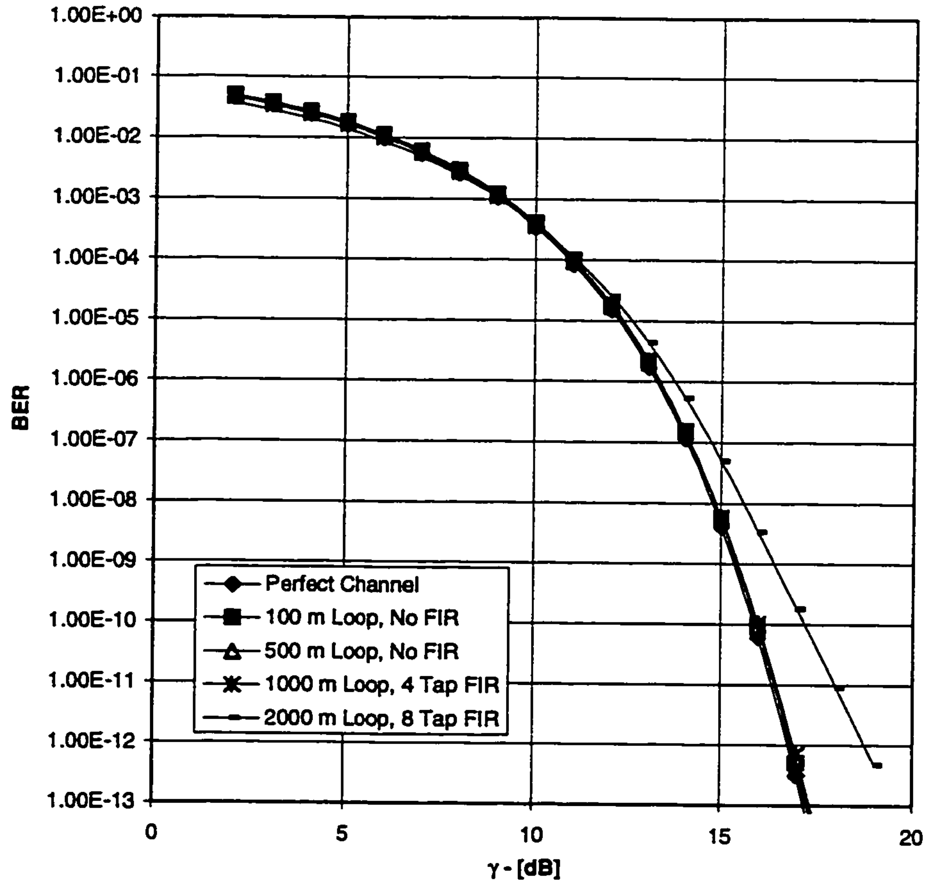

Figure 35: CMFB-DMT ADSL Performance in the Presence of AWGN (With Optional FIR Equalization and Ideal 5-5 Post-Detection Combiner)

The curves in Figure 35 indicate that the combination of a linear pre-detection equalizer and a post-detection combiner should be very effective at minimizing the effects of ISI. The results above are optimistic, since ideal combining without noise enhancement (as described in Section 2.2.4) is assumed.

6.1.2.2.3 CMFB-DMT VDSL Transmission in the Presence of AWGN

The basic set of parameters which were held constant in the simulations of the performance of CMFB-DMT VDSL transmission in the presence of AWGN are included in Table 15. Simulation results indicated that a 5-5 post-detection combiner was sufficient. This is reasonable since the genus of the filter bank is 4 and the frequency domain characteristics of the 512 sub-channel filter bank were designed to be similar to those of the 256 sub-channel bank.

Table 15: CMFB-DMT VDSL Parameters

Parameter	Value
Bit rate	26 Mbps
Transform Size	512 sub-channels, $g = 4$
Post-Detection Combiner Dimensions	5-5
Maximum Bit Load per Sub-Channel	7 bits
Available Band	50 kHz - 4.33 MHz
Sampling Frequency	8.67 MHz

The FIR equalizer lengths used for the different loop lengths considered in the CMFB-DMT VDSL simulations are listed in Table 16.

Table 16: FIR Equalizer Lengths used in CMFB-DMT VDSL Simulations

Loop Length - [m]	# FIR Equalizer Taps
100	0
500	6
1000	12

Performance curves for CMFB-DMT VDSL transmission in the presence of AWGN are shown in Figure 36.

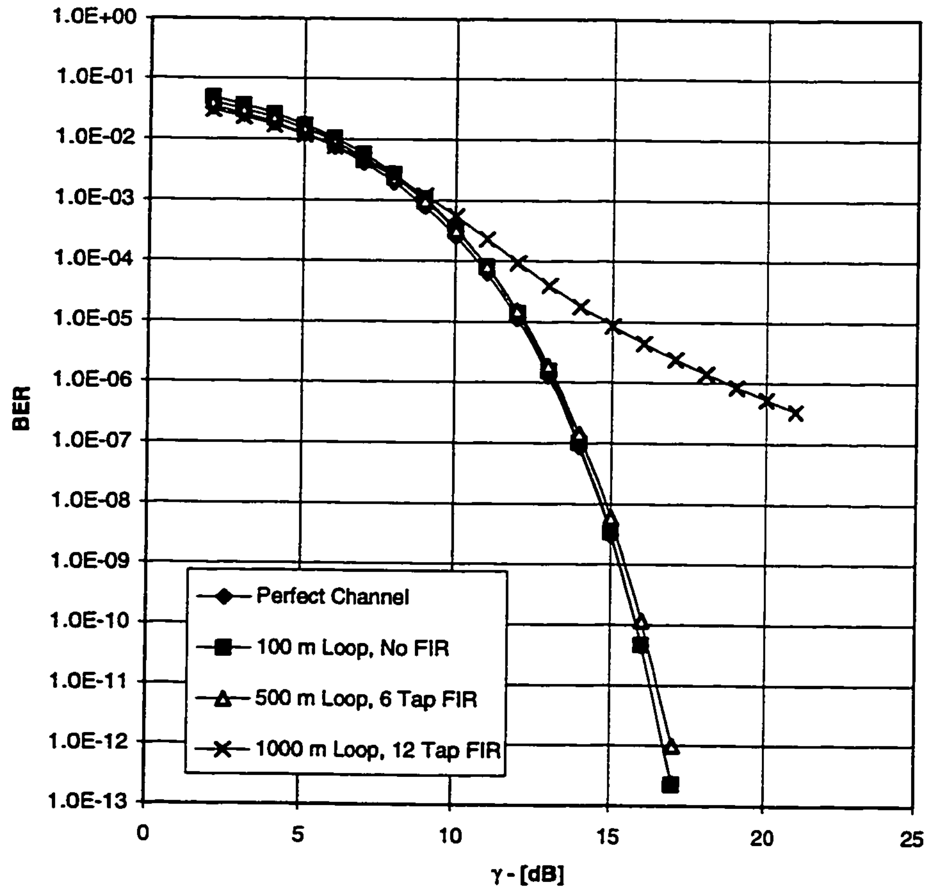

Figure 36: CMFB-DMT VDSL Performance in the Presence of AWGN(With Optional FIR Equalization and 5-5 Post-Detection Combiner)

The combination of the FIR equalizer and post-detection combiner are quite successful at mitigating the effects of ISI and ICI on the 100 m and 500 m loops. The BER performance on the 1000 m loop is less than satisfactory. This is due to the residual ISI and ICI which exists after application of the finite dimension FIR equalizer and combiner. Since the 1000 m loop had a steep attenuation response, a fairly large number of low-frequency sub-channels (in fact, all of the sub-channels considered in the simulation) carried the maximum bit load allowed in the simulation, 7 bits. These large constellations are very susceptible to peak distortion.

Additional simulations of the 1000 m loop, and observation of the ISI and ICI impulse responses indicated that no significant benefit could be obtained by moderate increases the length of the FIR equalizer or the dimensions of the combiner. It was determined, however, that by reducing the maximum allowable sub-channel bit load, reasonably good performance was possible. The following figure shows the BER performance on the 1000 m loop with a maximum sub-channel bit load of 6 bits. The simulated performance using 6 bits as the maximum bit load is shown for comparison.

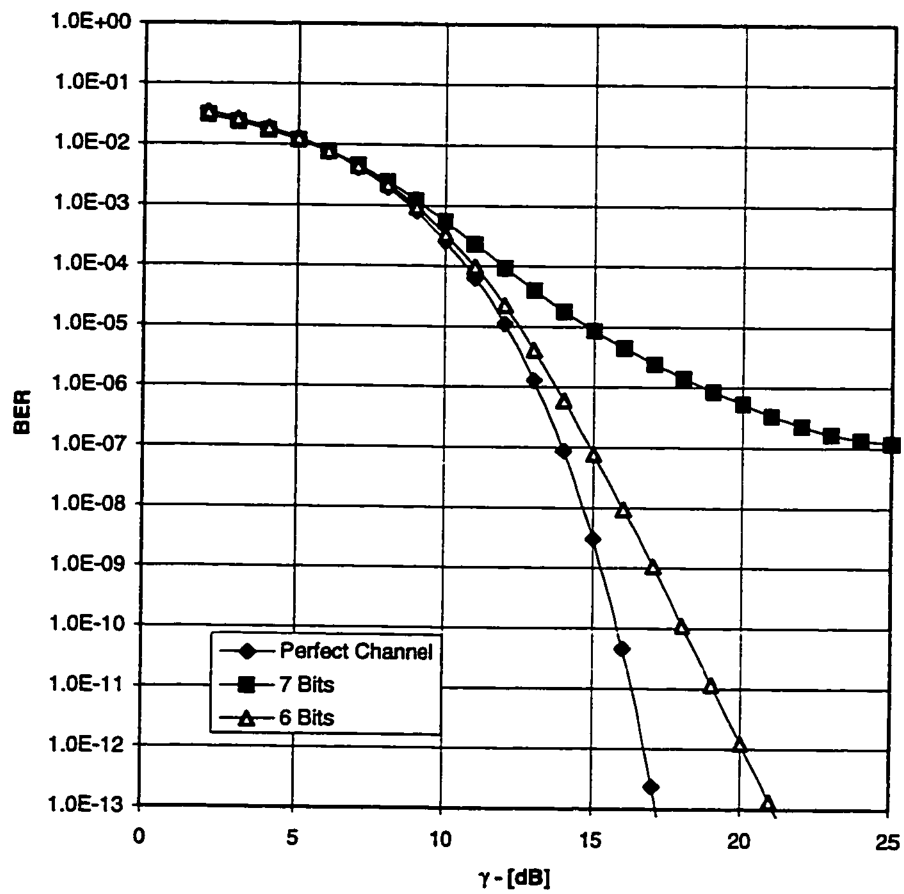

Figure 37: CMFB-DMT VDSL Performance on 1000 m Loop Using a Reduced Maximum Sub-Channel Bit Load

The curves in Figure 37 indicate that decreasing the maximum allowable constellation order to 6 bits can improve the performance on the 1000 m loop significantly. The smaller constellations have less dynamic range in the symbol amplitudes and therefore are more robust in the presence of ISI and ICI. Note that a transmit power penalty is incurred by reducing the maximum constellation size since more bits must be transmitted on the higher frequency sub-channels which experience more attenuation.

6.1.2.3 FFT-DMT

6.1.2.3.1 FFT-DMT ADSL Transmission in the Presence of AWGN

The parameters which were held constant in all of the FFT-DMT ADSL simulations are identified in Table 17. As was the case for the link margin calculations, the signal bandwidth was chosen such that target bandwidth efficiency on the sub-channels is 6 bps/Hz (this is similar to the ADSL standard). The transform size and CP length are chosen to be the same as used in the ADSL standard. This transform size is reasonably economical to implement and the capacity reduction due to the cyclic prefix, $\upsilon/N_{FFT}+\upsilon$, is small – approximately 5.9 %.

Table 17: FFT-DMT ADSL Parameters

Parameter	Value
Bit rate	6 Mbps
Transform Size	512 points (or 256 sub-channels)
CP Length	32 samples
Maximum Bit Load per Sub-Channel	14 bits
Available Band	50 kHz - 1.0 MHz
Sampling Frequency	2 MHz

The number of TEQ taps used for the various loop lengths considered are shown in Table 18. The TEQ lengths were chosen based on trial and error with the goal of achieving the best performance using as few taps as possible.

Table 18: TEQ Lengths Used in FFT-DMT ADSL Simulations

Loop Length - [m]	# TEQ Taps
200	2
500	5
1000	8
2000	12

The following figure shows the simulated performance of FFT-DMT in the presence of AWGN for the various parameters mentioned above. The simulations used ideal frequency domain equalization as discussed in Chapter 5 and the optimum TEQ taps computed using the LS-UEC design method mentioned in Chapter 2.

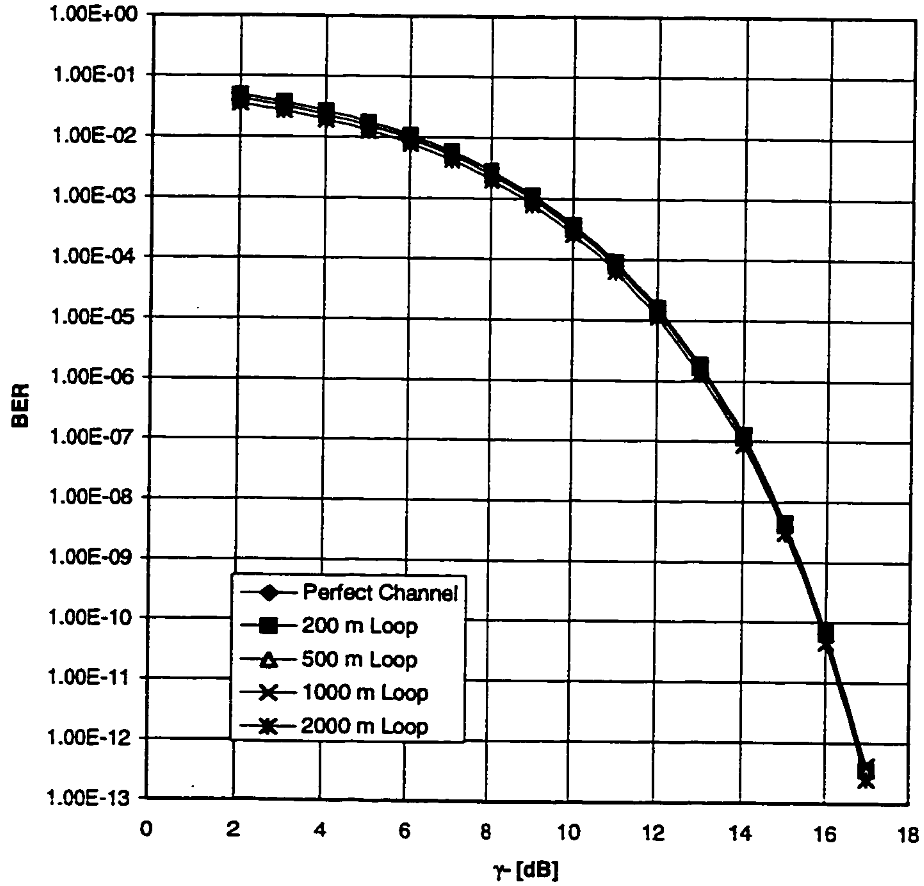

Figure 38: FFT-DMT ADSL Performance in the Presence of AWGN

As can be seen from Figure 38, the performance is practically ideal, independent of loop length. There is no visible penalty due to noise enhancement from the equalizer because the sub-bands are narrow and the equalizer gain is close to uniform across them. The FDEQ taps were ideal and the TEQ taps were computed using perfect knowledge of the channel impulse response. Therefore, we do not observe any degradation due to imperfect tap weights. Since the number of taps is small, however, we can hypothesize that the impact of small amounts error in the TEQ and FDEQ taps would be minimal.

6.1.2.3.2 FFT-DMT VDSL Transmission in the Presence of AWGN

The common parameters for the FFT-DMT VDSL simulations are shown below in Table 19. The signal bandwidth is chosen to achieve the same spectral efficiency target as was used in the ADSL simulations, 6 bps/Hz. Since the sampling rate is about 4 times higher in the VDSL case than it was for the ADSL simulations, the channel impulse response is expected to have a proportionately longer duration in discrete samples. In order to help combat the effects of the longer channel response, the transform size was increased to 1024 points. This transform size is not unreasonable to implement. Given the signal bandwidth and this transform size, the sub-channel bandwidth for the VDSL scenario is still small – about 8.5 kHz. The cyclic prefix duration was chosen to be 64 samples in order to make the capacity reduction ratio, $\upsilon/N_{FFT}+\upsilon$, the same as it was in the ADSL simulations (~5.9 %).

Table 19: FFT-DMT VDSL Parameters

Parameter	Value
Bit rate	26 Mbps
Transform Size	1024 points (or 512 sub-channels)
CP Length	64 samples
Maximum Bit Load per Sub-Channel	14 bits
Available Band	50 kHz - 4.33 MHz
Sampling Frequency	8.67 MHz

As was the case for the ADSL simulations, the TEQ lengths were chosen based upon trial and error. The TEQ lengths used to obtain the FFT-DMT VDSL performance results presented in this section are shown below inTable 20.

Table 20: TEQ Lengths Used in FFT-DMT VDSL Simulations

Loop Length - [m]	# TEQ Taps
200	2
500	5
1050	16

The simulated performance of FFT-DMT VDSL transmission for the various parameters indicated above is shown below inFigure 39.

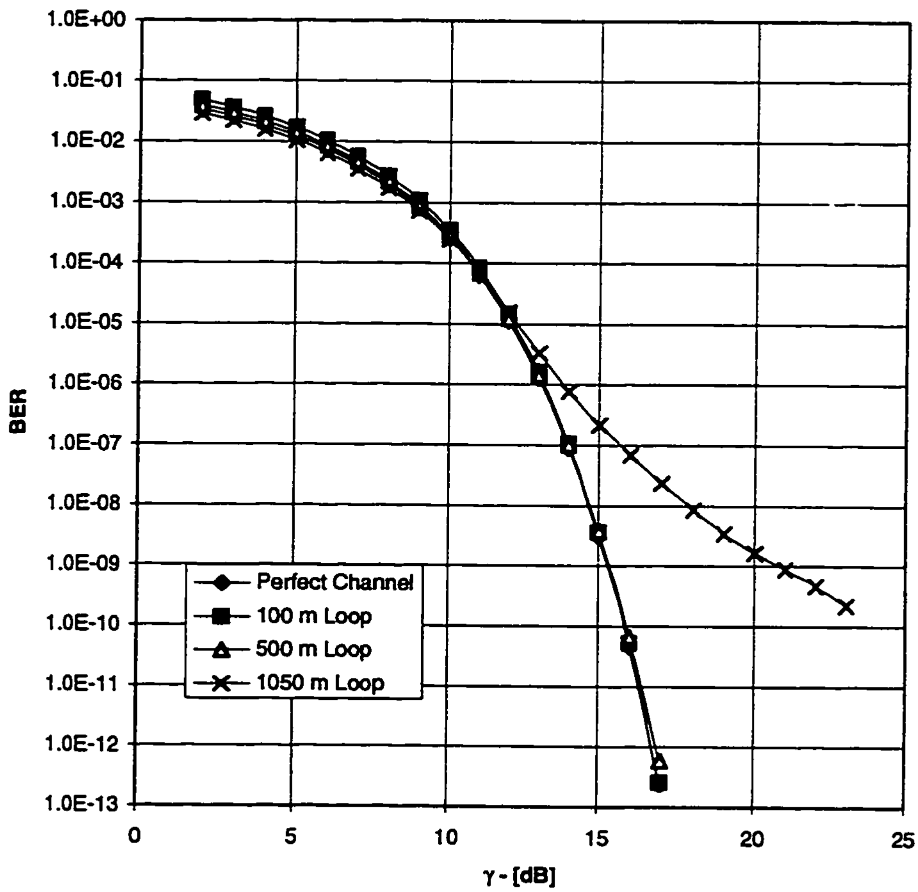

Figure 39: FFT-DMT VDSL Performance in the Presence of AWGN

The curves in Figure 39 are very similar to the results for CMFB-DMT VDSL in Figure 36. Nearly ideal performance is observed on the relatively short 100 m and 500 m loops. Again, it is important to point out that the TEQ and frequency domain equalizer taps have optimum values computed with perfect knowledge of the channel response. It is not possible to observe a penalty due to noisy tap weights. The results do indicate that the combination of TEQ, cyclic prefix and FDEQ is a very efficient means of mitigating ISI and ICI for this scenario.

The degraded performance on the 1050 m loop is due to the fact that many sub-channels carry large 14 bit constellations and there is some residual distortion in shortened channel impulse response. As was the case for CMFB-DMT, it was determined that moderate increases in the length of the FIR equalizer (TEQ) did not correct this problem. Reducing the maximum allowable sub-channel bit load to 12 bits caused a marked improvement in the performance on the 1050 m loop. This fact is illustrated by the performance curves in Figure 40.

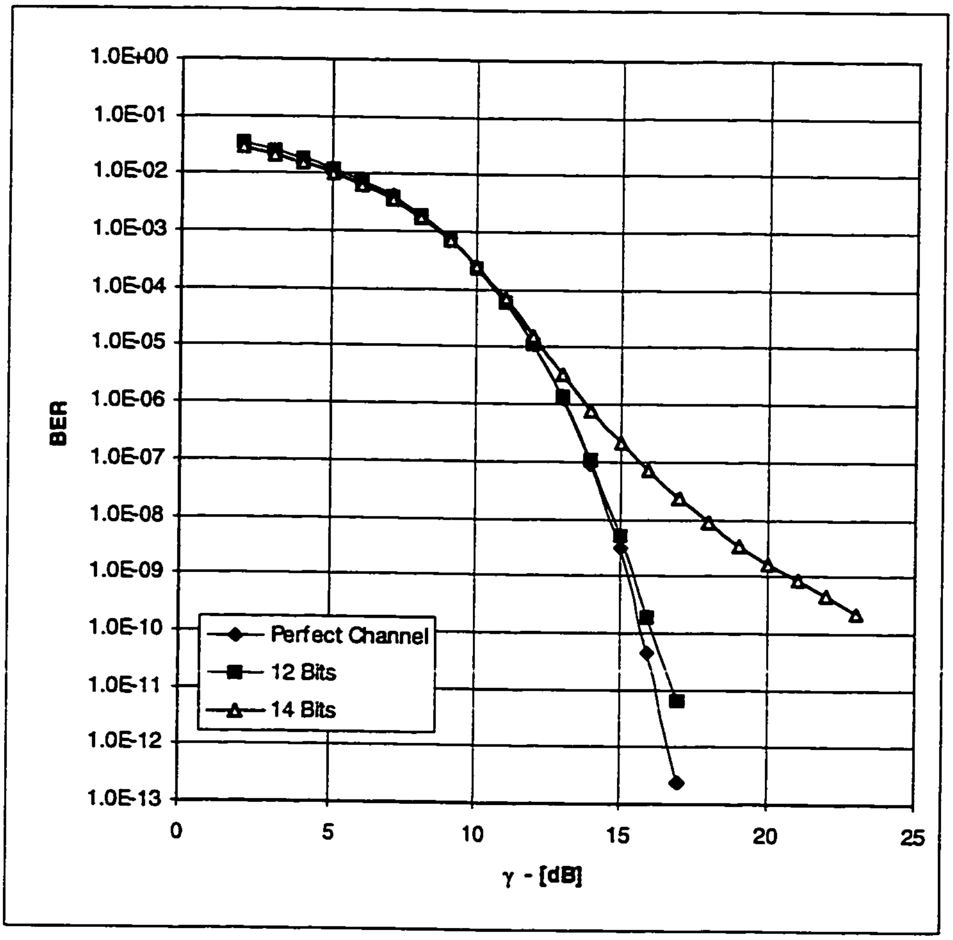

Figure 40: FFT-DMT VDSL Performance on 1050 m Loop Using a Reduced Maximum Sub-Channel Bit Load

The simulated BER curves for the 1000 m VDSL loops using both multicarrier modulations point out an interesting trade-off in the multicarrier signal design problem.

On long, highly attenuating loops the theoretically optimum bit allocation requires the use of large constellations on the low frequency sub-channels. Very large constellations (such as the 14 bit QAM constellation, for example) require practically perfect elimination of ISI and ICI which is generally not possible using finite length filters. Had finite precision computations and imperfect channel characterization been incorporated into the simulations, this would have magnified the problems with the large constellations. A practical multicarrier modem design has to balance these issues.

6.2 Performance in the Presence of self-FEXT

In general, self-FEXT causes an error floor at some very small error rate. This is illustrated in the following figure which shows the symbol error rate (or SER) performance of 16-CAP transmission at the VDSL rate on a 500 m loop as determined using the frequency domain methods. The parameters used to generate the curves were the same as in Table 10. The abscissa in Figure 41 is the ratio of the signal power to the power of AWGN at the receiver input (*SNRg*).

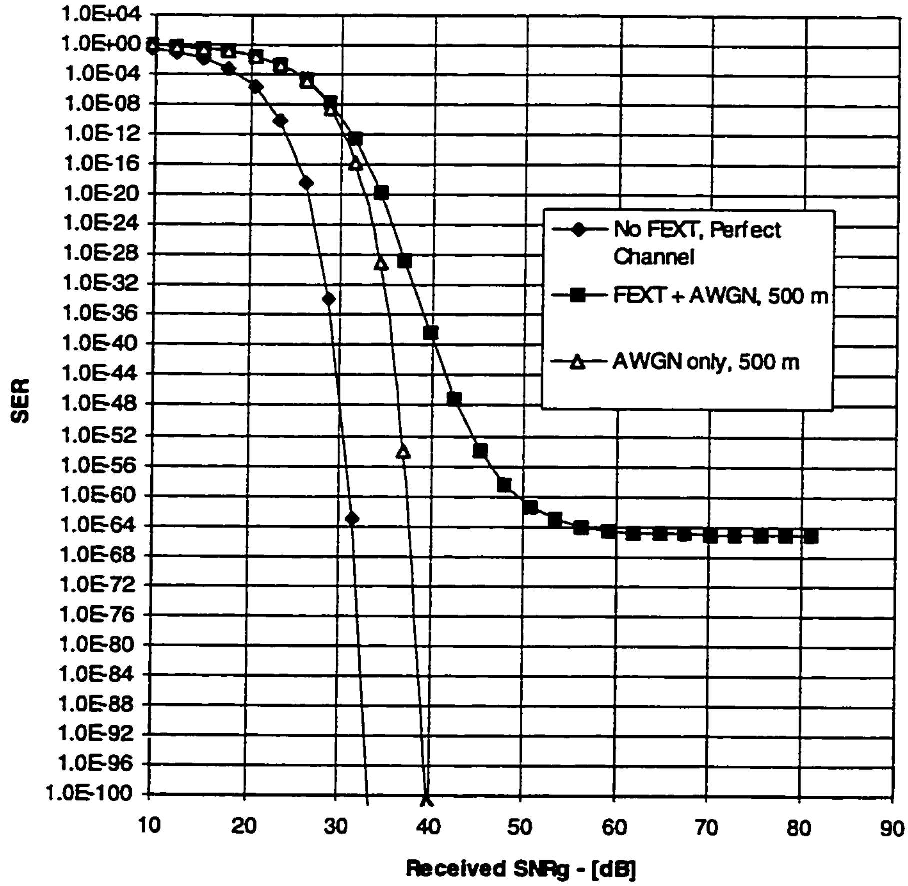

Figure 41: 16-CAP VDSL Symbol Error Rate Performance in the Presence of FEXT (500 m Loop, Infinite ZF-DFE)

When the received signal power is relatively small ($SNRg$ < 30 dB), the performance is dominated by AWGN. As the received signal power increases, the FEXT PSD begins to emerge from the AWGN floor and we begin to observe a penalty due to FEXT. Once the signal power is high enough, the AWGN PSD level becomes negligible compared to the self-FEXT PSD in the signal band. At this point, the slicer SNR ceases to increase as the received signal power increases because the FEXT PSD is proportional to the signal PSD at each frequency in the signal band. The result of the slicer SNR leveling off is an error floor. We can think of this phenomenon as the loop becoming saturated by FEXT noise at some input power level.

Error performance curves which show the self-FEXT error floor are difficult to generate (and to present in a clear fashion) because of the small error probabilities involved. In the following sections, the effects of FEXT on the performance of 16-CAP and multicarrier modulations will be studied by observing how the link margin varies with transmitted power.

6.2.1 Performance of 16-CAP in the Presence of Self-FEXT

Due to the small magnitude of self-FEXT relative to the signal amplitude it was not feasible to observe the effect of FEXT on BER performance using the Monte-Carlo simulation. The small error rates associated with the relatively high SNR's at which FEXT is significant would have taken years to simulate by this method. The effects of self-FEXT on BER performance were observed using a frequency domain simulation based upon link budget calculations described in Section 4.1.

The link budget calculation program was adapted to calculate the link margin for 16-CAP transmission on a specific loop length for a variety of input powers.

The symbol error rate (SER) performance curves used to illustrate the self-FEXT error floor phenomenon in Section 6.2 were constructed from link margin results. The slicer SNR was determined from the link margin at various input powers and then equation (53) was applied to compute the SER.

6.2.1.1 ADSL Data Rate

Link margin curves for 16-CAP transmission at the 6 Mbps ADSL data rate were computed assuming the basic signal parameters listed in Table 8. The performance target relative to which the margins were computed was BER = 1e-7. The following figure shows the link margin trajectories as a function of signal power on 100 m, 1000 m and 2500 m loops both with and without self-FEXT. The number of FEXT disturbers used in the computations is 49 as in Chapter 4. The results in Figure 42 include the noise enhancement penalty due to the ideal, infinite ZF-DFE.

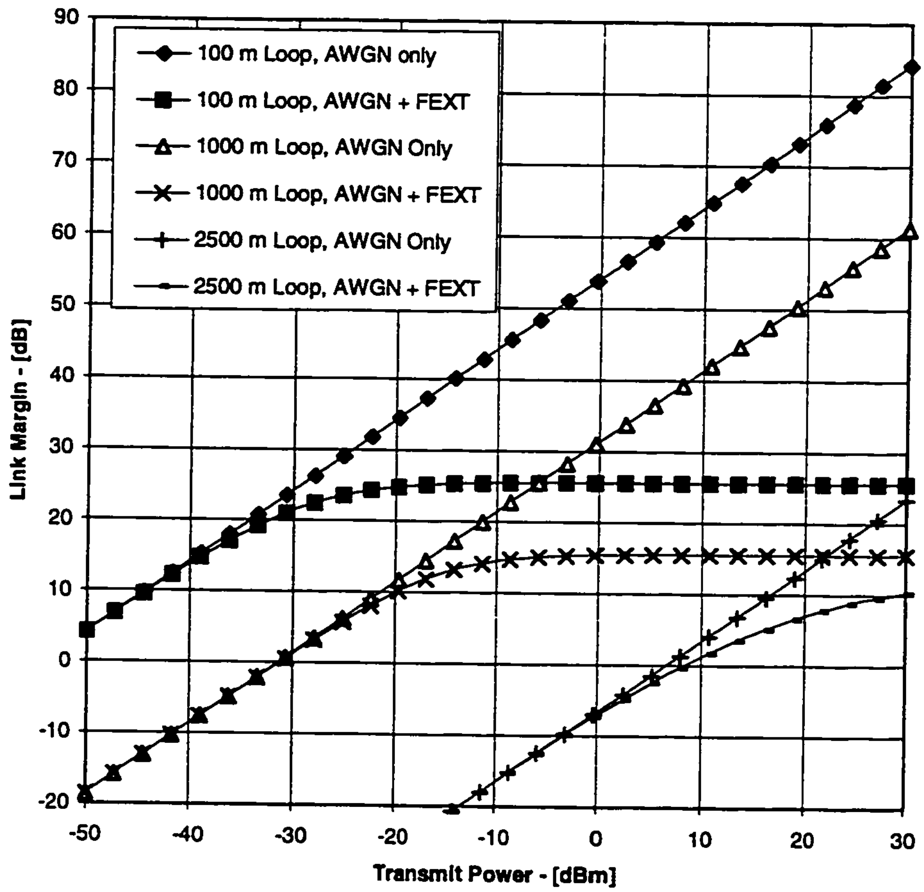

Figure 42: 16-CAP ADSL Link Margin Performance vs. Transmit Power

The link margin curves above tell essentially the same story as the SER performance curves in Figure 41. On each loop, we observe that when the input power is below some threshold, the performance is AWGN dominated. This can be attributed to the fact that the self-FEXT spectrum is not significant compared to the AWGN level. As the input power increases, the FEXT spectrum emerges from the AWGN floor and the margin performance becomes FEXT limited. The FEXT limited margins are a monotonically decreasing function of loop length as observed in Chapter 4.

6.2.1.2 VDSL Data Rate

Assuming the basic parameters for the 16-CAP VDSL signal listed in Table 10, link margin versus transmit power curves were computed for 100 m, 500 m and 1000 m loops. As in the previous sections, the performance target used to compute the margins was BER = 1e-7 (SNR ~ 21.5). The curves in Figure 43 show the margin performance in the presence of AWGN only and in the presence of both AWGN and 10 disturber self-FEXT.

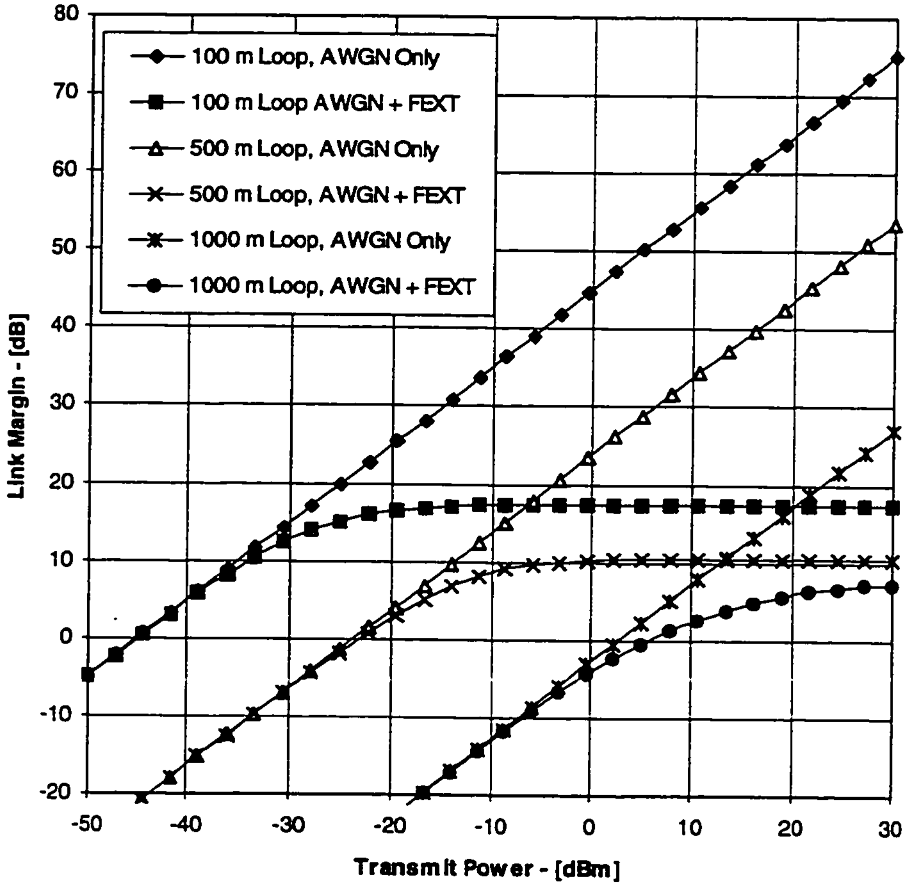

Figure 43: 16-CAP VDSL Link Margin Performance vs. Transmit Power

The results in Figure 43 are very similar to the results obtained for the ADSL data rate. The fact that the FEXT limited margins are not much lower for the VDSL scenario compared to the ADSL case indicates that the less severely attenuated low frequency band edge plays an important role in determining the margin performance.

6.2.2 Performance of Multicarrier Modulations in the Presence of Self-FEXT

As was the case for 16-CAP modulation, the impact of self-FEXT on the performance of the multicarrier modulations was examined by observing link margins as a function of input power on different loops. The link margin analysis mentioned in Chapter 4 was applied to computing link margin versus input power curves for different loop lengths.

As in Chapter 4, the margin analysis assumes that FFT-DMT and CMFB-DMT margins are equivalent. This assumption is based upon the fact that the two modulations have similar bandwidth efficiency on each sub-channel under the following conditions: 1) no cyclic prefix is used for the FFT-DMT system; 2) the CMFB and FFT-DMT systems have equivalent bandwidth; and 3) the CMFB and FFT-DMT systems use the same number of sub-channels.

The link margin approach was chosen primarily to ensure that the results for 16-CAP and the multicarrier modulations are comparable. The 16-CAP link margins are computed assuming an ideal, infinite ZF-DFE and therefore no penalty due to ISI is included. Some (small) residual ISI and ICI is present in the simulated multicarrier systems due to the fact that the equalizers are finite. Had the semi-analytical simulations been employed, the residual ISI and ICI would have incurred a penalty which does not exist in the CAP margin results at the low error probabilities where self-FEXT is significant.

It should be noted that the link margin calculations for the multicarrier modulation schemes do not include any penalty due to noise enhancement from equalization. Based upon the simulated BER performance of FFT-DMT in the presence of AWGN (see Section 6.1.2.3), it is arguable that the noise enhancement penalty is minimal because the sub-channels have narrow bandwidth.

6.2.2.1 ADSL Data Rate

With the exception of the cyclic prefix length, which was set to zero, the FFT-DMT ADSL signal parameters in Table 17 were used to compute the link margin curves shown in Figure 44. The performance target for the margin calculations was the same as used earlier for 16-CAP, namely BER = 1e-7.

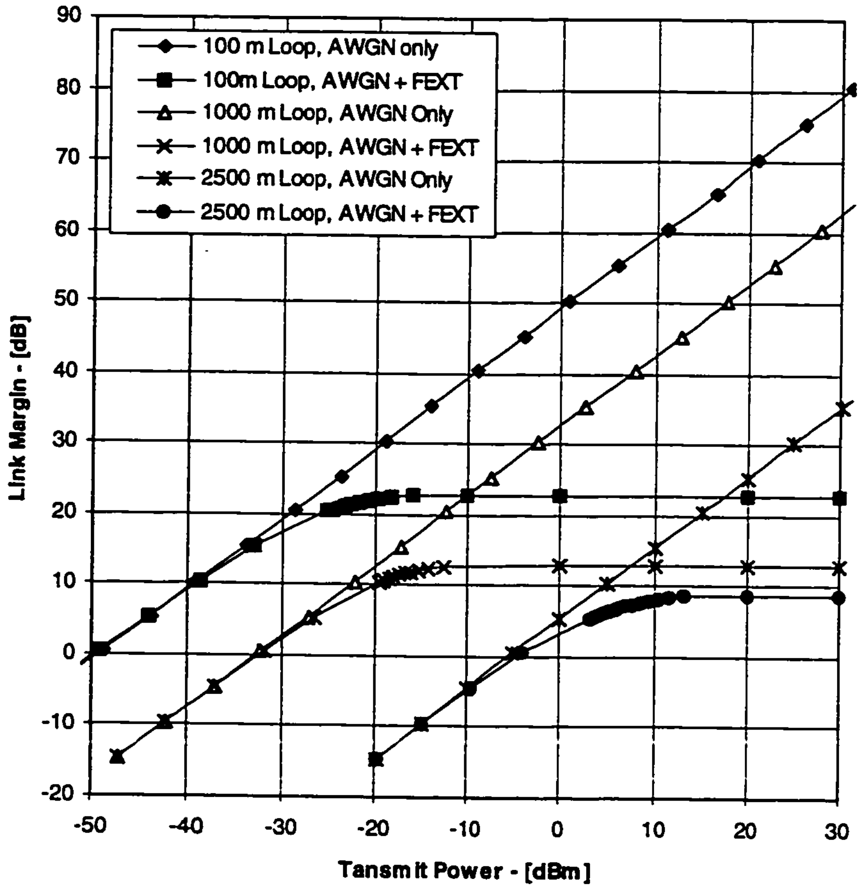

Figure 44: Multicarrier ADSL Margin Performance vs. Transmit Power

The results above reinforce some earlier observations.

Multicarrier modulations offer a performance advantage over 16-CAP on AWGN dominated loops with moderate to heavy attenuation. This is because, by this analysis, the multicarrier schemes do not suffer from significant penalties due to equalizer noise enhancement while the 16-CAP scheme does. With reference to the results for 16-CAP in Figure 42, observe that for the mildly attenuating 100 m loop, the 16-CAP margins are better when AWGN dominated. This is due to the fact that the optimized multicarrier signal has higher average bandwidth efficiency and therefore has a higher SNR requirement. For the longer 1000 m and 2500 m loops the multicarrier margins are better in the AWGN dominated regime because of the significant noise enhancement penalty from the CAP DFE.

The performance of multicarrier modulations in the FEXT-dominated regime is at best only comparable to the performance of CAP. The FEXT-dominated margins for 16-CAP in Figure 42 are actually slightly better than those observed for the multicarrier schemes in Figure 44. Based upon the margin results in Chapter 4, this can be attributed to the higher bandwidth efficiency of the multicarrier signal.

6.2.1.1 VDSL Data Rate

Performance margins relative to the BER = 1e-7 target were computed for multicarrier signaling at the VDSL data rate. The parameters in Table 19, which describe the FFT-DMT VDSL signal, were used to compute the margins. The cyclic prefix length was set to zero to respect the conditions required for the assumption that the CMFB-DMT and FFT-DMT margins are equivalent. The margin versus transmit power curves are included below in Figure 45.

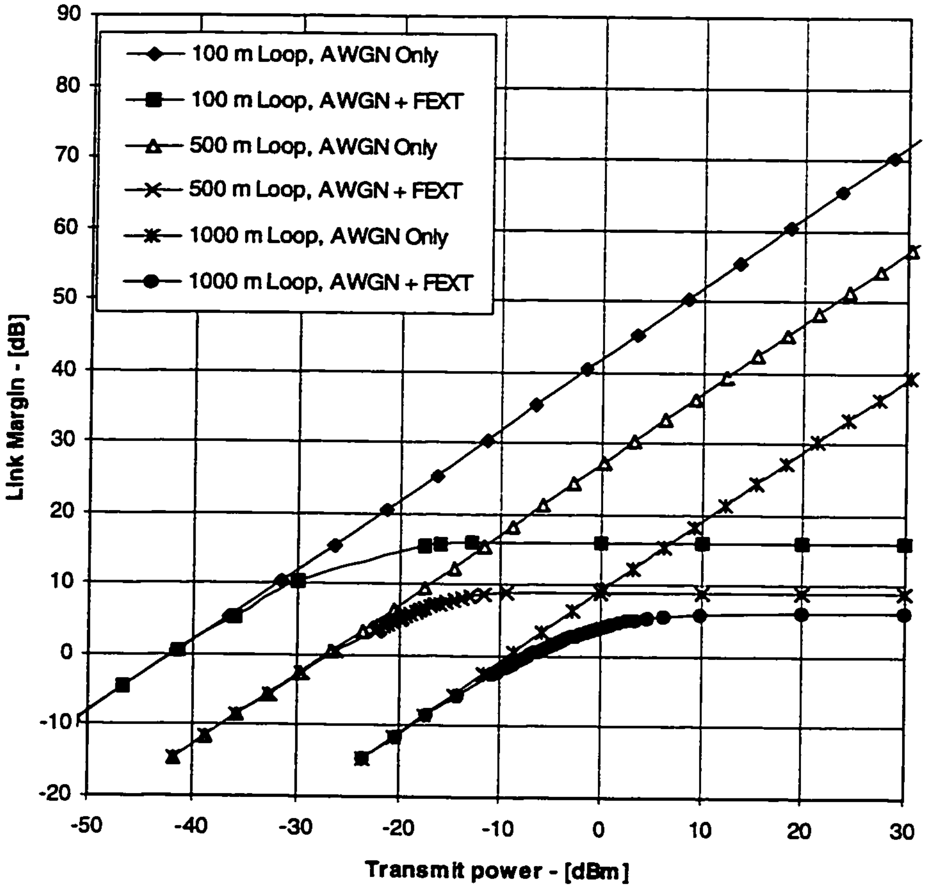

Figure 45: Multicarrier VDSL Margin Performance vs. Transmit Power

The results above in Figure 45 and the margin curves for 16-CAP VDSL in Figure 43 are consistent with our earlier observations for the ADSL scenario. The multicarrier margins are better than those for 16-CAP on the 500 m and 1000 m loops under AWGN dominated conditions. This is due to the DFE noise enhancement penalty which degrades the CAP performance. For the short, 100 m loop under AWGN dominated conditions and for all of the loops considered under self-FEXT dominated conditions, the multicarrier margins are very similar to the 16-CAP margins. There is no obvious advantage in either case. These observations are similar to those made by Zervos and Kalet in [69] considering NEXT impaired transmission over UTP.

6.3 Emission Masking and Narrow-Band Interference

This section discusses briefly the impact of emission masking on CAP transmission at the VDSL rate and the spectral isolation properties of the FFT and CMFB transform.

6.3.1 Performance of CAP with Emission Masking

The performance of CAP signaling at the VDSL data rate with emission masking was simulated using the Monte-Carlo simulator used to obtain the results in section 6.1. The program was modified to include -20 dB notches in the end-to-end frequency response. These notches corresponded to the four amateur radio bands of Table 1. The notch filtering was accomplished using a 2048 tap linear phase FIR filter. The transition bands at the edges of each notch were approximately 40 kHz wide.

The simulations employed the parameters in Table 10 along with the DFE dimensions listed below. The number of DFE taps was determined in each case using the threshold method employed earlier on in this work. The threshold value was 0.001 as in the previous cases.

Table 21: Equalization Requirements for 16-CAP-VDSL with Emission Masking

Loop Length - [m]	# FF Taps	# FB Taps
100	18	75
500	25	88
1000	34	90

The emission masking filter had the effect of dramatically increasing the duration of the end-to-end impulse response. This is reflected in the estimated equalization requirements above. As one might expect, it proved to be somewhat difficult to get the huge equalizers to converge using the standard LMS algorithm primarily because they were very sensitive to the choice of step size. For the sake of consistency with the simulations discussed earlier, a long training period – approximately 65000 symbols – was employed with a small step size 0.00005.

The simulated performance results are shown below in Figure 46.

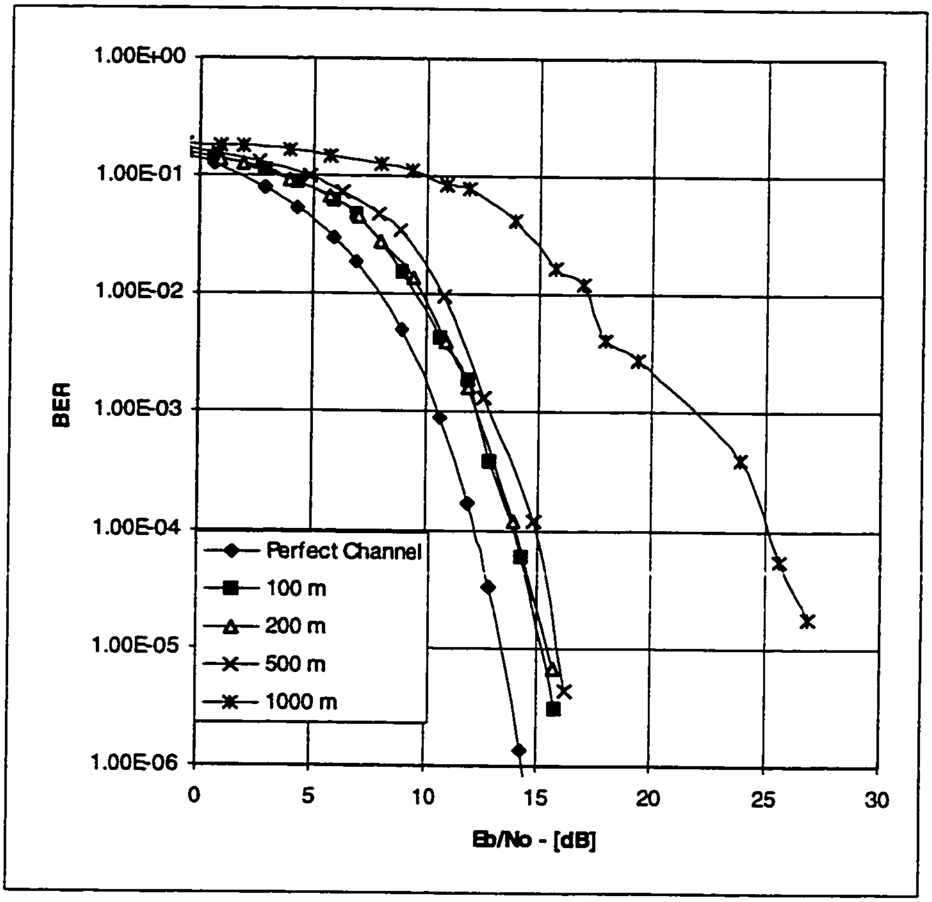

Figure 46: CAP-VDSL Performance with Emission Masking

The simulated performance curves show higher penalties: approximately 2 dB for the 100 m loop at BER = 1e-5; close to 3 dB for the 500 m loop at the same error rate. Without emission masking, essentially no penalty was observed on the 100 m loop and the penalty on the 500 m loop was 1 dB at BER = 1e-5. The 2 dB increase in the penalties observed on the short loops when emission masking is present can be attributed to noise enhancement and the higher residual error associated with the increased number of DFE taps. Note that this is slightly better than the 3 dB penalty due to noise enhancement observed in the link margin results of Chapter 4. This can be attributed to two factors: 1) the margins in Chapter 4 included a penalty due to the reduction in transmitted power due to the masking notches which is not included here; and 2) in Chapter 4 the DFE's were assumed to be designed with respect to the zero forcing criterion whereas the MSE criterion is used here. Since the SNR's considered are relatively low, we should expect the MSE criterion DFE to provide somewhat better performance than the ZF criterion DFE.

In the case of the 1000 m loop, large penalties are observed due to the imperfect convergence of the equalizers – even after the relatively long training period.

In this case, one way in which we can improve performance on the 1000 m loop is to decrease the number of DFE taps. By increasing the threshold employed in determining the number of DFE taps required to 0.005 the estimated number of DFE taps required for the 500 m and 1000 m loops was reduced by about 30 %. Table 22 below indicates the number of DFE taps required with the new threshold for the 500 m and 1000 m loops.

Table 22: Equalization Requirements for 16-CAP VDSL with Emission Masking Determined Using a Larger Magnitude Threshold Than in Table 21

Loop Length - [m]	# Feed-Forward Taps	# Feedback Taps
500	25	44
1000	32	56

The simulated BER performance on the 500 m and 1000 m loops using the smaller DFE's is shown below in Figure 47. The performance curves simulated using the longer equalizers specified in Table 21 are also shown for comparison. In all cases, the simulations employed a relatively long training sequence – approximately 65000 symbols – and a small adaptation step size, 0.00005.

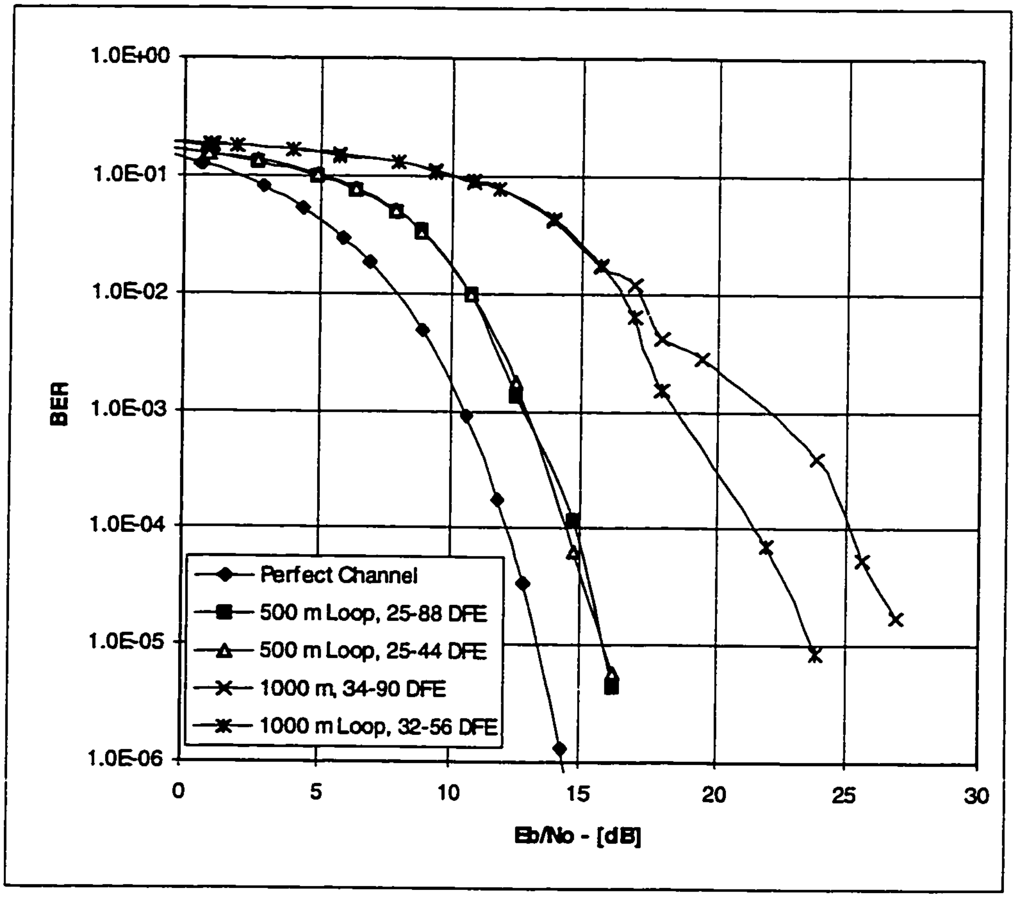

Figure 47: CAP-VDSL Performance with Emission Masking Using Smaller DFE's Than in Figure 46

As can be seen from the curves above, using a smaller DFE improves the simulated performance on the 1000 m loop. Approximately 3.5 dB improvement is observed at BER = 1e-5; a less than satisfactory penalty of approximately 8 dB is still present. The observed improvement with the smaller DFE on the 1000 m loop supports the idea that the poor performance on that loop is due to the high residual error associated with the large LMS adapted equalizer. Notice also that the performance on the 500 m loop is basically unchanged when the smaller DFE is used: this suggests that for the relatively high error probabilities considered, the original, larger equalizer was excessive. However, with the shorter equalizer, is possible that we might observe degradation at lower probabilities of error than the ones simulated due to the associated increase in residual ISI.

The results for the longer loops indicate that the feasibility of using a DFE adapted with standard LMS for 16-CAP VDSL transmission with emission masking is questionable. Since the number of equalizer taps is significantly higher than without emission masking, a very small step size is required to minimize the residual MSE due to error in the tap values. Even with the small step-size, the equalizer may exhibit poor convergence properties as evidenced by the simulated performance on the 1000 m loop. Using a very small step size has a major drawback: it slows down the time-domain response of the receiver. This increases the duration of the initial training period and makes the link more susceptible to any time variations in the channel response.

Alternative adaptive algorithms such as the recursive least-squares (RLS) and Kalman algorithms may be more appealing than LMS in this case, since they offer more rapid convergence [49].

6.4.1 Narrow-Band Interference and Multicarrier modulations.

Consider the scenario of purely sinusoidal signal interference acting on a multicarrier signal.

If we apply purely sinusoidal interference to a 256 sub-channel analysis CMFB (with overlap factor 4), we observe the interference profiles shown in Figure 48. The interference magnitudes observed on the sub-channels are normalized to the highest output level observed. The plot labeled "Case A" corresponds to the case where the sinusoidal interferer has exactly the same frequency as the center frequency of one of the CMFB-DMT sub-channels. The plot labeled "Case B" corresponds to the case where the sinusoid frequency falls exactly between the center frequencies of two adjacent sub-channels.

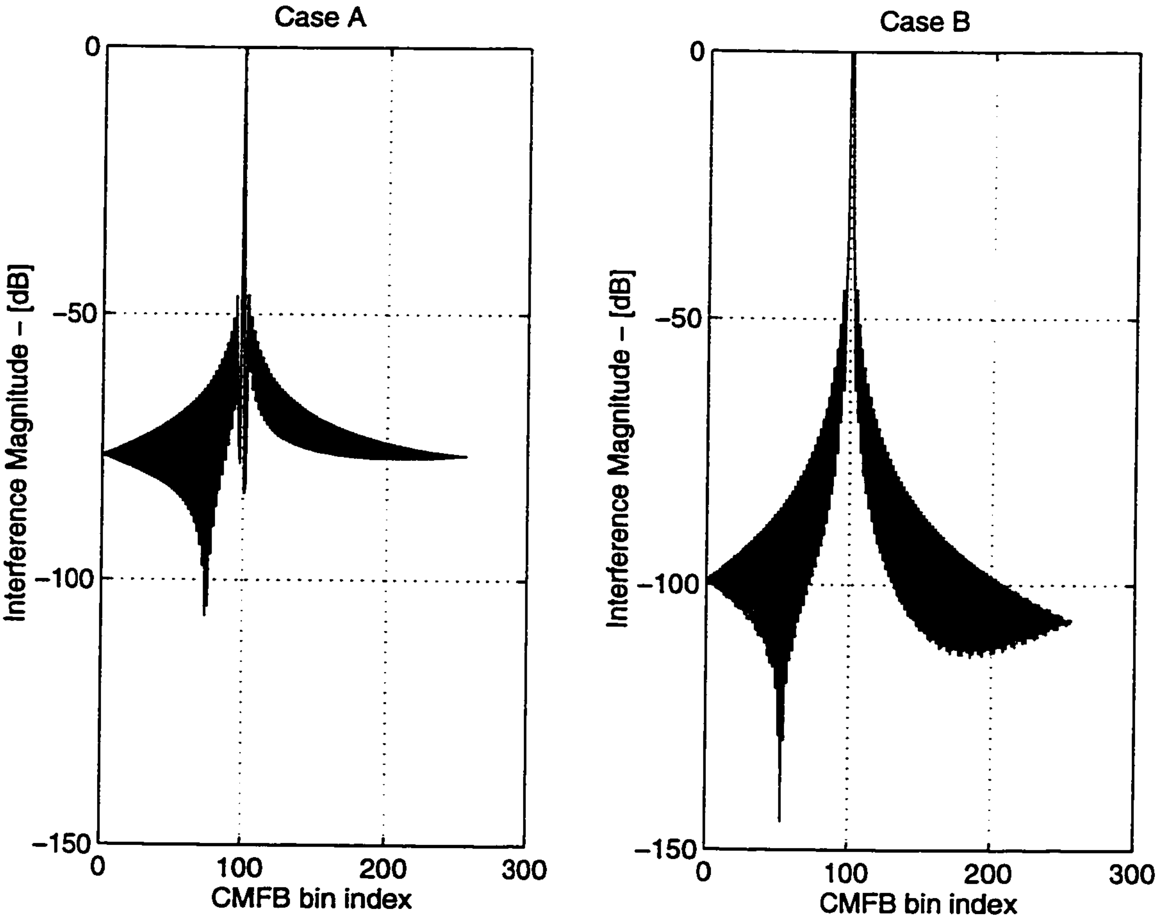

Figure 48: Normalized Narrow-Band Interference Magnitude at Output of Analysis CMFB (Case A – Interferer at sub-channel center; Case B – Interferer between two sub-channels)

The results in Figure 48 indicate that the alignment of the sinusoidal interference frequency with the CMFB-DMT center frequencies has only a marginal impact on the interference profile. For both Case A and Case B, the number of tones which have normalized interference levels greater than -50 dB is less than 15.

In the case of the FFT-DMT, the analysis transform output due to a sinusoidal interferer can vary drastically depending upon the relationship of the interferer tone to the center frequencies of the FFT sub-channels. Figure 49 below shows the interference magnitude output for a 256 sub-channel FFT-DMT system for the two extreme cases. In Case A, the interferer tone is located at the center frequency of one sub-channel and in Case B, the interfere is exactly between two sub-channels.

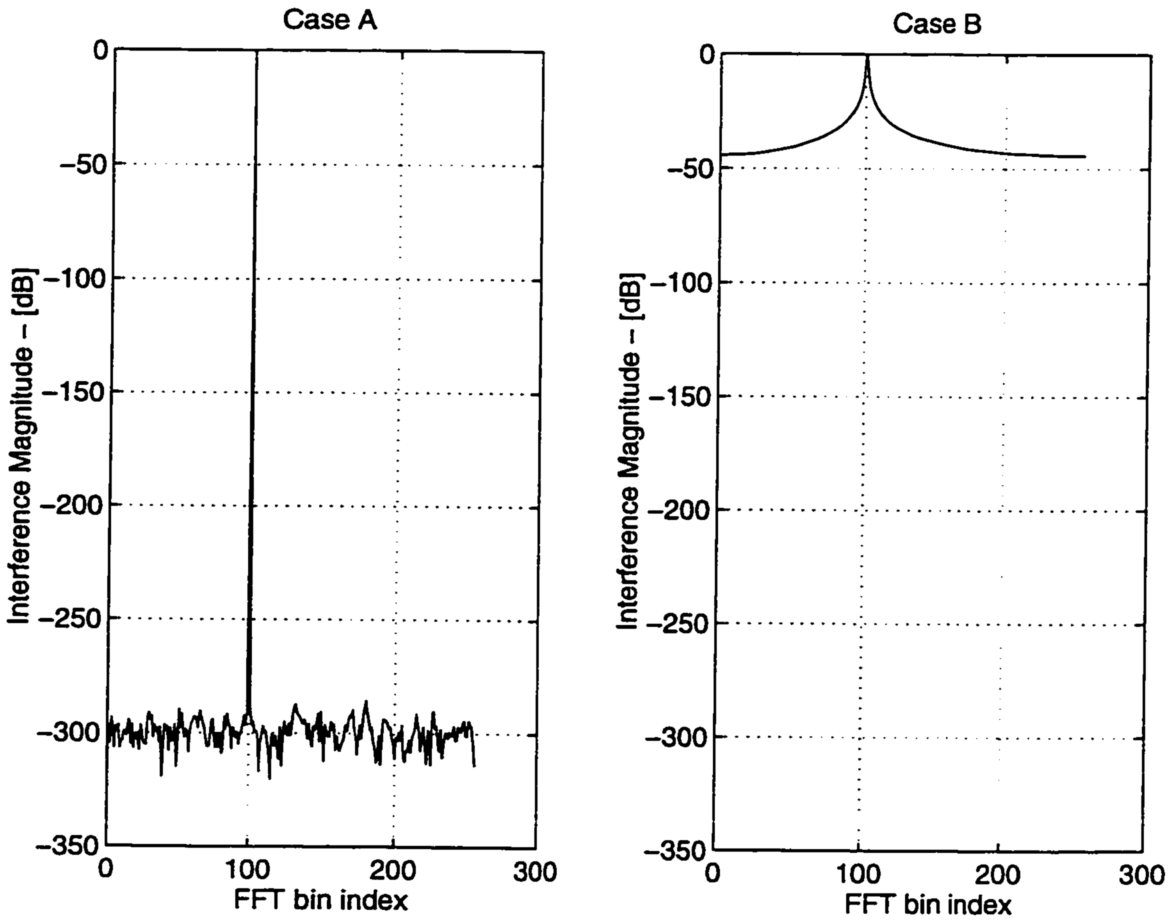

Figure 49: Normalized Narrow-Band Interference Magnitude at Output of Analysis FFT (Case A – Interferer at sub-channel center; Case B – Interferer between two sub-channels)

As can be seen from the plot labeled Case A in Figure 49, the analysis FFT is quite good at isolating interferer frequencies which correspond exactly to the center frequency of specific sub-channels (or FFT bins). However, if the interferer tone lies exactly between the center frequencies of two sub-channels as in Case B (the worst case scenario), many of the sub-channels are adversely affected. In fact, all of the sub-channels exhibit normalized interference levels above -50 dB. The performance of the FFT-DMT system is limited in this respect by the frequency response of the rectangular window used in applying the analysis transform.

In general, narrow band interference has a non-zero bandwidth. The worst case response to sinusoidal interference will likely define the general shape of the interference profile for each system. The spectrally isolated frequency responses of CMFB offer a significant advantage over the FFT responses. Compared to the FFT-DMT scenario, relatively few CMFB-DMT sub-channels are heavily impaired by narrow band interference. The capacity of a CMFB link impaired by narrow band interference will generally be better than a similarly impaired FFT-DMT link.

Chapter 7

Computational Complexity

The following pages include a brief analysis of the computational complexity of the three modulations considered in this work. In each case, a generalized estimate of the steady state computational complexity will be formulated based upon assumptions consistent with those applied in the rest of this work. Note that the complexity estimates for the multicarrier receivers will be somewhat optimistic due to the fact that the FIR pre-detection equalizers are assumed to be static in steady state. Finally, using parameters chosen based on the simulations, the complexity of the different modulations will be compared for the cases of transmission at both the ADSL and VDSL data rates.

7.1 CAP

We can estimate the computational complexity of the CAP transmitter based upon equation (6) which is included below for convenience.

$$x_n = \sum_k \left\{ a_k g_{I,(n-Nk)} + b_k g_{Q,(n-Nk)} \right\}$$

To form the contribution to the transmitted sequence of samples due to a single CAP symbol (i.e. for fixed k) it is necessary to scale the in-phase and quadrature-phase pulses and add them to appropriate samples of the transmitted sequence. The complexity per symbol is thus:

$$\begin{array}{ll} 2L_{pulse} & \text{multiplications / symbol} \\ 2L_{pulse} & \text{additions / symbol} \end{array} \qquad \ldots(84)$$

where L_{pulse} is the length in samples of the baseband pulse. Assuming 4 bits per symbol, as is the case for 16-CAP, the complexity per bit is

$$\begin{array}{ll} \frac{1}{2}L_{pulse} & \text{multiplications / bit} \\ \frac{1}{2}L_{pulse} & \text{additions / bit} \end{array} \qquad \ldots(85).$$

For the CAP receiver, assuming analog timing recovery, the major computational functions are the application of the detector filters and the equalizer. Based upon [24], the computational complexity of adaptation using the standard LMS algorithm in the case of the complex DFE is approximately 2 additions (or subtractions) to compute the complex error signal, 2 real multiplies to scale the error signal by the step size, and 2 real adds per tap for the update. Assuming that the detector filters are each of length L_{pulse} and that the equalizer has a total of N_{DFE} complex taps which are adapted once every symbol period, the complexity per symbol is:

$$\begin{array}{ll} 2L_{pulse} + 4N_{DFE} + 2 & \text{multiplications / symbol} \\ 2L_{pulse} + 4N_{DFE} + 2 & \text{additions / symbol} \end{array} \qquad \ldots(86).$$

Again assuming 4 bits per symbol, the complexity per bit is

$$\begin{array}{ll} \frac{1}{2}L_{pulse} + N_{DFE} + \frac{1}{2} & \text{multiplications / bit} \\ \frac{1}{2}L_{pulse} + N_{DFE} + \frac{1}{2} & \text{additions / bit} \end{array} \qquad \ldots(87).$$

The importance of the equalizer is clear from the equations above.

7.2 CMFB-DMT

The computational complexity of applying either the synthesis or analysis CMFB transform is (according to [42]):

$$\frac{3M}{2}\log_2(M) + gM \quad \text{multiplications}$$
$$\frac{M}{2}\log_2(M) + gM \quad \text{additions} \qquad \ldots(88)$$

where M is the number of sub-channels and g is the overlap factor.

The complexity per bit of the CMFB-DMT transmitter is thus

$$\frac{3M}{2b_A}\log_2(M) + \frac{gM}{b_A} \quad \text{multiplications / bit}$$
$$\frac{M}{2b_A}\log_2(M) + \frac{gM}{b_A} \quad \text{additions / bit} \qquad \ldots(89)$$

where b_A is the aggregate number of bits per symbol.

The CMFB-DMT receiver complexity is higher due to the presence of the linear equalizer and post-detection combiner. Assuming a linear equalizer with L_{FIR} taps and post detection combining with a depth of $|T|$ symbols and a width of $|\Omega|$ sub-channels (this implies $|T||\Omega|$ taps for *each* sub-channel), the receiver complexity is approximately:

$$\frac{3M}{2b_A}\log_2(M) + \frac{M}{b_A}\left(g + L_{FIR} + |T||\Omega| + 1\right) \quad \text{multiplications / bit}$$
$$\frac{M}{2b_A}\log_2(M) + \frac{M}{b_A}\left(g + L_{FIR} + 2|T||\Omega| + 1\right) \quad \text{additions / bit}$$

...(90).

Equation (90) assumes the post-detection combiner is updated each symbol period using the standard LMS algorithm as suggested in [54]. The LMS adaptation requires the computation of M error signals, multiplication of these by the step sizes, and addition of the various scaled error signals to the appropriate taps. The linear equalizer is assumed to be static in steady state.

7.3 FFT-DMT

The complexity of a 2M point FFT is (from[48]):

$$\begin{array}{ll} (8M+1)\log_2(M) & \text{multiplications} \\ (8M+1)\log_2(M) & \text{additions} \end{array} \qquad \ldots(91).$$

The $2M$ point transform corresponds to M-1 sub-channels capable of carrying 2-dimensional QAM symbols.

We can estimate the steady-state complexity of the FFT-DMT transmitter to be

$$\begin{array}{ll} \frac{(8M+1)}{b_A}\log_2(M) & \text{multiplications / bit} \\ \frac{(8M+1)}{b_A}\log_2(M) & \text{additions / bit} \end{array} \qquad \ldots(92).$$

The complexity of the FFT-DMT receiver includes the computation required for the TEQ and the frequency domain equalizer at the output of the analysis transform:

$$\begin{array}{ll} \frac{(8M+1)}{b_A}\log_2(M)+\frac{M}{b_A}\left(L_{TEQ}+6\right) & \text{multiplications / bit} \\ \frac{(8M+1)}{b_A}\log_2(M)+\frac{M}{b_A}\left(L_{TEQ}+6\right) & \text{additions / bit} \end{array}$$

$$\ldots(93).$$

The equation above assumes that the TEQ – which has L_{TEQ} taps – is static under steady state conditions. It also assumes that the frequency domain equalizer is adapted every symbol using the standard LMS algorithm. The adaptation complexity amounts to the computation of 1 complex difference for each sub-channel; multiplication of the complex error signals by the real valued step-sizes (2 multiplications); and addition of the scaled error signals to the appropriate taps.

7.4 Estimated Complexity for ADSL

The computational complexity relationships from the preceding pages were applied to estimate the complexity of the three modulations for the 6 Mbps ADSL rate on a 2000 m loop. The parameters employed in the calculations were as follows:

- In the case of CAP, the pulse duration is assumed to be a conservative 64 samples (in the simulations, the pulse was longer). An 11-10 DFE is also assumed.

- For CMFB-DMT we assume a 256 sub-channel filter bank with $g = 4$, an 8 tap linear equalizer, post-detection combining on each sub-channel using 25 adaptive taps, and a sampling rate of 2 MHz.

- The FFT-DMT system is assumed to use a 512 point FFT with 32 samples of cyclic prefix, a 12 tap TEQ, an adaptive complex FDEQ tap on each sub-channel and a 2 MHz sampling rate.

The results are shown in Table 23.

Table 23: Computational Complexity at the ADSL Rate on a 2000 m Loop

Modulation	TX Complexity	RX Complexity
16-CAP	32 Multiplies/bit 32 Additions/bit	53.5 Multiplies/bit 53.5Additions/bit
CMFB-DMT	5.3 Multiplies/bit 2.7 Additions/bit	16.7 Multiplies/bit 25.0 Additions/bit
FFT-DMT	10.0 Multiplies/bit 10.0 Additions/bit	12.9 Multiplies/bit 12.9 Additions/bit

As can be seen from the numerical data above, this analysis shows that the multicarrier modulations offer a computational complexity advantage over 16-CAP. This is despite the fact that it is necessary to compute two seemingly huge block transforms for each symbol. Since the multicarrier symbols carry large numbers of bits, the complexity per bit is small.

The complexities of the multicarrier transmitters are based solely upon the transform complexity. Note that the CMFB transform with $g = 4$ is actually less complex than the FFT (which had the same number of sub-channels) in terms of real operations since it is a real-valued transform.

The CMFB-DMT receiver requires 3.7 more multiplications per bit and 12 more additions per bit more than the FFT-DMT receiver. This is due to the fact that equalizing CMFB-DMT is more of a challenge.

Considering the end-to-end complexity of both the transmitter and receiver, the CMFB-DMT system requires 0.9 less multiplications per bit and 5 more additions per bit than the FFT-DMT system. Assuming that the number of instruction cycles required is the same for additions and multiplications, as in [58], the end-to-end CMFB-DMT system would offer a higher total processor load.

7.5 Estimated Complexity for VDSL

The exercise of estimating the computational complexity of the three modulations under consideration was repeated taking into account parameters used in the simulations at the VDSL rate on the 1000 m loop. The parameters which figured in the complexity estimates were as follows:

- For CAP, the pulse duration is assumed to be 64 taps. A 17-12 DFE is also assumed.
- In the case of CMFB-DMT, we assume a 512 sub-channel filter bank with $g = 4$, a 12 tap linear equalizer, post-detection combining with 25 adaptive taps for each sub-channel, and an 8.67 MHz sampling rate.
- The FFT-DMT system is assumed to use a 1024 point transform, a 64 sample cyclic prefix, a 16 tap TEQ, an adaptive frequency domain equalizer tap for each sub-channel and a sampling rate of 8.67 MHz.

The estimated computational complexity of the three systems is shown below in Table 24.

Table 24: Computational Complexity at the VDSL Rate on a 1000 m Loop

Modulation	TX Complexity	RX Complexity
16-CAP	32 Multiplies/bit 32 Additions/bit	61.5 Multiplies/bit 61.5Additions/bit
CMFB-DMT	5.8 Multiplies/bit 2.8 Additions/bit	19.2 Multiplies/bit 24.2 Additions/bit
FFT-DMT	11.3 Multiplies/bit 11.3 Additions/bit	14.7 Multiplies/bit 14.7 Additions/bit

The results above are very similar to those computed for the 2000 m ADSL loop in the previous section. The two multicarrier modulations both have significantly lower complexity than the CAP scheme. In each case, the receiver complexities have increased somewhat due to the increased equalization requirements.

Note that the multicarrier transmitter complexities are not appreciably different from the ADSL case – even though the transform size has doubled. This is because the bandwidth efficiency is the same for the two cases. The number of bits per multicarrier symbol is doubled by the increase in transform size (which equates to a longer symbol period) and this offsets the higher transform complexity.

Considering the end-to-end complexity of the two multicarrier modulations: CMFB-DMT requires 1 more multiplication per bit and one less addition per bit than FFT-DMT. Again invoking the assumption that the cost in execution cycles of adds and multiplies are equivalent, as in [58], the two multicarrier systems are equivalent.

Chapter 8

Conclusions and Suggestions for Future Work

8.1 Summary and Conclusions

What follows is a summary of the observations and results with references to the relevant figures and tables in this work.

1. **Link margins**

- Link margin versus loop length curves computed considering only AWGN were included in Figure 19 and Figure 21.

  ◊ Link margins (recorded in dB) under AWGN dominated conditions were observed to decrease linearly with increasing loop length.

  ◊ These figures indicated that on mildly attenuating, short loops, the link margins of 4-CAP, 16-CAP, 64-CAP and multicarrier modulation depend mostly upon SNR requirement. As a result, the margins on short loops decreased with increasing bandwidth efficiency.

  ◊ As the loop lengths increased and the CAP equalization penalties became significant, the situation was reversed and performance margins were observed to increase with increasing bandwidth efficiency on long loops. The margins for multicarrier modulation were superior to all three CAP modulations on long loops. This was attributed to the optimized bit allocation and spectrum shape of the multicarrier signal (which effectively gave it higher bandwidth efficiency). Another factor was the lack of a significant equalization penalty in the case of multicarrier modulation.

- The link margin versus loop length curves including the effects of both self-FEXT and AWGN were included inFigure 20 and Figure 22.

  ◊ When self-FEXT was dominant, link margins exhibited a relatively slow, monotonic decrease with increasing loop length.

  ◊ The self-FEXT dominated margins of 4-CAP, 16-CAP, 64-CAP and multicarrier modulation decreased with increasing bandwidth efficiency.

  ◊ The curves for 4-CAP, 16-CAP, and 64-CAP showed two distinct regimes. The margin performance was observed to be dominated by self-FEXT up to a certain loop length beyond which AWGN became the dominant impairment. The "critical lengths" at which this change occurred increased with increasing bandwidth efficiency (and decreasing signal bandwidth).

  ◊ The performance margins for multicarrier modulation in the presence of self-FEXT were generally comparable to those computed for CAP with similar bandwidth efficiency. The margins for multicarrier modulation became somewhat better than those for CAP on longer loops when AWGN became dominant. This character is attributed to the optimized nature of the multicarrier signal and the presence of significant equalization penalties in the CAP system.

- Link margins for 4-CAP, 16-CAP and 64-CAP with emission masking in the presence of AWGN were included inFigure 23.

  ◊ Penalties due to noise enhancement and power loss due to the masking notches increased with increasing bandwidth efficiency. A penalty of approximately 2 dB was observed in the case of 4-CAP; for 16-CAP the penalty was near 3 dB; and for 64-CAP a penalty of approximately 3.5 dB was observed.

- Estimates of the reach of 4-CAP, 16-CAP, 64-CAP and multicarrier modulation at the ADSL and VDSL data rates were included in Table 6 and Table 7. The reach figures were estimated assuming a minimum requirement of 6 dB performance margin with respect to the target error rate, BER = 1e-7.

    ◊ In the presence of AWGN, the reach increased with increasing bandwidth efficiency. This was attributed to the fact that signals with smaller bandwidth, experience proportionally less attenuation.

    ◊ At the ADSL rate and in the presence of self-FEXT, multicarrier modulation provided the best reach (> 2500 m) at the ADSL rate, followed by 64-CAP (~ 2400 m).

    ◊ At the VDSL rate with self-FEXT, both 16-CAP and multicarrier modulation provided approximately ~900 m reach. This was higher than that provided by 4-CAP and 64-CAP.

2. Performance in the Presence of AWGN

- The simulated BER performance of 16-CAP at the ADSL rate was shown in Figure 29.

    ◊ The performance penalties due to noise enhancement and error in the equalizer taps were observed to increase with loop length. Minimal penalties were observed down to BER = 1e-5 for 100 m and 500 m loops. A penalty of approximately 0.5 dB was observed for the 1000 m loop. The penalties observed at BER = 1e-5 on the 1500 m and 2000 m loops were approximately 1.5 dB and 2.5 dB respectively.

- Figure 30 included simulated BER performance curves for 16-CAP at the VDSL data rate.
  - ◊ The penalties observed for 16-CAP at the VDSL data rate increased more rapidly with increasing loop length than at the ADSL data rate. This was due to the larger bandwidth of the VDSL signal.
  - ◊ No significant penalty was observed on the short, 100 m loop. The penalty on the 500 m loop was approximately 1 dB. For the 1000 m loop, a somewhat heavy 4 dB penalty was observed at BER = 1e-5.
- Figure 31 showed the effect on BER performance of increasing the number of sub-channels in an FFT-DMT system. The simulations were all performed at the ADSL rate using a 1000 m loop and frequency domain equalization (complex AGC on each sub-channel).
  - ◊ BER performance improved as the number of sub-channels was increased. This was attributed to the fact that the channel response seen by each sub-channel became more ideal as the sub-channel bandwidth decreased and the symbol duration increased.
  - ◊ Even with a large number of sub-channels, significant degradation was observed on the 1000 m loop due to ISI and ICI. This identified a trade-off in the design of multicarrier communication links. On one hand, it is desirable to have a large number of sub-channels to keep the sub-channel bandwidth as small as possible. On the other hand, an excessively large transform is not desirable because it can make the transceiver hardware complex.
- Figure 32, Figure 33 and Figure 34 supported the argument that the most efficient equalization scheme for CMFB-DMT includes both an FIR equalizer at the receiver input and post-detection combining. The simulated ADSL rate

systems all used a 256 sub-channel CMFB with g= 4; the loop length considered was 2000 m.

◊ Figure 32 showed that the BER using only FIR equalization at the receiver input is quite poor. An error floor near BER = 5e-2 was observed even for relatively long equalizers (80 taps). This was attributed to the sensitivity of the CMFB orthogonality properties to even minimal distortion in the end-to-end channel and to numerical error in the filter bank.

◊ Figure 33 shows the performance using only idealized post-detection combining. The BER performance improved somewhat as the combiner dimensions were increased. Increasing the combiner dimensions beyond a certain point ($|\Omega| = 5$ - $|T| = 5$ for the case under consideration) was observed to provide diminishing returns in terms of the performance improvement. Severely degraded performance due to residual ISI and ICI was observed even for large 9-7 and 11-5 combiners.

◊ The BER performance curves in Figure 34 indicated that using a short FIR filter at the receiver input in conjunction with a moderately sized, idealized combiner could provide near ideal performance. For the 2000 m loop under consideration, using an 8-tap FIR equalizer along with a 5-5 post-detection combiner provided BER performance within 1 dB of ideal down to BER = 1e-9.

- The simulated BER performance of CMFB-DMT at the ADSL data rate was shown in Figure 35. All of the simulations used a 256 sub-channel CMFB with $g = 4$. Idealized 5-5 post-detection combiners were used in conjunction with optional FIR equalization.

◊ On the short 100 m and 500 m loops, it was determined the no FIR equalizers were required. For the 1000 m and 2000 m loops, 4 tap and 8 tap FIR equalizers were used, respectively.

◊ The performance on the 100 m, 500 m and 1000 m loops was practically ideal down to BER = 1e-13.

◊ In the case of the 2000 m loop, the performance was within 1 dB of ideal down to BER = 1e-9, as indicated above.

- BER performance curves at the VDSL data rate for CMFB-DMT were included in Figure 36 and Figure 37. These simulations employed a 512 sub-channel CMFB with $g = 4$. Again, 5-5 combiners were used with optional FIR equalization at the receiver input.

  ◊ No FIR equalizer was required for the 100 m loop. A 6 tap FIR equalizer was required for the 500 m loop. In the case of the 1000 m loop, it was determined that the performance did not improve for FIR equalizers longer than 12 taps

  ◊ The performance on the 100 m and 500 m loops was practically ideal.

  ◊ For the 1000 m loop, the performance was degraded due to residual ISI and ICI: an error floor was apparent near BER = 1e-7. The sensitivity to the small amount of residual signal-dependent interference was attributed to the use of large 128-level constellations on many sub-channels.

  ◊ The BER performance curves in Figure 37 indicate that by reducing the maximum allowable constellation size from 128 levels to 64 levels, the performance of CMFB-DMT VDSL on the 1000 m loop could be improved dramatically. A penalty of only 2 dB was observed at BER = 1e-8 using the smaller constellation size limit.

- Figure 38 included simulated BER performance curves for FFT-DMT transmission at the ADSL data rate. The simulations all used 256 sub-channels with a 32 point cyclic prefix as in the ADSL standard [4]. Both frequency domain equalization and time domain equalization were also employed.

  ◊ The TEQ lengths used for the 200 m 500 m 1000 m and 2000 m loops were 2 ,5 ,8 and 12 taps respectively.

  ◊ Practically ideal performance was observed for each case down to BER = 1e-12. This testified to the power of the FFT-DMT equalization scheme.

- BER performance curves for FFT-DMT at the VDSL rate were included in Figure 39 and Figure 40. The simulations which yielded these results used 512 sub-channels with a 64 point cyclic prefix and the same equalization scheme as for the ADSL simulations.

  ◊ The optimum TEQ dimensions were determined to be 2, 5 and 16 taps for the 100 m, 500 m and 1050 m loops respectively.

  ◊ The performance on the short 100 m and 500 m loops was nearly ideal. Due to some residual ISI and ICI, the performance on the 1000 m loop was degraded: a penalty of nearly 6 dB was evident at BER= 1e-9. As was the case for CMFB-DMT VDSL, this degradation was attributed to the use of large constellations on many low-frequency sub-channels.

  ◊ The BER performance curves in Figure 40 showed that nearly ideal performance was possible on the 1050 m loop when the maximum constellation size was reduced from 2^{14} points to 2^{12} points.

3. **Performance in the presence of self-FEXT**

- The link margin versus transmit power curves in Figure 41 through Figure 45 were used to analyze, in detail, the impact of self-FEXT on the performance of 16-CAP and multicarrier modulation at both the ADSL and VDSL rates.

  ◊ For both 16-CAP and multicarrier modulation, self-FEXT caused the link margins to saturate beyond some transmit power level.

  ◊ The link margins on loops saturated by self-FEXT were comparable for both types of modulation. This indicates that the self-FEXT phenomenon causes similar BER floors for both 16-CAP and multicarrier modulation.

  ◊ Two earlier observations were corroborated. These were the following: 1) link margin under self-FEXT dominated conditions decrease in a slow monotonic fashion with increasing loop length; 2) the absence of a noise enhancement penalty due to equalization gives multicarrier modulation a performance advantage over CAP on AWGN dominated loops.

4. **CAP with Emission Masking**

- Simulated BER curves for 16-CAP transmission at the VDSL rate with emission masking notches were shown in Figure 46 and Figure 47. The notches had a depth of 20 dB and corresponded to the amateur radio bands specified in Table 1.

  ◊ The curves indicated that a 2 dB performance penalty at BER = 1e-5 should be expected due to noise enhancement in the masking notches.

  ◊ On the 1000 m loop the performance was unsatisfactory due to poor equalizer convergence. This was attributed to the relatively large number of DFE taps required. This observation indicated that the LMS algorithm is not well suited for use with the large DFE's required in the emission masking scenario.

5. **Multicarrier modulations in the presence of narrow-band interference**

- The response of a representative CMFB and the FFT to sinusoidal interference was illustrated in Figure 49 and Figure 48. Two scenarios were considered in each case: 1) the interferer frequency was identical to the center frequency of one of the sub-channels; 2) the interferer frequency was exactly between the center frequencies of two adjacent sub-channels.

  ◊ For the CMFB (256 sub-channels with $g = 4$), the two scenarios provided similar interference profiles. The number of sub-channels which exhibited interference levels higher than 50 dB below the peak level was less than 15 in both cases.

  ◊ In the case of the FFT, the first scenario was the better of the two: only the sub-channel which corresponded to the interferer frequency was impaired to a significant degree. When the interferer tone was between two sub-channels, all of the sub-channels exhibited interference levels greater than 50 dB below the peak interference level.

  ◊ These observations suggested that CMFB-DMT should be more robust than FFT-DMT in the presence of narrow-band interference.

6. **Computational Complexity**

- Formulas which describe the computational complexity in real operations of CAP, CMFB-DMT and FFT-DMT were presented in Chapter 7. Estimates of the computational complexity of 16-CAP, CMFB-DMT and FFT-DMT at the ADSL and VDSL data rates were computed based upon parameters from the earlier simulations. These numerical results are included in Table 23 and Table 24.

◊ At both data rates, the complexity of the multicarrier systems was observed to be less than half that of the 16-CAP systems

◊ The CMFB-DMT transmitters at both data rates, had lower computational complexity by approximately a factor of 2 than the FFT-DMT transmitters. This was due to the fact that the CMFB transform is real valued.

◊ The CMFB-DMT receivers required about 25% more adds and nearly 100% more multiplies than the FFT-DMT receivers at both data rates.

◊ Taking into account the end-to-end computational complexity including both the transmitter and receiver, the differences between the two multicarrier modulations were more subtle. The CMFB-DMT system required marginally more operations at the ADSL rate while, at the VDSL rate the two had nearly identical complexity.

In summary, this work demonstrated that multicarrier modulations present interesting alternatives to the more traditional, single-carrier CAP scheme. They offer an advantage over CAP on long, AWGN impaired loops and in terms of computational complexity. Multicarrier modulations also exhibit performance similar to that of CAP under self-FEXT limited conditions. The multicarrier modulations also have the advantages of being less susceptible to impulse noise than CAP (due to their longer symbol time) and being more flexible than CAP in terms of band avoidance (in the narrow-band interference and emission masking scenarios). Among the multicarrier modulations neither CMFB-DMT or FFT-DMT was clearly superior to the other. The equalization scheme used in FFT-DMT was observed to be more efficient than that of CMFB-DMT. This is offset by the fact that CMFB-DMT should be more robust in the presence of narrow-band interference.

8.2 Suggestions for Future Work

The relatively broad scope of this thesis has necessitated sacrificing depth in places. Fortunately, the breadth of this work makes it possible to identify a number of topics which merit further study.

1. **Equalization:**

   - Equalization criteria and design constraints for the FFT-DMT TEQ. Current TEQ designs for DMT are ill-behaved optimization problems with several parameters. Furthermore, the literature on this topic is not very clear. Identifying new approaches and a tutorial treatment of the existing methods would be useful.

   - High performance adaptive algorithms for the CMFB-DMT FIR and post-detection combiner filters as well as for the large DFE's required for CAP transmission in the presence of emission masking.

   - Sensitivity of the multicarrier schemes to noisy equalizer/combiner coefficients.

2. **Multicarrier Modulations:**

   - Performance study of CMFB-DMT using near-perfect reconstruction (NPR) filter banks. Near-perfect reconstruction (NPR) cosine modulated filter banks offer potential for better spectral isolation than for the PR filter banks used in this work. Post-detection combining could eliminate the effects of reconstruction error.

   - Performance studies which include NEXT and impulse noise; more in-depth work on narrow band interference.

   - Error control coding strategies for multicarrier modulations.

- Factors which affect the performance of full-duplex xDSL transmission using the different duplexing techniques.

3. **CAP Modulation:**

   - Optimum transmit and receive pulse shapes in the presence of spectrally shaped noise.

4. **Transceiver Implementation:**

   - Impact of subtle issues such as oscillator drift and timing phase error on multicarrier modulation performance.

   - Effects of finite precision computations on multicarrier modulation performance.

   - Hardware complexity and cost of CAP, FFT-DMT and CMFB-DMT modems. In this work, the multicarrier modulations were shown to offer a computational complexity advantage. These results do not give an accurate indication of the hardware cost. Implementing a transform-based modulation most likely requires many "slow" hardware elements. Implementing CAP modulation requires relatively few hardware elements but they must operate at high speed.

   - Efficient line driver designs capable of handling the large dynamic range of multicarrier signals.

5. **Impulse Noise:**

   - Modeling impulse noise for the VDSL bandwidth.

   - Optimizing multicarrier signals to make them less susceptible to impulse noise.

As the list above suggests, the broadband access technology arena offers many interesting research topics. One of the most appealing aspects of this area is the broad range of subject matter which comes into play – from mathematics-oriented topics such as multirate filter banks to electronic design.

BIBLIOGRAPHY

[1] ADSL Forum. WWW site materials. Available from: http://www.adsl.com/. February 1997.

[2] N. Al-Dahir, J. Cioffi. "A Low-Complexity Pole-Zero MMSE Equalizer for ML Receivers." Proceedings of the Allerton Conference on Communications Computing and Control. September 1994.

[3] N. Al-Dahir, J. Cioffi. "Optimum Finite Length Equalization for Multicarrier Transceivers." IEEE Trans. on Communications. Vol. 44. No. 1. January 1996.

[4] Alliance for Telecommunications Industry Solutions. "American National Standard for Telecommunications – Network and Customer Installation Interfaces – Asymmetric Digital Subscriber Line (ADSL) Metallic Interface. ANSI T1.413 1995" ANSI. New York. 1995.

[5] M. Barton. "Optimization of Discrete Multitone to Maintain Spectrum Compatibility With Other Transmission Systems on Twisted Copper Pairs." IEEE JSAC. Vol. 13. No. 9. December 1995.

[6] M. Barton et al. "Performance Study of High-Speed Asymmetric Digital Subscriber Lines Technology." IEEE Trans. on Communications. Vol. 44. No. 2. February 1996.

[7] M. Barton. "Impulse Noise Performance of an Asymmetric Digital Subscriber Lines Passband Transmission System." IEEE Trans. Comm. Vol. 43. No. 2/3/4. February/March/April 1995.

[8] M. Barton. "On the Performance of an Asymmetrical Digital Subscriber Lines QAM Transceiver." IEEE Globecom '91.

[9] J.A.C. Bingham. "Multicarrier Modulation for Data Transmission: An Idea Whose Time Has Come." IEEE Communication Magazine. May 1990.

[10] C. Bourget. Personal communication. May 1997.

[11] W.Y. Chen et al. "Design of Digital Carrierless AM/PM Transceivers." T1E1.4 92-149.

[12] D.K.Cheng. <u>Field and Wave Electromagnetics</u>. Addison-Wesley. Don Mills, Ontario. 1990.

[13] J.S. Chow et al. "Equalizer Training Algorithms for Multicarrier Modulation Systems." IEEE ICC. Geneva, Switzerland. 1993.

[14] J.S. Chow, John Cioffi. "A Cost-Effective Maximum Likelihood receiver for Multicarrier Systems." IEEE ICC. Chicago. 1992.

[15] P.S. Chow et al. "A Practical Discrete Multitone Transceiver Loading Algorithm for Data Transmission Over Spectrally Shaped Channels." IEEE Trans. on Communications. Vol. 43. No. 2/3/4. February/March/April 1995.

[16] J. Cioffi. "Very-high-speed Digital Subscriber Lines – System Requirements (95-117R4)". ANSI. March 1996.

[17] B. Daneshrad, H. Samueli. "A 1.6 Mbps Digital-QAM System for DSL Transmission." IEEE JSAC. Vol. 13. No. 9. December 1995.

[18] B. Daneshrad, H. Samueli. "A Carrier and Timing Recovery Technique for QAM Transmission on Digital Subscriber Loops." IEEE ICC. Geneva, Switzerland. 1993.

[19] M.S. El-Tanany et al. "DSP Techniques in High Speed Transceivers (Course Notes)." Short course offered at Nortel. Winter 1997.

[20] N. Erdol et al. "Wavelet Modulation: A Prototype for Digital Communication Systems." Florida Atlantic University. 1994.

[21] M. Ghosh, "Analysis of the effect of impulse noise on multicarrier and single carrier QAM systems." IEEE Transactions on Comm. Vol. 43. No. 2. 1995.

[22] R.D. Gitlin, J.F. Hayes. Data Communications Principles. Plenum Press. New York. 1992.

[23] M. Hawryluck and M. Kavehrad. "Equalization Requirements for CAP/QAM Transmission at ADSL and VDSL Data Rates on Category-3 Unshielded Twisted Pair: Theory and Simulation Results." Canadian Conference on Broadband Research. Ottawa. April 1997.

[24] S. Haykin. Adaptive Filter Theory. 3rd Ed. Prentice-Hall. Englewood Cliffs, N.J. 1996.

[25] W. Henkel et al. "A Wide-Band Impulse-Noise Survey on Subscriber Lines and Inter-Office Trunks — Modeling and Simulation." IEEE Globecom. 1995.

[26] W. Henkel et al. "Coded 64-CAP ADSL in an Impulse-Noise Environment — Modeling of Impulse Noise and First Simulation Results." IEEE JSAC. Vol. 13. No. 9. Dec. 1995.

[27] W. Henkel, T. Keßler. "A Wideband Impulsive Noise Survey in the German Telephone Network : Statistical Description and Modeling." AËU. Vol. 48. No. 6. May 1994.

[28] G-H. Im et al. "51.84 Mbps 16-CAP ATM LAN Standard." IEEE JSAC. Vol. 13. No. 4. May 1995.

[29] I. Kalet. "The Multitone Channel." IEEE Trans. on Communications. Vol. 37. No. 4. February 1989.

[30] M. Kavehrad. "Performance of Nondiversity Receiver for Spread Spectrum in Indoor Wireless Communications." AT&T Technical Journal. Vol. 64. No. 6. July-August 1985.

[31] M. Kavehrad, M. Joseph. "Maximum Entropy and the Method of Moments in Performance Evaluation of Digital Communication Systems." IEEE Trans. on Communications. Vol. COM-34. No. 12. December 1986.

[32] M. Kavehrad, P.J. McLane. "Performance of Low-Complexity Channel Coding and Diversity for Spread Spectrum in Indoor, Wireless Communication." AT&T Technical Journal. Vol. 64. No. 8. October 1985.

[33] A. Kim. "Two Way Cable Television System Characterization." Cable Television Laboratories, Inc. Louisville. 1995.

[34] A. Kim. "Digital Transmission Characterization of Cable Television Systems." Cable Television Laboratories, Inc. Louisville. 1994.

[35] R.D. Koilpillai, P.P. Vaidyanathan. "Cosine modulated Perfect Reconstruction FIR Filter Banks Satisfying Perfect Reconstruction." IEEE Trans. on Signal Processing. Vol. 40. No. 4. April 1992.

[36] S. A. Kosmopoulos et al. "Fourier-Bessel Error Performance Analysis and Evaluation of M-ary QAM Schemes in an Impulsive Noise Environment." IEEE Trans. Comm. Vol. 39. No. 3. March 1991.

[37] H. Kwon, S. Chun. "Performance of DMT and CAP/QAM VDSL on ANSI Test Loops. (T1E1.4/96-107)" ANSI. April 1996.

[38] I. Lee et al. "Performance Evaluation of a Fast Computation Algorithm for the DMT in High-Speed Subscriber Loop." IEEE JSAC. Vol. 13. No. 9. December 1995.

[39] A.R. Lindsey, J.C. Dill. "Wavelet Packet Modulation: A Generalized Method for Orthogonally Multiplexed Communications." IEEE Southeastern Symposium on System Theory. March 1995.

[40] A.R. Lindsey. "Multi-Dimensional Signaling Via Wavelet Packets." Proceedings of the International Society for Optical Engineering Annual Meeting. April 1995.

[41] H.S. Malvar. "Extended Lapped Transforms: Properties, Applications and Fast Algorithms." IEEE Trans. on Signal Processing. Vol. 40. No. 11. November 1992.

[42] J. Mau. "Perfect Reconstruction Modulated Filter Banks: fast algorithms and attractive new properties." IEEE. 1993.

[43] K. Maxwell. "Asymmetric Digital Subscriber Line: Interim Technology for The Next Forty Years." IEEE Comm. Magazine. October 1996.

[44] R. Mélinand. "Internship Report: Impulse Noise Modeling and Simulation in the Loop Plant." BCRL Internal Report. University of Ottawa. Dec. 1996.

[45] P.J.W. Mesla et al. "Impulse Response Shortening for Discrete Multitone Transceivers." IEEE Trans. Communications. Vol. 44. No. 12. December 1996.

[46] D.G. Messerschmitt. "A Transmission Line Modeling Program Written in C." IEEE JSAC. Vol. SAC-2. No. 1. January 1984.

[47] T.Q. Nguyen. "Digital Filter Bank Design: Quadratic Constrained Formulation." IEEE Trans. on Signal Processing. Vol. 43. No. 9. September 1995.

[48] A.V. Oppenheim, R.W. Schafer. Discrete-Time Signal Processing. Prentice-Hall. Englewood Cliffs, N.J. 1989.

[49] J. Proakis. Digital Communications 3rd ed. McGraw. New York. 1995.

[50] R.S. Prodan et al. "Analysis of Cable System Digital Transmission Characteristics." Cable Television Laboratories, Inc.

[51] S.U.H. Qureshi. "Adaptive Equalization." Proceedings of the IEEE. Vol. 73. No. 9. September 1985.

[52] A.D. Rizos et al. "Comparison of DFT and Cosine Modulated Filter Banks in Multicarrier Modulation." IEEE Globecom '94.

[53] M. Rossi et al. "Iterative Least Squares Design of Perfect Reconstruction QMF Banks." CCECE '96.

[54] S. Sandberg, M.A. Tzannes. "Overlapped Discrete Multitone Modulation for High Speed Copper Wire Communications." IEEE JSAC. Vol. 13. No. 9. December 1995.

[55] A. Sendonaris et al. "Joint Signaling Strategies for Maximizing the Capacity of Twisted Pair Loops." Rice University.

[56] G. Strang, T.Q. Nguyen. Wavelets and Filter Banks. Wellesley-Cambrige. Wellesley, Mass. 1996.

[57] L Swingle. "Impulse Noise Measurements in New York City and Their Possible Ramifications on Selection of DSL Line Code Standard (T1D1.3/86-144)." ANSI. Aug. 1986.

[58] <u>Third-Generation TMS320 User's Guide, SPRU031</u>. Texas Instruments Incorporated. Dallas, Texas. 1988.

[59] M. Tzannes et al. "The DWMT: A Multicarrier Transceiver for ADSL Using M-band Wavelet Transforms." ANSI T1E1.4 93-067. March 1993.

[60] M.Tzannes. "System Design Issues for the DWMT Transceiver." ANSI T1E1.4 93-100. April 1993.

[61] United States Federal Communications Commission. Web-site materials available from: http://www.fcc.gov/. March 1997.

[62] A. Vahlin, N. Holte. "Optimal Finite-Duration Pulses for OFDM." IEEE. 1994.

[63] P.P. Vaidyanathan. Multirate Systems and Filter Banks. Prentice-Hall. Englewood Cliffs, N.J. 1992.

[64] P.P. Vaidyanathan. "Multirate Digital Filters, Filter Banks, Polyphase Networks and Applications: A Tutorial." Proc. of the IEEE. Vol. 78. No. 1. January 1990.

[65] H. Van De Velde et al. "Effect of Cable and System Parameters on Passband ADSL Performance." IEEE Trans. Communications. Vol. 43. No. 2/3/4. February/March/April 1995.

[66] J.J. Werner. "The HDSL Environment." IEEE JSAC. Vol. 9. No. 6. August 1991.

[67] J.J. Werner. "Impulse Noise in the Loop Plant." IEEE Globecom. 1990.

[68] Westell Technologies, Inc. "DSL Technology for Internet Access Vital to the Future of Telephone Companies." Available from: http:///www.westell.com:80/westell/adslWpr.html. February 1997.

[69] N.A. Zervos, I. Kalet. "Optimized Decision Feedback Equalization Versus Optimized Orthogonal Frequency Division Multiplexing for High Speed Data Transmission Over the Local Cable Network." ICC. 1989.

TEST TARGET (QA-3)

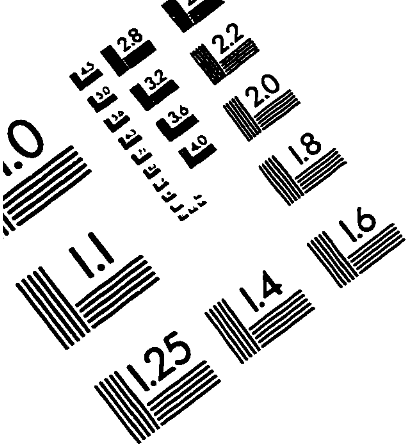

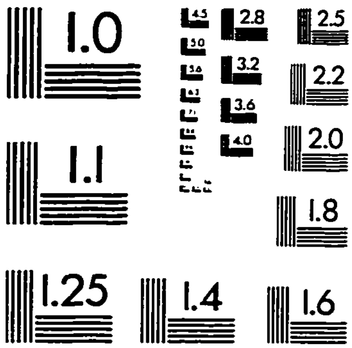

150mm

6″

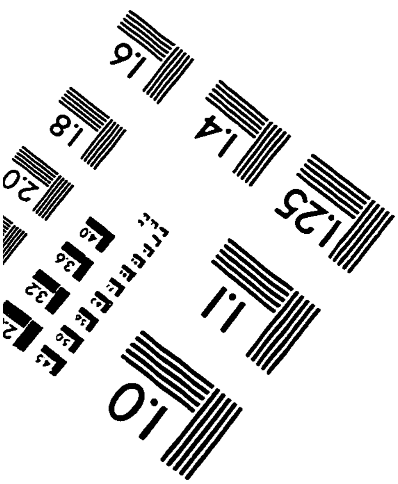

APPLIED IMAGE, Inc
1653 East Main Street
Rochester, NY 14609 USA
Phone: 716/482-0300
Fax: 716/288-5989